NTNU

Norwegian University of
Science and Technology

Fluid structure interaction aspects in obstructive sleep apnea patients

Øyvind Hole

Master of Science in Mechanical Engineering
Submission date: June 2017
Supervisor: Bjørn Helge Skallerud, KT

Norwegian University of Science and Technology
Department of Structural Engineering

ABSTRACT

In this master thesis, a comparative study of the feasibility of fluid-structure interaction (FSI) tools has been done in light of simulating the problem of obstructive-sleep apnea (OSA). Part of the study has been done by simulating the benchmark; *Flow Induced Oscillations of a Flexible Beam*, by the different solvers; COMSOL, Abaqus and Abaqus coupled with ANSYS Fluent through third party coupling code MpCCI. By evaluating the results produced a qualifying approach for simulating the case of OSA is done.

By assessing through FSI simulations, insight to the problem at hand can be gained. Making a proper problem formulation can be crucial to get a physical meaningful analysis. When setting up FSI simulations, several choices have to be made to make the most suitable approach. For instance if the type of discretization should be described with a Lagrangian, Eulerian or an Arbitrary Lagrangian-Eulerian (ALE) formulation, and how the coupling of the fluid and solid domain should be done.

The capturing of the interface and the interaction between the fluid and structure proves to be essential for the simulations. In addition to the choice of dicretization and coupling of the domains, the simulations is sometimes limited by technical problems and the feasibility of tools.

The use of computational FSI analysis can be a cumbersome task even if simulations yield decent results. The majority of the benchmark simulations did not produce the results expected. Only two of four simulations reached oscillations resembling the pattern shown in other studies. Thus indicating errors in model description and/or weaknesses of tools. For instance the capability to solve for non-linear behaviour.

The main issue for the benchmark simulations were related to the deformation and mesh motion of the fluid domain by the use of the ALE method, which often required a finer mesh tuning increasing the computational cost. The results from the benchmark were post processed in COMSOL and Abaqus, and compared in order to see to what extent they correlated. For additional perspective a comparable study is referred to in context of some of the findings [5].

By formulating a simpler problem description for the case of OSA some of the issues related to large deformations were bypassed. The simulation of the soft palate yielded coarse yet useful results, which can be used to get some insights to the disease. However, due to some of the flow specifics other problems were encountered, mainly regarding the embedded 3D simulations done with Abaqus. These primarily concerned convergence criteria for the equilibrium

equations, where a low Reynolds number and high flow velocity demanded fine tuning of mesh and additional equilibrium convergence iterations.

SAMMENDRAG

I denne masteroppgaven har en komparativ studie av brukbarheten til fluid-struktur interaksjon (FSI) verktøy blitt gjort i lys av å simulere problemet med obstruktiv søvnapné (OSA). En del av studien er gjort ved å simulere en standard test; *Flow Induced Oscillations of a Flexible Beam*, av de forskjellige simuleringsverktøyene; COMSOL, Abaqus og Abaqus kombinert med ANSYS Fluent via en tredjeparts koblingskode, MpCCI. Ved å evaluere de oppnådde resultatene er det gjort en kvalifiserende tilnærming for simulering av sykdommen OSA.

Ved å vurdere problemstillingen gjennom FSI-simuleringer kan man få innsikt i detaljene rundt fenomenet. Å lage en god problemformulering kan være avgjørende for å få en fysisk meningsfull analyse. Når FSI-simuleringer settes opp, må det gjøres flere valg for å gjøre den mest hensiktsmessige tilnærmingen. For eksempel om diskretisering av domenene bør beskrives med en Lagrangian, Eulerian eller en vilkårlig Lagrangian-Eulerian (ALE) formulering, og hvordan koblingen av domenene skal utføres.

Samspillet mellom væsken og strukturen viser seg å være avgjørende for simuleringene. I tillegg til valget av diskretisering og kopling av domenene, kan simuleringene noen ganger begrenses av tekniske problemer og mangler ved verktøyene.

Bruken av beregningsbasert FSI-analyse kan være en besværlig oppgave, selv om simuleringer er gjennomførbare og anstendige resultater oppnåes. De fleste av referansesimuleringene produserte ikke de forventede resultatene. Kun to av fire simuleringer nådde svingningene og mønsteret vist i andre studier. Dette indikerer at feil har blitt gjort i modellbeskrivelsen og/eller svakheter i verktøy. For eksempel evnen verktøyene har til å løse for ikke-lineæritet.

Hovedproblemet i tilfellet av den standard utformede simuleringstesten var relatert til deformasjon og mesh-bevegelse av væskedomenet ved bruk av ALE-metoden, som ofte krevde en finere maskingesting som ofte krever ett finere mesh og som øker kjøretiden. Resultatene ble etterbehandlet i COMSOL og Abaqus, og sammenlignet for å se i hvilken grad de korrelerte. For ytterligere perspektiv er en sammenlignbar studie referert til i sammenheng med noen av funnene [5].

Ved å formulere en enklere problembeskrivelse for tilfelle av OSA ble noen av problemene knyttet til store deformasjoner omgått. Simuleringen av den myke ganen ga grove, men likevel nyttige resultater for å få innsikt i sykdommen. På grunn av noen av strømningsspesifikasjonene oppstod imidlertid andre problemer. Spesielt i de innebygde 3D-simuleringene gjort med Abaqus.

Disse vedrørte hovedsakelig konvergenskriterier for likevektsligningene, hvor det relativt lave Reynolds tallet og høy luftstrømningshastighet krevde finjustering av mesh og ytterligere iterasjoner.

Don't judge each day by the harvest you reap
but by the seeds that you plant.

— Robert Louis Stevenson

ACKNOWLEDGMENTS

I would like to express gratitude towards my supervisor Bjørn Helge Skallerud for making it possible to define an interesting and fitting task and helping throughout the whole project. Furthermore i would like to thank Paul Roger Leinan for sharing precious time and knowledge by supporting with experience and ideas on the usage of software.

Finally i would like to thank my family and the student community at NTNU, where optimism is always found in times of hardship.

CONTENTS

LIST OF FIGURES

LIST OF TABLES

ACRONYMS

OSA	Obstructive Sleep Apnea
FSI	Fluid Structure Interaction
MAD	Mandibular Advancement Device
CPAP	Continuous Positive Airway Pressure
CFD	Computational Fluid Dynamics
PDE	Partitioned Differential Equation
FDM	Finite Difference Method
FEM	Finite Element Method
FVM	Fluid Volume Method
VOF	Volume Of Fluid
ALE	Arbitrart Lagrangian Eulerian

PREFACE

THE PROJECT

This is the master thesis for the degree of master of science in mechanical engineering, faculty of engineering of NTNU.

Currently NTNU runs a research project funded by Research Council of Norway that address improved understanding of obstructive sleep apnea (OSA). The project is a collaboration between Medical Faculty (PhD-position) and Faculty of Engineering Science (2 PhD-positions). The project addresses a combination of both fluid and solid mechanical issues related to the upper airway. A part objective is to combine the fluid and solid models in FSI simulation to evaluate to what extent there is an interaction between the two domains. A comparative study of FSI simulation coupling is advisable to qualify an approach to this.

This project is carried out with support from SINTEF. Headquartered in Trondheim, SINTEF is the largest independent research orginaisation in Scandinavia. A feasibility and comparative study of FSI simulations coupling codes by internal and external co-simulation and from different solvers is beneficial. The study will involve finite volume (FVM) and finite element analysis (FEA) code using Arbitrary Lagrangian Eulerian (ALE). The concerning FEA code Abaqus is provided by Simulia, and Comsol by Comsol, Inc. The CFD solver Fluent is provided by Ansys, Inc. and the coupling code MpCCI is developed by Fraunhofer SCAI.

OUTLINE

The purpose of this master thesis is to make a study of the feasibility of Abaqus coupled with Fluent in comparison to in-house coupling by Abaqus and Comsol. This is done in the light of simulating the problem of obstructive-sleep apena (OSA). Prerequisites for this study are knowledge about the mechanics of solids and fluids. The scopes of disciplines each has its own research field. The mechanics related to OSA is muscle tissue and airflow. To start, an introduction describing the problem and basic anatomy/physiology/pathophysiology related to OSA is given in part one.

A combination of both solid and fluid belongs to the fluid-structure interaction field, a research field gaining popularity the last decade. The mathematics to solve these problems, whereof the majority exists of numerical methods, are also of importance. These prerequisites are treated in part two, the theory part of the thesis. This part is divided into chapters explaining the basis of mul-

tiphysics, discretisation, fluid and solid mechanics, numerical approach and computational methods, and computational FSI.

When the introduction to the problem of OSA and the prerequisites of FSI and numerical methods are understood, one can continue to part three, which formulates and treats a academic test problem; *Flow Induced Oscillations of a Flexible Beam*, for the sake of benchmarking correlations and channel flow with a flexible beam and an obstruction to resemble the case of OSA.

Part I

INTRODUCTION

By evaluating obstructive sleep apnea syndrome through computational fluid-structure interaction simulations knowledge can be gained about the physical behaviour of the disease. Formulating so called benchmark problems by FSI and testing different solvers can be the key to gaining advantage. To be able to tackle this, defining some of the groundwork for both the medical and the engineering side of the problem has to be done. The report will thus address a combination of both fluid and solid mechanical issues related to fluid-structure interaction and the upper airway.

Some physiological background related to OSA is necessary to understand the concept and purpose of the study. Part I will give some insights into the fundamental anatomy of the upper airway and the disease. Then a brief introduction of the interests and applications for computational FSI for this problem will be given.

1 OBSTRUCTIVE SLEEP APNEA

1.1 THE DISEASE

For the case of OSA, only the upper respiratory system is of interest. The upper airway consists of the nose and nasal cavity, the mouth and oral cavity, and the throat which is composed of the pharynx and larynx [Figure 1].

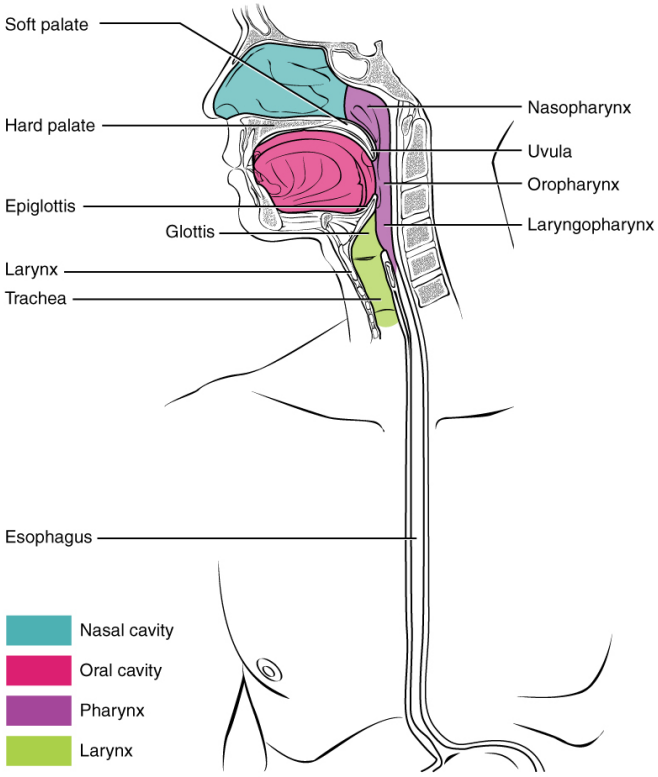

Figure 1: Upper airway anatomy [12].

1.1.1 *Background knowledge*

"The pathogenesis of obstructive sleep apnea (OSA) has been under investigation for over 25 years, during which a number of factors that contribute to upper airway (UA) collapse during sleep have been identified." - Cloudagh & T.Douglas, 2005 [11]

Obstrucive Sleep apnea is a potentially serious sleep disorder [30], which approximately affects 2 - 4% of the population. It causes breathing to repeatedly stop and start during sleep. This type of apnea is caused by the airway being

sucked close on inspiration during sleep. The phenomena is perhaps best described by Blumen et al. [9]

"Pathophysiology of the obstructive sleep apnea syndrome shows three components: intra and peripharyngeal obstacles, excessive pharyngeal wall compliance and upper airway dilator muscle dysfunction. The upper airway dilator muscle contraction occurs at the beginning of inspiration, thus maintaining opened the pharyngeal lumen through inspiration."

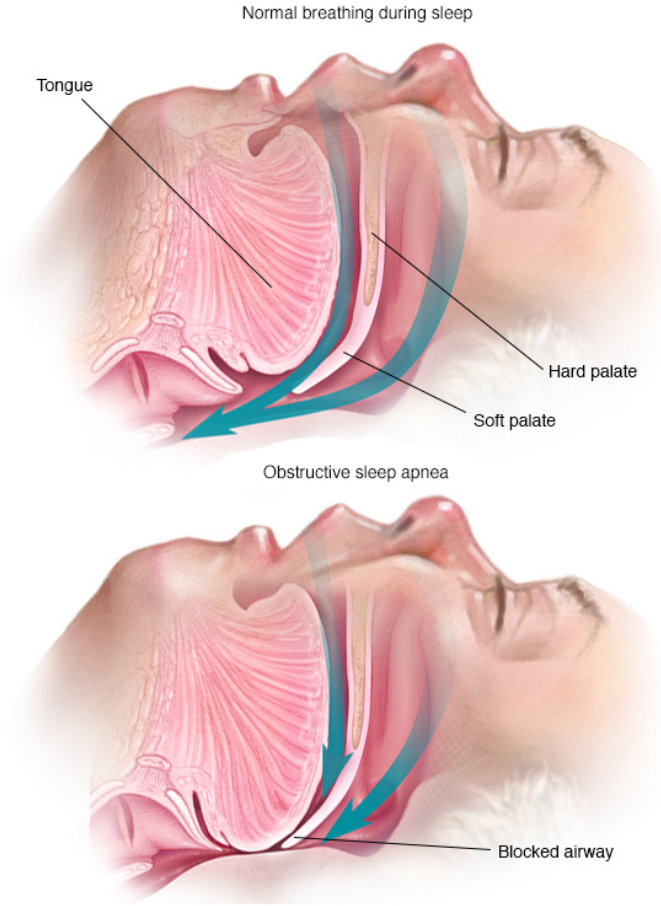

Figure 2: Obstrucive sleep apnea syndrome [31].

The airway is kept patent by the dilating muscles which have higher than normal activity during wakefulness. But during sleep the muscle tone falls and the airway narrows [9]. The upper airway dilating muscles, which are composed of striated muscle tissue, normally relaxes during sleep. In patients with OSA, the dilating muscles can no longer successfully oppose negative pressure within the airway during inspiration. Snoring may then occur; followed by airway occlusion and subsequent apnea.

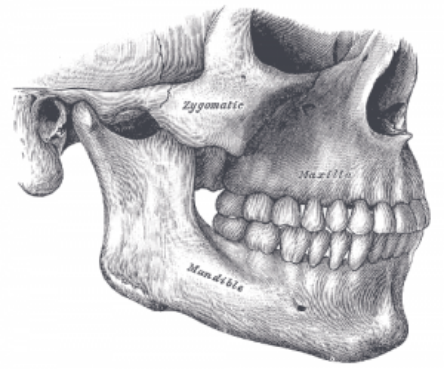

Figure 3: The maxilla and mandible [18].

Any narrowing in the pharynx will comply for the predisposal of OSA. Factors which cause narrowing of pharynx may be, e.g obisity, large tonsils or shortening of the mandible or maxilla [Figure 3]. Abnormal hormone levels conditions such as hypothyroidism or acromegaly may also narrow the upper airway with tissue infiltration.

1.1.2 *Sites of airway collapse*

In most subjects suffering from OSA, airway closure usually occurs within the oral pharyngeal region [13]. This region is also typically smaller in OSA patients. Airway narrowing is a dynamic process and may vary among subjects, including both the retroglossal and hypopharyngeal areas. However the retropalatal region of the oropharynx is the most common site of collapse.

1.1.3 *Treatments*

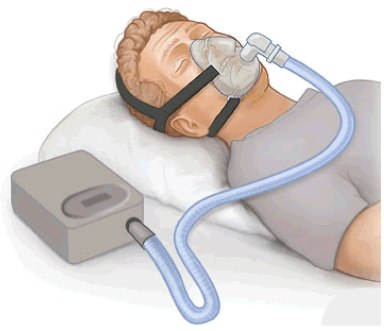

(a) Continuous Positive Airway Pressure (CPAP) [29].

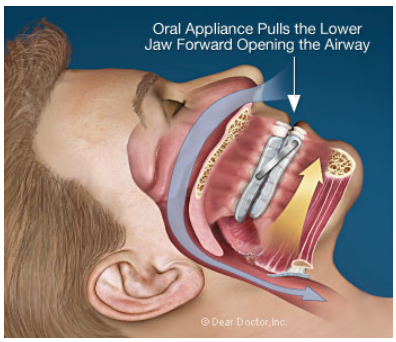

(b) Mandibular Advancement Device (MAD) [24].

Figure 4: Two recommended methods of treatment.

Treatments for obstructive sleep apnea are available. One treatment involves using a pumping device (CPAP/APAP) that keep the airway open by providing air pressure while breathing [Figure 4]. The compressed air is then delivered through a mask covering the patient's nose and/or mouth. Another option is using a oral prosthesis (MAD) to thrust your mandible forward during sleep, thus moving the tongue out of the oropharynx.

In more severe cases, surgery may be an option. *Hyo-mandible Suspension* is an example of a surgery with aim to treat OSA. By repositioning and securing the hyoid [Figure 5] from above the thyroid cartilage to just over it, the tounge base and epiglottis advances forward [10]. Thereby opening the retrolingual and hypopharyngeal airway passage in the pharynx. This treatment has been shown to be highly effective [1].

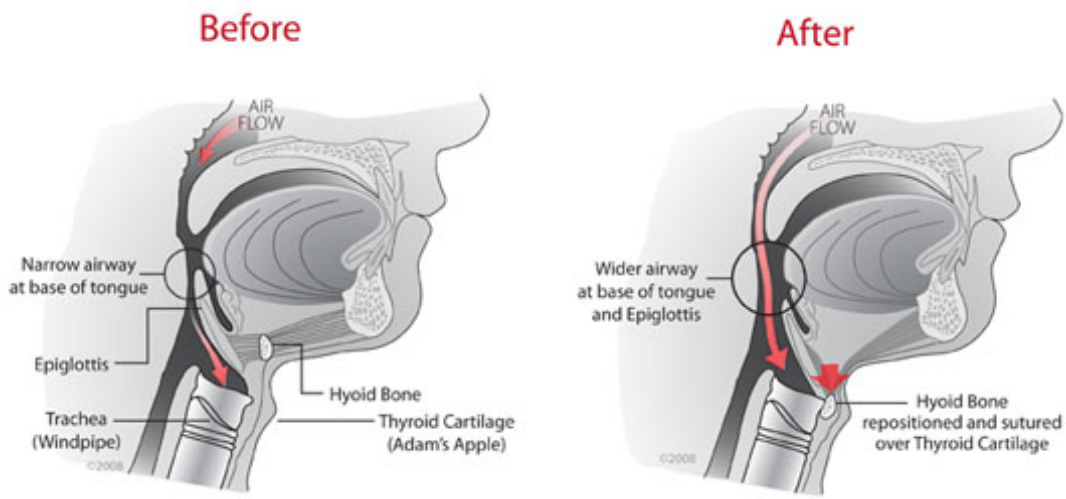

Figure 5: Hyoid Suspension [10].

1.2 INTERESTS

Because Obstructive sleep apnea affects such a large part of the population, methods which gives insight to understanding the disease is preferable. Today not only clinical studies has the ability to produce interesting results. New ways of understanding the human body is made available through biomechanical research and the use of computers. Investigation of scenarios to best describe and model diseases by means of computational multiphysics is also of interest. This field have lately gained popularity due to its applicability to describe problems from everyday issues to complex problems [6].

1.3 FRAMEWORK FOR MODELLING

Different models describing the problem of OSA has been proposed in the past. Due to the complexity of the problem it can be difficult to describe adequately. Not only can the airflow through the nasal and mouth cavity be cumbersome to characterize. It may become turbulent in some areas of the mouth and throat. Thus, realistically turbulence models need to be employed.

By making this a engineering problem it can be crucial to define proper initial and boundary conditions. To get realistic flow conditions it may be essential to be able to set the initial and boundary conditions at a distance to the phenomena which is to be observed. From a CFD point of view, when modelling the case of OSA it might not be satisfactory to describe the flow only through lesser parts of the upper airway.

To make a simpler model some assumptions can be made. For instance if the material of the tongue is considered homogeneous, elastic and isotropic the properties have a constant Young's modulus, E and Poisson ratio, ν [25]. These properties are defined later in [Chapter 4]. Whenever simplifications are made some drawbacks to the realism is also made. Different material properties, linear or non-linear behaviour produce various results. For instance, the mechanical properties of the tongue can best be described as inhomogeneous and anisotropic [25].

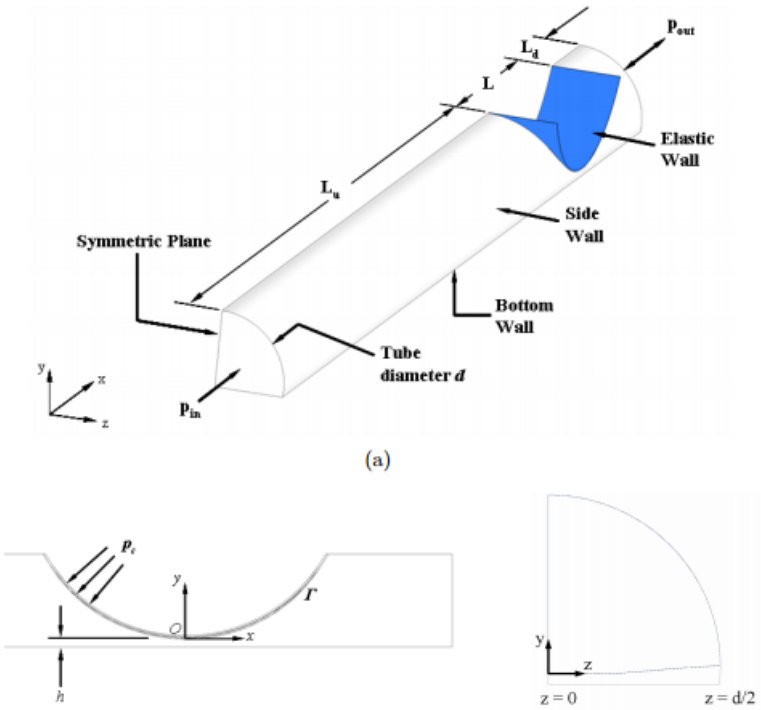

Figure 6: Suggested schematics of model [35].

A simplification of the problem of OSA has been done by Rasani, Inthavong, and Tu [35]. The physiological mechanisms in the pharyngeal airway are very closely related to the flow in compliant tubes [25]. The partial collapse of the airway and a nonlinear flow rate retardation is reassembling the phenomena of flow rate limitation. The narrowing of the airway in the pharynx leads to increased transmural pressure via the venturi effect (Giovanni Battista Venturi, 1746–1822). The effect can be derived from Bernoulli's equation [40]. If boundary deformation is to be accounted for, such as by use of a conforming mesh discussed later in [Chapter 3], an Arbitrary Lagrangian-Eulerian (ALE) method can be used.

As partly mentioned in [Section 1.2], it should be noted that a simple model reassembling the one by Rasani, Inthavong, and Tu [Figure 6] might not account for the behavior of the flow prior to the oropharynx. The changing behavior of the airflow going through the oral cavity and also the nasal cavity is likely to be of importance when reaching the pharynx. Thus, it may be difficult to accurately define inlet and outlet conditions and account for turbulent flow.

To proper define an problem description is important in any case of simulating. Especially in complex cases such as OSA. Nevertheless, the methods and applications for solving such a problem description is also of interest. This is of particular concern in this report. The depth of which will be presented in part II and following chapters.

Part II

THEORY

In part II the theory of the thesis is presented. The primary objective of this part is to set a general foundation for the FSI workings and applications. First an introduction to FSI's role in the area of multiphysics is presented. A state of the art fluid and solid mechanics analysis will then be given. The capability and applications of computational fluid dynamics (CFD) and finite element analysis (FEM) will be evaluated in light of modelling the problem of OSA.

2 MULTIPHYSICS

2.1 BASIS OF MULTIPHYSICS

Multiphysics applies almost everywhere in engineering, sciences and medicine, and even in our daily lives [6]. The expression however might be confusing. After all there is only one set of physical laws, and nothing multiple about it. Many phenomenas in the world is multiphysical in nature. Meaning different domains and forces interact with each other simultaneously. These systems have the potential to best be described by computational simulations. Before computers were able, physical effects were often observed and described in isolation. With the developing of tools capable of solving coupled systems the area of multiphysics has been enhanced.

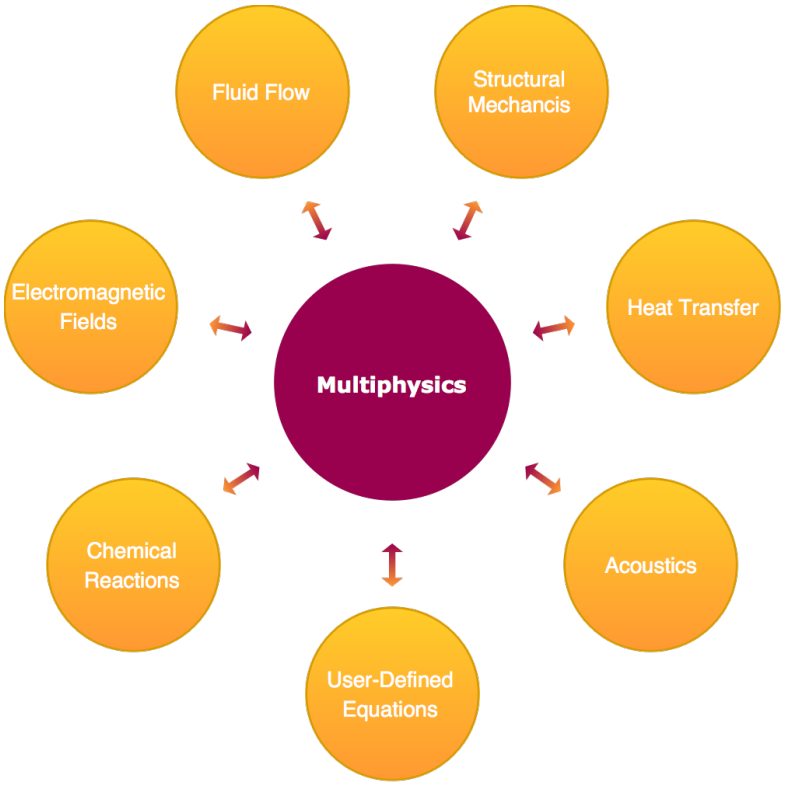

Figure 7: Multiphysic domains [23].

The coupling of systems is defined by COMSOL Inc. as follows

- *Coupled physcial phenomena in computer simulation.*

- *The study of multiple interacting physical properties.*

By examining the multiple forces in play the effects of these in combination and in isolation may be investigated. The analysis of corresponding coupled systems may be most challenging and is intended to be solved by numerical methods.

One particular interesting and challenging area in multiphysics is fluid-structure interactions (FSI). Predictive FSI methods to solve problems involving coupling of fluid flow with structural mechanics is highly demanded in many fields of interest [6]. In ordinary engineering problems however, effects of FSI is often negligible, due to minute traction forces or very stiff structures. In the case of bio-mechanical engineering the effects should not be disregarded and an efficient FSI solver is beneficial.

In coupled multiphysics problems, such as FSI, changes in one subsystem causes a response in other subsystems. Like most fields in engineering, FSI analysis types can be divided into three main categories, represented in [Figure 8].

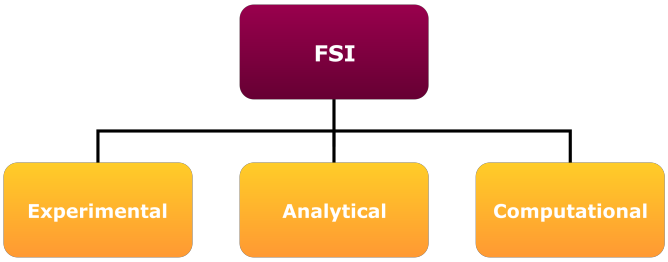

Figure 8: Main FSI categories.

Experimental analysis is perhaps the most rewarding and trustworthy analysis. It is often used for validation of numerical analysis, but has limits in costs and in some cases the constraints on scaling. For instance such as simultaneously satisfying Reynolds and Froude numbers criteria in complex tests.

Analytcial solutions is seldom found for all, but rather for a limited set of problems. These are substantial in order to understand the problem and for the validation of numerical solvers. While there are some use of analytic methods in solution of fluid- and structure-only problems. The inherently nonlinear and time-dependent nature of FSI makes it very difficult to apply analytic methods to [6].

Computational FSI analysis has the advantage of potentially requiring low resources. Due to advances in computational power and numerical algorithms, increasingly complex problems can be simulated [7]. Despite these suggestions, issues in the efficiency and the stability of certain FSI problems remain. These challenges relies among others upon; problem formulation, fluid-structure coupling, numerical discretization, software modularity and the effectiveness of computational architecture.

3

MESH DISCRETISATION

3.1 INTRODUCTION

In applying a computational FSI to a problem description one needs to choose an appropriate kinematic description of the continuum, managing the dynamics of both the fluid and the structure. There are several reference frames or coordinate systems to be considered for mesh forming. The governing equations of motion are generally described from either an Eulerian or a Lagrangian point of view [6]. Deformation and movement are factors to be considered.

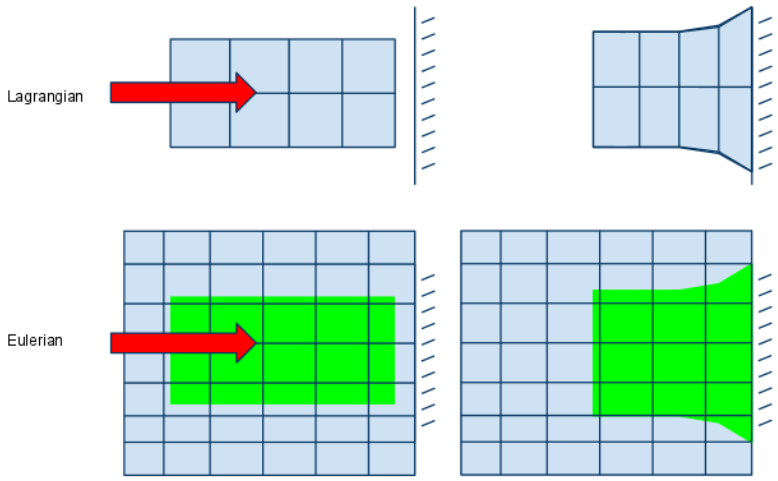

Figure 9: Lagrangian and Eulerian reference frame [41].

3.2 EULERIAN FORMULATION

The Eulerian formulation, in FSI also known as the immersed boundary method, use a fixed formulation of coodrinates. An Eulerian frame is fixed in space and the continuum moves with respect to the grid. In the Eulerian description, large distortions in the continuum motion can be handled with relative ease. For this reason, the Eulerian frame is used widely in fluid dynamics. A disadvantage is that the interface is not tracked accurately, which for FSI problems is of importance. Also it generally comes at the expense of the resolution of flow details. Where high gradients are expected, a fine mesh is needed. Thus it may not satisfy the need for accuracy when handling vortex induced flow, nor the case of OSA where pressure gradients are of particular interest. However, considering problems of large mesh displacements the method is often able to perform more stable and less time consuming simulations [5].

3.3 LAGRANGIAN FORMULATION

A Lagrangian frame moves with the material. The Lagrangian description makes it possible to track back loading history of the material, and therefore, suitable when working with material with history dependent behavior. Easily tracking free surfaces and interfaces between materials yield accurate material displacements. Large deformations however, lead to mesh tangling implying a less precise solution. Remeshing is needed in this case, which in particular for a 3D case often proves computational expensive. When considering materials which is highly elastic, deformations are relatively smaller and the Lagrangian frame is attractive. For this reason, the Lagrangian frame is used widely in structure mechanics.

3.4 ARBITRARIAN LAGRANGIAN-EULERIAN METHOD

The Abitrary Lagrangian-Eulerian (ALE) method is one of the most commonly used methods for capturing the interaction between structure and fluid [27]. This method is a combination of the classical two descriptions of motion, the Lagrangian motion and the Eulerian motion, with the purpose to summon their respective advantages and minimize their disadvantages.

The ALE description offers freedom in moving the computational mesh and large distortions of the continuum can be handled with high resolution and accuracy. Nodes either follow the continuum as in the Lagrangian description, are fixed as in Eulerian description or move arbitrary to get continuously re-zoning capability. An ALE description can be used in order to account for boundary deformation and, thus, deformation of the fluid mesh. The result is a computational mesh that can avoid large mesh distortion with good resolution.

Different ways of formulating the frame of reference when modelling FSI have been proposed in the past, each having its advantages and disadvantages. The Arbitrary Lagrangian Eulerian method have the advantage of providing a strong coupling, explained further in [Section 6.3.2]. As long as rotations, translations and/or deformations of the solid remain within certain limits, this method works very well and is recommended [27]. However, for problems in which these limits are violated, elements become ill-shaped and ALE alone does not suffice. As a solution to this problem an often used combination is ALE with some form of re-meshing. This can however, be a difficult and time consuming task [26]. Also the relocation of solutions from the old mesh to the new mesh may create artificial diffusion, resulting in loss of accuracy.

3.5 MESH GENERATION

The FSI solution procedures is based on the handling and conforming of meshes. Two distinct method exists; the *conforming mesh methods* and *non-conforming mesh methods* [17]. These bases on the Lagrangian and Eulerian formulations, respecively. The conforming mesh methods consists of using the interface between the solid and fluid domain as a physical boundary. Hence adopting the interface as a part of the solution. When movement or deformation is done to the solid, a mesh update is required to solve the next step.

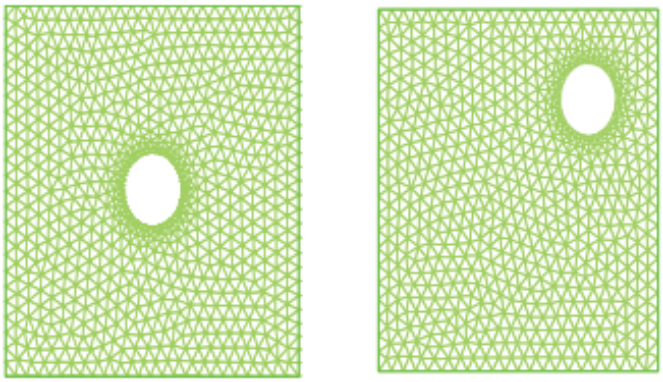

(a) Conforming mesh. Left $t = t_1$; Right $t = t_2$.

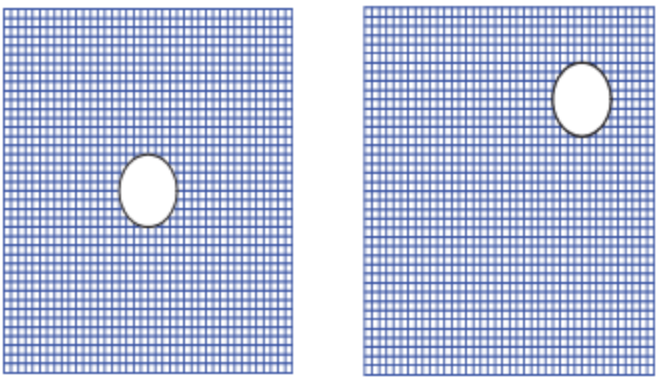

(b) Non-conforming mesh. Left $t = t_1$; Right $t = t_2$.

Figure 10: Solid sphere moving in fluid [17].

The non-conforming mesh methods uses the interface location and the boundary conditions as constraints imposed on the model equations. Thus a mesh update is not needed since the fluid and solid equations can be solved independently within their own respective grids. The non-conforming mesh methods are based on the framework of the immersed methods (IB). The goal of the IB is to avoid mesh updates in the numerical procedure altogether. Thus minimizing computational effort and time needed.

4 SOLID MECHANICS

4.1 INTRODUCTION

The following sections will state and briefly explain the governing equations of the structure. Much of its content is based on the the free and open educational book by *Saravanan, U., 2013* [39]. The structural equations to model the deformation of the solid are derived.

4.2 MATERIAL

An elastic material has the ability to resist a distorting influence or deforming force and to return to its original size and shape when that influence or force is removed. When describing the relative elasticities of a material, both the modulus and the elastic limit have to be considered.

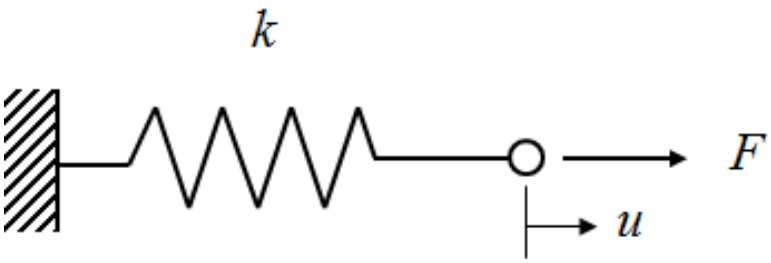

Figure 11: A 0-D representation using lumped stiffness.

Most elastic materials such as springs exhibit linear elasticity and can be described by a linear relation between the stress and strain. This relationship is known as Hookes law which can be stated as a relationship between tensile force $\mathbf{F}$ and corresponding displacement $\mathbf{x}$.

$$\mathbf{F} = k\boldsymbol{x} \tag{1}$$

The elastic components, as previously mentioned, can be modeled as springs of elastic constant E, given by the formula

$$\sigma = E\varepsilon \tag{2}$$

where σ is the normal stress in [Pa], E is the elastic modulus of the material in [Pa] and ε is the strain that occurs under the given stress.

4.3 STRUCTURE EQUATIONS

The equations of the structure come from the conservation of momentum and material model for elasticity.

4.3.1 *Rigid body motion*

For a solid which is assumed rigid its motion is governed by the six equations of motion. In 2D cases the equations are reduced to three. Euler's equations states that

$$\mathbf{M} = \mathbf{I}\dot{\boldsymbol{\omega}} + \boldsymbol{\omega} \times (\mathbf{I} \cdot \boldsymbol{\omega}) \tag{3}$$

where I is the moments of inertia in tensor form, ω the angular velocity vector, o$\dot{\text{m}}$ega the angular acceleration vector and $\mathbf{M}$ is the moment about the center of mass [34].

In this case the problem is an initial value problem. Hence, there are no boundary conditions. By integrating the pressure and shear stress over the surface of the body the sum of the force and moment can be obtained.

$$\mathbf{F} = \int_A p n_s \, dA + \int_A \tau_s \, dA \tag{4}$$

$$\mathbf{M} = \int_A p r \times n_s \, dA + \int_A r \times \tau_s \, dA \tag{5}$$

4.3.2 *Conservation of momentum*

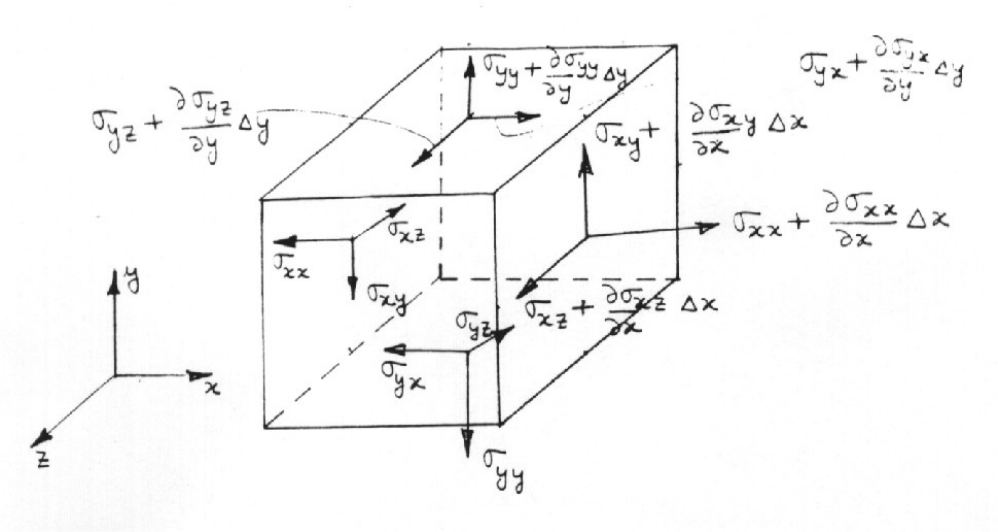

Figure 12: Components of stress

Two kinds of forces can be experienced in a body. These are

- Contact forces
- Body forces

This is described by - *Anderson, 1995* [2] as

- *Body forces, which act directly on the volumetric mass of the element. These forces "act at a distance"; examples can be gravitational and electromagnetic forces.*
- *Surface forces, which act directly on the surface of the element. They are only due to two sources.*
  - *The pressure distribution acting on the surface, imposed by the outside fluid surrounding the element.*
  - *The shear and normal stress distributions acting on the surface, also imposed by the outside fluid by means of friction.*

Assume that the Cauchy stress, $\boldsymbol{\sigma}$ varies over an infinitesimal element in the current configuration [39]. When expanding the Cartesian components of the stresses using Taylor's series up to first order in 2D, the directional components are

$$\begin{aligned}
\sigma_{xx}(x+\Delta x, y) &= \sigma_{xx}(x,y) + \left.\frac{\partial \sigma_{xx}}{\partial x}\right|_{x,y} \Delta x \\
\sigma_{xy}(x+\Delta x, y) &= \sigma_{xy}(x,y) + \left.\frac{\partial \sigma_{xy}}{\partial x}\right|_{x,y} \Delta x \\
\sigma_{yx}(x, y+\Delta y) &= \sigma_{yx}(x,y) + \left.\frac{\partial \sigma_{yx}}{\partial y}\right|_{x,y} \Delta y \\
\sigma_{yy}(x, y+\Delta y) &= \sigma_{yy}(x,y) + \left.\frac{\partial \sigma_{yy}}{\partial y}\right|_{x,y} \Delta y
\end{aligned}$$

The equilibrium of forces for the element is due to the stresses and body forces it experience. From [Figure 12] it follows that the equilibrium forces in the x-direction gives

$$\begin{aligned}
\text{Net forces} = &\left[\sigma_{xx}(x,y) + \left.\frac{\partial \sigma_{xx}}{\partial x}\right|_{x,y} \Delta x - \sigma_{xx}(x,y)\right] \Delta y \\
&+ \left[\sigma_{yx}(x,y) + \left.\frac{\partial \sigma_{yx}}{\partial y}\right|_{x,y} \Delta y - \sigma_{yx}(x,y)\right] \Delta x + \rho b_x \Delta x \Delta y = 0
\end{aligned}$$

where ρ is the density of the element and b_x is the body force in the x-direction. Analogues to the x-direction this can also be done in the y-direction. When the higher order Taylor expansions $\left[+ \frac{\partial \sigma_*}{\partial(x,y,z)}\Big|_{(x,y,z)} \Delta(x,y,z)\right]$ is neglected the equation simplifies to

$$\frac{\partial \sigma_{xx}}{\partial x} + \frac{\partial \sigma_{yx}}{\partial y} + \rho b_x = 0. \tag{6}$$

Note that this method is used throughout all deductions on infinitesimal scale. In the 3D case the equilibrium forces in the x-direction is (in other notations)

$$\begin{aligned}\text{Net forces} = &\left[\sigma_{xx} + \frac{\partial \sigma_{xx}}{\partial x}\Delta x\right]\Delta y\Delta z - \sigma_{xx}\Delta y\Delta z \\ &+ \left[\sigma_{yx} + \frac{\partial \sigma_{yx}}{\partial y}\Delta y\right]\Delta x\Delta z - \sigma_{yx}\Delta x\Delta z \\ &+ \left[\sigma_{zx} + \frac{\partial \sigma_{zx}}{\partial z}\Delta z\right]\Delta x\Delta y - \sigma_{zx}\Delta x\Delta y + \rho g_x \Delta x\Delta y\Delta z = 0\end{aligned}$$

which when simplified becomes

$$\frac{\partial \sigma_{xx}}{\partial x} + \frac{\partial \sigma_{yx}}{\partial y} + \frac{\partial \sigma_{zx}}{\partial z} + \rho b_x = 0. \tag{7}$$

The total force in 3D can be written

$$\mathbf{F} = [\rho \mathbf{b} + \boldsymbol{\nabla} \cdot \boldsymbol{\sigma}] dx dy dz$$

Inserting $F = m\mathbf{a}$ and $m = \rho \ dxdydz$ and $\mathbf{b} = \mathbf{g}$ the result is

$$\begin{aligned}\rho \mathbf{a} \ dxdydz &= [\rho \mathbf{g} + \boldsymbol{\nabla} \cdot \boldsymbol{\sigma}] \ dxdydz \\ \rho \frac{D\mathbf{u}}{Dt} \ dxdydz &= [\rho \mathbf{g} + \boldsymbol{\nabla} \cdot \boldsymbol{\sigma}] \ dxdydz \\ \rho \frac{D\mathbf{u}}{Dt} &= \boldsymbol{\nabla} \cdot \boldsymbol{\sigma} + \rho \mathbf{g}\end{aligned} \tag{8}$$

which is the final expression for the conservation of linear momentum, also named as equilibrium equations [39]. Here the deviatoric stress $\boldsymbol{\sigma}_{dev}$ from $\boldsymbol{\sigma} = -p\mathbf{I} + \boldsymbol{\sigma}_{dev}$ is related to the material model used. The symbols $\mathbf{u}$, $\boldsymbol{\sigma}$, $\mathbf{f}$, $\boldsymbol{\nabla}$, p, $\mathbf{I}$, ρ, denote the velocity, Cauchy stress tensor, body force, gradient operator, pressure, and the unity tensor respectively.

4.3.3 *Deformation*

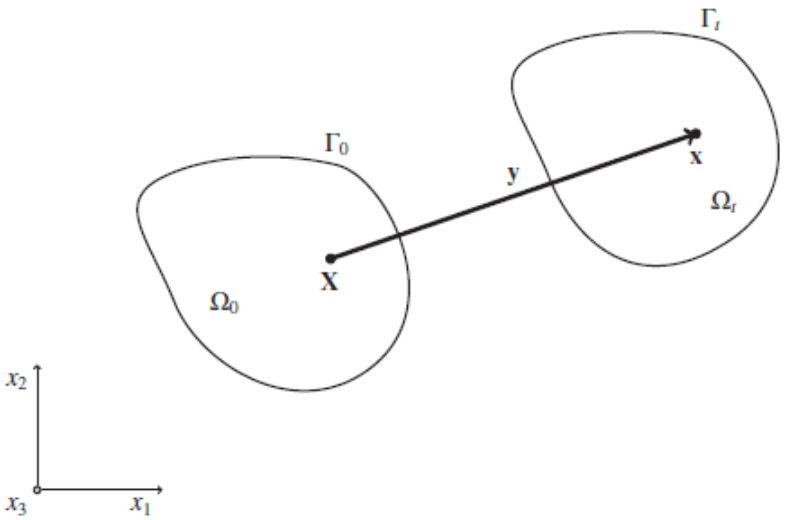

Figure 13: Reference and current configurations [6].

In [Figure 13], $\mathbf{X}$ is the coordinates of the initial or reference configuration at $t = 0$. A time-varying vector field over Ω_0 is defined $\mathbf{y} = \mathbf{y}(\mathbf{X}, t)$. A mapping between the coordinates of the material in the reference configurations to the current configuration can then be given as

$$\mathbf{x}(\mathbf{X}, t) = \mathbf{X} + \mathbf{y}(\mathbf{X}, t), \tag{9}$$

where $\mathbf{x}$ represents the coordinates of the current configuration.
The deformation gradient $\mathbf{F}$ is given by

$$\mathbf{F} = \frac{\partial \mathbf{x}}{\partial \mathbf{X}} = \mathbf{I} + \frac{\partial \mathbf{y}}{\partial \mathbf{X}}, \tag{10}$$

which can be used to define the Cauchy-Green deformation tensor $\mathbf{C}$ as

$$\mathbf{C} = \mathbf{F}^T\mathbf{F}, \tag{11}$$

and the Green-Lagrange strain tensor $\mathbf{E}$ as

$$\mathbf{E} = \frac{1}{2}(\mathbf{C} - 1). \tag{12}$$

Density of the solid is determined by the volume change [6]. This is the same as the determinant of the deformation gradient $\mathbf{J}$ which is given by

$$\mathbf{J} = \det(\mathbf{F}). \tag{13}$$

Using principal of virtual work the Cauchy stress tensor $\boldsymbol{\sigma}$ can be expressed as

$$\boldsymbol{\sigma} = \mathbf{J}^{-1}\mathbf{F}\mathbf{S}\mathbf{T}^{\mathsf{T}}. \tag{14}$$

Here the $\mathbf{S}$ is the second Piola-Kirchoff stress tensor. Since the Cauchy stress (and hence the Kirchhoff stress) is symmetric, the second Piola-Kirchoff stress is also symmetric. The structural mechanics variations formulation in the current configuration is

$$\int_{\Omega_t} w \cdot (\rho(\mathbf{a} - \mathbf{f}) - \boldsymbol{\nabla} \cdot \boldsymbol{\sigma} d\Omega + \int_{(\Gamma_t)_h} w \cdot (\boldsymbol{\sigma}\mathbf{n} - \mathbf{h}) d\Gamma = 0. \tag{15}$$

When equation (15) holds for all admissible w, the conclusion is

$$\rho(\mathbf{a} - \mathbf{f}) - \boldsymbol{\nabla} \cdot \boldsymbol{\sigma} = 0 \tag{16}$$

at every point inside Ω_t and

$$\boldsymbol{\sigma}\mathbf{n} - \mathbf{h} = 0 \tag{17}$$

at every point on the traction boundary, $(\Gamma_t)_h$ [6].

When the solid is not assumed rigid, three sets of equations are necessary. The first is already derived, the equilibrium of stresses.

$$\rho\frac{D\mathbf{u}}{Dt} = \boldsymbol{\nabla} \cdot \boldsymbol{\sigma} + \rho\mathbf{b} \tag{18}$$

For the cases studied in this thesis the only material model of relevance is the Linear Elasticity model. When in addition assuming isotropic material the model states

$$\boldsymbol{\sigma}_{ij} = \frac{E}{1+\nu}\left[\varepsilon_{ij} + \delta_{ij}\frac{\nu}{1-2\nu}\varepsilon_{kk}\right], \tag{19}$$

Here E is the Young's modulus, ν the Poisson's ratio and δ_{ij} the Kronecker delta.

The last equation is the strain relations

$$\varepsilon_{ij} = \frac{1}{2}\left(\frac{\partial \mathbf{u}_i}{\partial \mathbf{x}_j} + \frac{\partial \mathbf{u}_j}{\partial \mathbf{x}_i}\right) \tag{20}$$

where ε_{ij} is the strain and $\mathbf{u}_i$ is the displacement in the $\mathbf{x}_i$ direction.

4.3.4 *Initial and boundary conditions*

$$\begin{aligned} \rho \frac{D\mathbf{u}}{Dt} &= \boldsymbol{\nabla} \cdot \boldsymbol{\sigma} + \rho \mathbf{b} \\ \det(\mathbf{F}) &= 1 \\ \boldsymbol{\sigma} &= G(\mathbf{F} \cdot \mathbf{F}^T - \mathbf{I}) - p\mathbf{I} \end{aligned} \tag{21}$$

In the above equations the symbol G denote the solid shear modulus. The system of equations in (21) are the momentum balance, the continuity and the constitutive relation describing the rheological behaviour of the fluid and solid, respectively [27]. To solve the system (21) two IC's and one BC is needed. This is the initial displacement and velocity of the solid and the pressure p on the solid boundary. Where the solid is in contact with air the deformation and velocity can be assumed zero initially. The pressure p need not be considered because it is a function of the surrounding density of the fluid ρ and the internal energy e. These necessary conditions are provided from the fluid [2].

5

FLUID DYNAMICS

5.1 INTRODUCTION

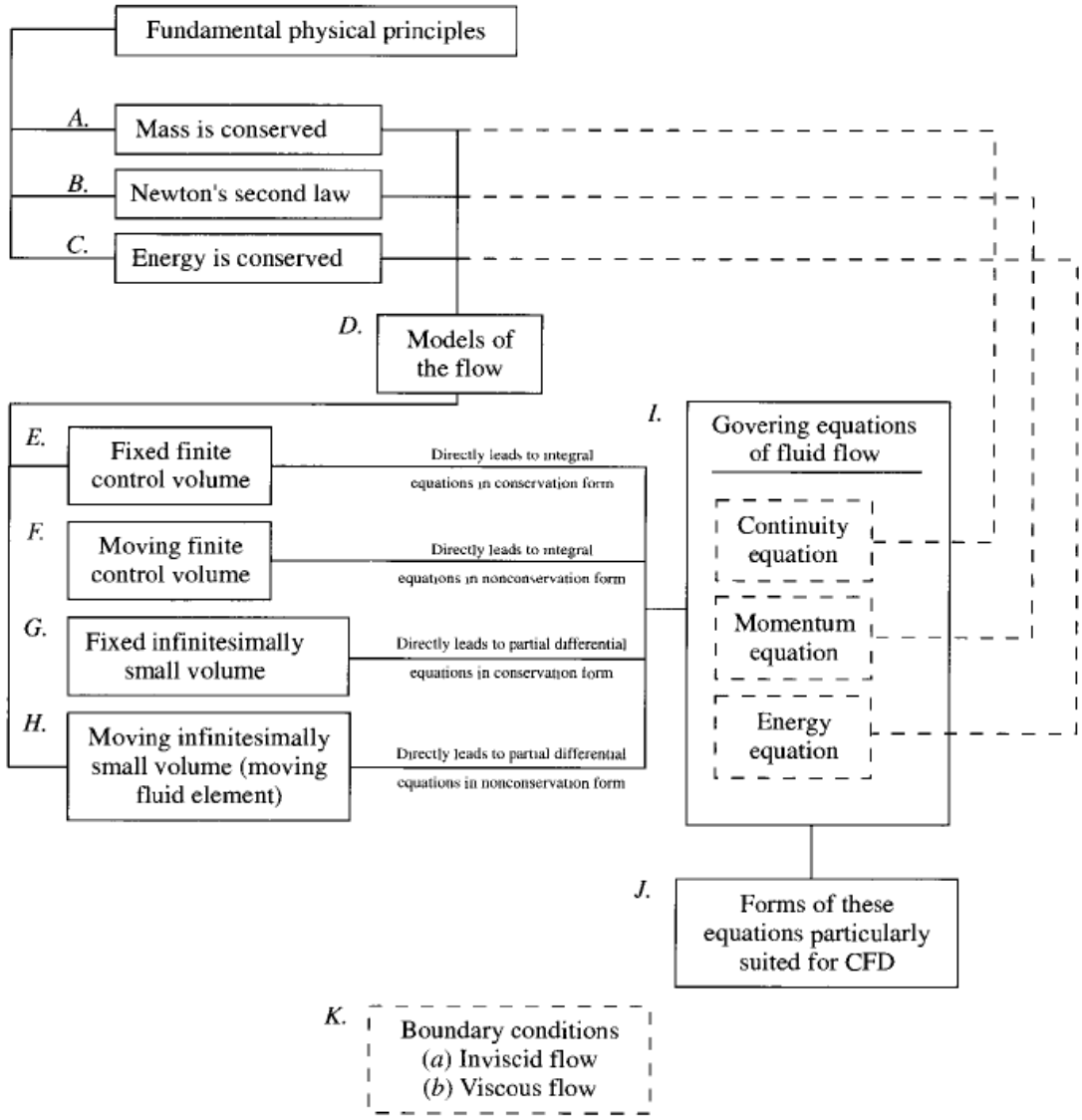

Figure 14: Roadmap of fundamental principles [2].

Three fundamental equations lay the groundwork for all fluid dynamics.

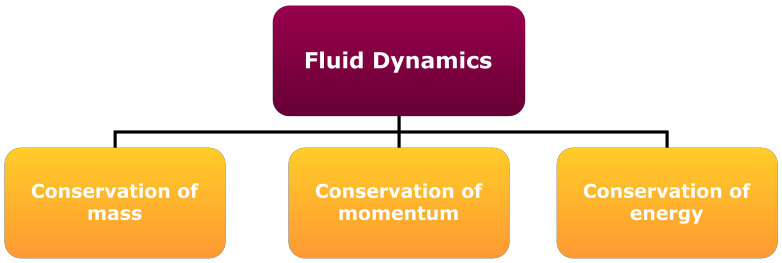

Figure 15: The fundamental principles of fluid dynamics.

These principles shown in [Figure 15] are the continuity from mass conservation, momentum form Newtons's second law and the energy equation from conservation of energy. These equations can be deduced in both an Eulerian and a Lagrangian frame.

Much of the material in this chapter bases on the book by *Anderson JR., 1995* [2], which was first found trough a secondary source [43]. This excellent book was acquired and used to a great extent in the following sections.

Considering the case of *Flow Induced Oscillations of a Flexible Beam* [Chapter 8] and the OSA palate model [Chapter 9] assumptions for the flow are made. Coherent to [Chapter 4], the governing equations of flow are deduced and explained.

5.2 REFERENCE FRAME AND SCALE

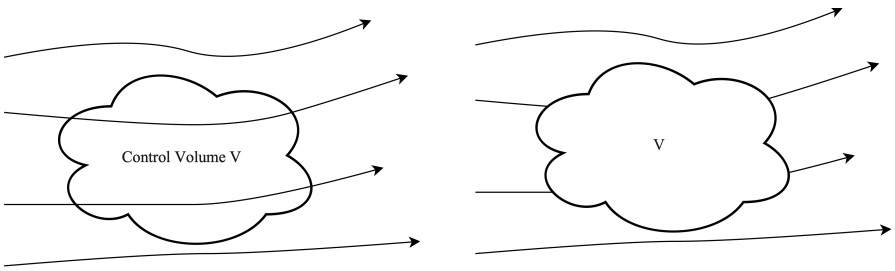

Figure 16: Fixed finite control volume to the left. Moving control volume to the right [2].

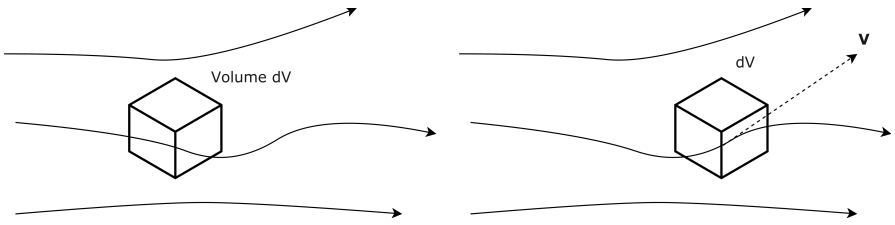

Figure 17: Fixed infinitesimal control volume to the left. Moving infinitesimal control volume to the right [2].

In [Figure 16] the finite control volume to the left is fixed in space with the fluid moving through it. The finite control volume to the right is moving with the fluid such that the same fluid particles are always in the same control volume. In [Figure 17] the infinitesimal fluid element is fixed in space with the fluid moving through it. The image to the right in the same figure shows the infinitesimal fluid element moving with the velocity V along a streamline. The velocity V is equal to the local flow velocity at each point.

In fluid dynamics different scales with different reference frames can be used. The scale can either be continuum or infinitesimal. The reference frame can either be fixed in space or moving with the fluid. These are called the Eulerian and Lagrangian frame of reference, respectively. By applying fundamental physical principles to a finite control volume fluid flow equations on integral form can be deduced. These governing equations can then be manipulated to get partial differential equations [2].

5.3 CONSERVATION OF MASS

5.3.1 *Continuum scale with fixed frame*

Consider a control volume of arbitrary shape and of finite size fixed in space like the left model in [Figure 16]. The fluid moves through the volume, across the surface. Mass conservation can in this case be described as in [Figure 18].

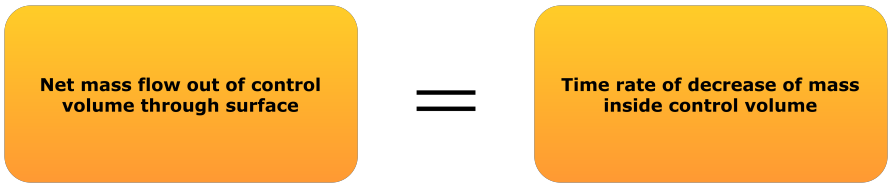

Figure 18: Conservation of mass [2].

In mathematical terms the net mass flow out of the control volume through the surface $\partial V = S \subseteq \mathbb{R}^3$ in $[m^2]$ can be described by

$$\iint_S \rho \boldsymbol{v} \cdot \boldsymbol{n} dS$$

where $\boldsymbol{v}, \boldsymbol{n} \in \mathbb{R}^3$ the velocity in $[\frac{m}{s}]$ and normal to the closed surface S respectively.

The time rate of decrease of mass inside volume $V \subseteq \mathbb{R}^3$ in $[m]^3$ is given by

$$-\frac{\partial}{\partial t} \iiint_V \rho dV.$$

Then

$$\frac{\partial}{\partial t}\iiint_V \rho dV + \iint_S \rho \mathbf{v}\cdot\mathbf{n}dS = 0 \tag{22}$$

which is the mass conservation in integral form [2].

5.3.2 *Infinitesimal scale with fixed frame*

Consider a control volume of arbitrary shape and of finite size fixed in space like the one in [Figure 17]. The fluid moves through the volume, across the surface. The mass conservation in this case can be described in the same way as for the continuum scale [Figure 18].

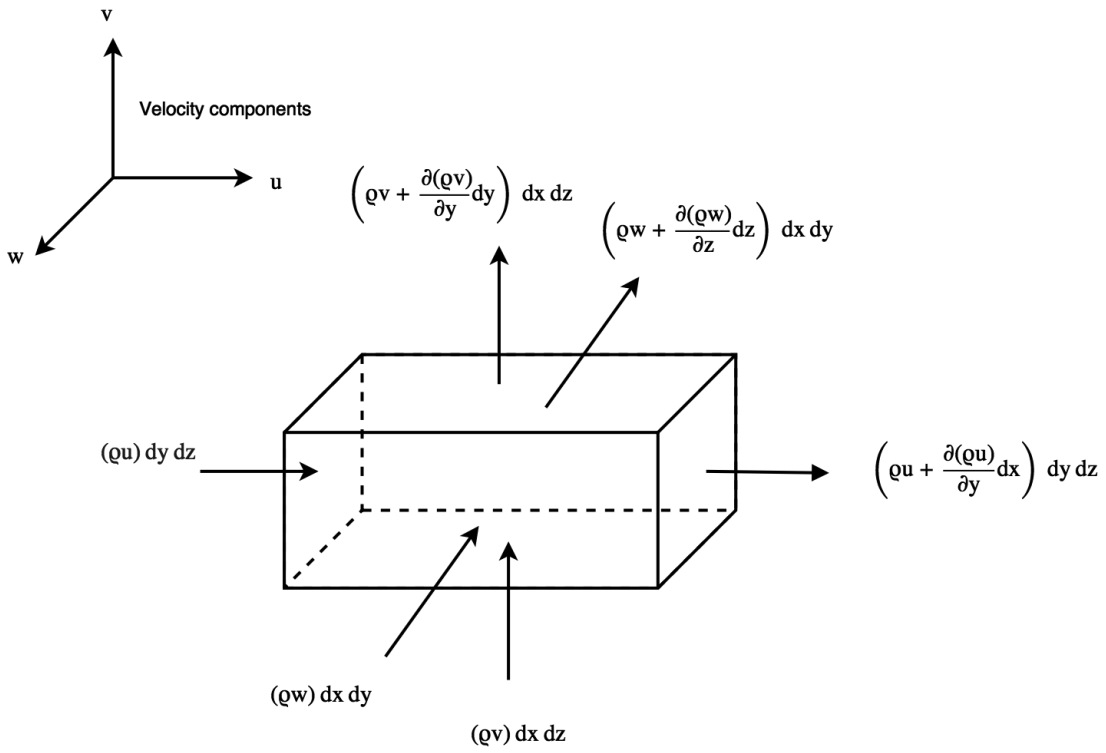

Figure 19: Model of infinitesimal element fixed in space [2].

The infinitesimal element is a cube [Figure 19]. Thus the consideration of direction is simpler than the continuum scale. Net outflow in the x-direction is

$$(\rho u)\,|_{x+dx}\,dydz - (\rho u)\,|_x\,dydz$$

Since dx is infinitesimal, the higher order terms of the taylor expansion can be neglected. This produces $(\rho u)|_x + dx\,\frac{\partial(\rho u)}{\partial x}\Big|_x$. Thus the net outflow in the x direction becomes

$$(\rho u)\,|_{x+dx}\,dydz-(\rho u)\,|_x\,dydz=\left[(\rho u)|_x+dx\,\frac{\partial(\rho u)}{\partial x}\bigg|_x\right]dydz-(\rho u)\,|_x\,dydz$$
$$=\frac{\partial(\rho u)}{\partial x}\bigg|_x dxdydz$$

The same procedure can be used in the y and z directions. When the mass decrease is set to a negative quantity and assuming constant density ρ in space, the statement can be expressed as

$$\left[\frac{\partial(\rho u)}{\partial x}\bigg|_x+\frac{\partial(\rho v)}{\partial y}\bigg|_y+\frac{\partial(\rho w)}{\partial z}\bigg|_z\right]dxdydz=-\frac{\partial\rho}{\partial t}dxdydz$$
$$\frac{\partial\rho}{\partial t}+\left[\frac{\partial(\rho u)}{\partial x}\bigg|_x+\frac{\partial(\rho v)}{\partial y}\bigg|_y+\frac{\partial(\rho w)}{\partial z}\bigg|_z\right]=0$$

which when the terms in the brackets is identified as $\boldsymbol{\nabla}\cdot(\rho\boldsymbol{v})$, leads to

$$\frac{\partial\rho}{\partial t}+\boldsymbol{\nabla}\cdot(\rho\boldsymbol{v})=0. \tag{23}$$

This is the continuity equation on a partial differential form. The equation is obtained directly in partial form because of the infinitesimal small aspect of the element. Since the element is assumed fixed in space it leads to the specific differential form. Which is named the conservation form [2].

5.3.3 *Continuum scale with moving frame*

In the figure to the right in [Figure 16] the element is moving with the fluid. In this case mass conservation can be described as

$$\frac{D}{Dt}\iiint_V\rho dV=0 \tag{24}$$

During the inteval Dt the particle stay the same. The material derivative is given by

$$\frac{D}{Dt}=\frac{\partial}{\partial t}\bigg|_{\text{particle}}$$
$$=\frac{\partial}{\partial t}\bigg|_{\text{space position}}+\sum_{i=1}^{3}\frac{\partial x_i}{\partial t}\bigg|_{\text{particle}}\frac{\partial}{\partial x_i}. \tag{25}$$

The density is thus

$$\begin{aligned}\frac{D}{Dt}\rho(x(t),y(t),z(t),t) &= \frac{\partial}{\partial t}\rho(x(t),y(t),z(t),t)\Big|_{\text{particle}} \\ &= \frac{\partial}{\partial t}+\frac{\partial\rho}{\partial x}\frac{\partial x}{\partial t}+\frac{\partial\rho}{\partial y}\frac{\partial y}{\partial t}+\frac{\partial\rho}{\partial z}\frac{\partial z}{\partial t} \\ &= \frac{\partial\rho}{\partial t}+\rho\boldsymbol{\nabla}\cdot\boldsymbol{v}. \end{aligned} \tag{26}$$

5.3.4 *Infinitesimal scale with moving frame*

A infinitesimal fluid element moving with the flow is represented in the right part of [Figure 17]. The element shape and volume will change as it moves with the stream. The mass of the element however is fixed. The variable volume and fixed mass for this element can be expressed by ∂m and ∂V respectively,

$$\partial m = \rho\partial V. \tag{27}$$

Since the element is moving with the fluid, again the notation of material derivative can be used [2]. As in the continuum scale case, the rate of change of the mass in time is equal to zero. Thus

$$\frac{D(\partial m)}{Dt} = 0 \tag{28}$$

$$\tag{29}$$

Combining this with equation (27),

$$\begin{aligned}\frac{D(\rho\partial V)}{Dt} &= 0 \\ \partial V\frac{D\rho}{Dt}+\frac{D(\partial V)}{Dt} &= 0 \\ \frac{D\rho}{Dt}+\frac{\rho}{\partial V}\cdot\frac{D(\partial m)}{Dt} &= 0 \end{aligned} \tag{30}$$

By using the divergence theorem, which in physical meaning states $\frac{1}{\partial V}\cdot\frac{D(\partial V)}{Dt}=0$, the equation finally becomes

$$\frac{D\rho}{Dt}+\rho\boldsymbol{\nabla}\cdot\boldsymbol{v}=0. \tag{31}$$

5.3.5 *Unity in the equations*

A total of four equations have been deduced, (22), (23), (24) and (31). These are four equations in integral or partial differential form, for either the conservative or non-conservative case. The equations are not fundamentally different,

but rather four different forms of the same equation; the continuity equation. For instance, with some manipulations the integral form of equation (22) can yield the differential form of equation (23).

One of the main difference is that the partial differential forms assume first order differentiability, implying continuity. While the integral forms allow the presence of discontinuities inside the fixed control volume. Therefore the integral form is considered to be more fundamental than the partial differential form [2].

5.4 CONSERVATION OF MOMENTUM

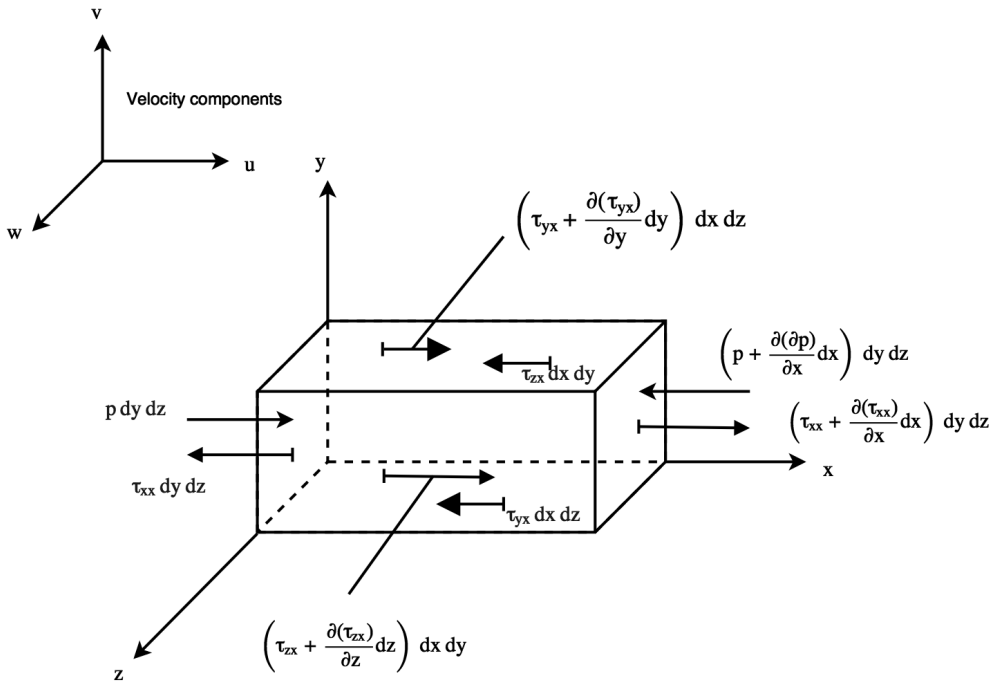

Figure 20: Forces in the x-direction [2].

Considering a moving infinitesimal fluid element, it can experience both body and surface forces. Newton's second law states $\mathbf{F} = m\mathbf{a}$. As a reminder from [Chapter 4], when considering a moving infinitesimal fluid element, it can also experience body and/or surface forces [2].

Let $\mathbf{f}$ denote the body force per unit mass, then

$$\text{body force on fluid element} = \rho \mathbf{f} \ dxdydz.$$

From [Figure 20] it follows that the net surface forces (abbreviated NSF) in the x-direction can be given as

$$\begin{aligned}
NSF_x = &\left[p - \left(p + \frac{\partial p}{\partial x}dx\right)\right] dydz + \left[\left(\tau_{xx} + \frac{\partial \tau_{xx}}{\partial x}dx\right) - \tau_{xx}\right] dydz \\
&+ \left[\left(\tau_{yx} + \frac{\partial \tau_{yx}}{\partial y}dy\right) - \tau_{yx}\right] dxdz + \left[\left(\tau_{yz} + \frac{\partial \tau_{zx}}{\partial z}dz\right) - \tau_{zx}\right] dxdy \\
&= \left[-\frac{\partial p}{\partial x} + \frac{\partial \tau_{xx}}{\partial x} + \frac{\partial \tau_{yx}}{\partial t} + \frac{\partial \tau_{zx}}{\partial z}\right] dxdydz
\end{aligned}$$

When again neglecting the Taylor expansions terms the total force becomes

$$\begin{aligned}
\mathbf{F} &= \left[-\boldsymbol{\nabla} p + \begin{pmatrix} \frac{\partial \tau_{xx}}{\partial x} + \frac{\partial \tau_{yx}}{\partial y} + \frac{\partial \tau_{zx}}{\partial z} \\ \frac{\partial \tau_{xy}}{\partial x} + \frac{\partial \tau_{yy}}{\partial y} + \frac{\partial \tau_{zy}}{\partial z} \\ \frac{\partial \tau_{xz}}{\partial x} + \frac{\partial \tau_{yz}}{\partial y} + \frac{\partial \tau_{zz}}{\partial z} \end{pmatrix} + \rho \mathbf{f}\right] dxdydz \\
&= \left[-\boldsymbol{\nabla} p + (\boldsymbol{\nabla} \cdot \tau)^T + \rho \mathbf{f}\right] \; dxdydz
\end{aligned}$$

The last term $(\boldsymbol{\nabla} \cdot \tau)^T$ is the divergence of the matrix, $div(\tau)$. Defining $\mathbf{F} = m\mathbf{a}$ and setting $m = \rho \; dxdydz$, $\mathbf{a} = \frac{D\boldsymbol{v}}{Dt}$ and the stress tensor $\boldsymbol{\sigma_{dev}} = \boldsymbol{\sigma}_{dev}^T$ the equation may further be developed to

$$\begin{aligned}
\rho \frac{D\boldsymbol{v}}{Dt} dxdydz &= \left[-\boldsymbol{\nabla} p + (\boldsymbol{\nabla} \cdot \boldsymbol{\sigma}_{dev}) + \rho \mathbf{f}\right] \; dxdydz \\
\rho \frac{D\boldsymbol{v}}{Dt} &= -\boldsymbol{\nabla} p + \boldsymbol{\nabla} \cdot \boldsymbol{\sigma}_{dev} + \rho \mathbf{f} \qquad (32)
\end{aligned}$$

Which are the Navier-Stokes equations in non-conservation form. The the conservation form can be deducted

$$\rho \left(\frac{\partial \boldsymbol{v}}{\partial t} + (\boldsymbol{v} \cdot \boldsymbol{\nabla})\boldsymbol{v}\right) = -\boldsymbol{\nabla} p + \boldsymbol{\nabla} \cdot \boldsymbol{\sigma}_{dev} + \rho \mathbf{f} \qquad (33)$$

5.4.1 *Shear stresses*

Fluids like water and air is often considered Newtonian. Isaac Newton described the flow behavior of fluids with a simple linear relation between shear stress $[mPa]$ and shear rate $[\frac{1}{s}]$. This relationship is now known as Newton's Law of Viscosity.

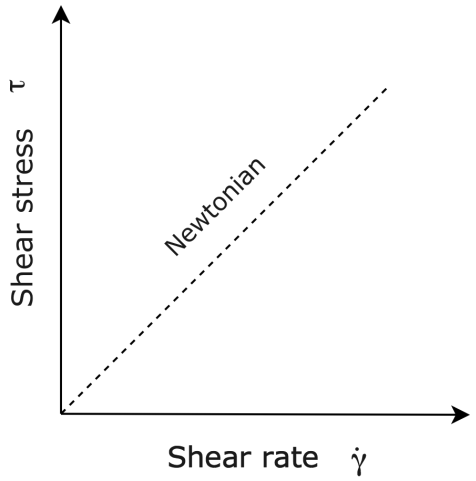

Figure 21: Shear stress as a function of shear rate.

When the fluid is assumed Newtonian

$$\underbrace{\tau}_{\text{Shear stress}} = \underbrace{\mu}_{\text{viscosity}} \times \underbrace{\dot{\gamma}}_{\text{Shear rate}}$$

where the the proportionality constant μ is the molecular viscosity $[Pa \cdot s]$ of the fluid. The molecular viscosity is also a function of temperature.

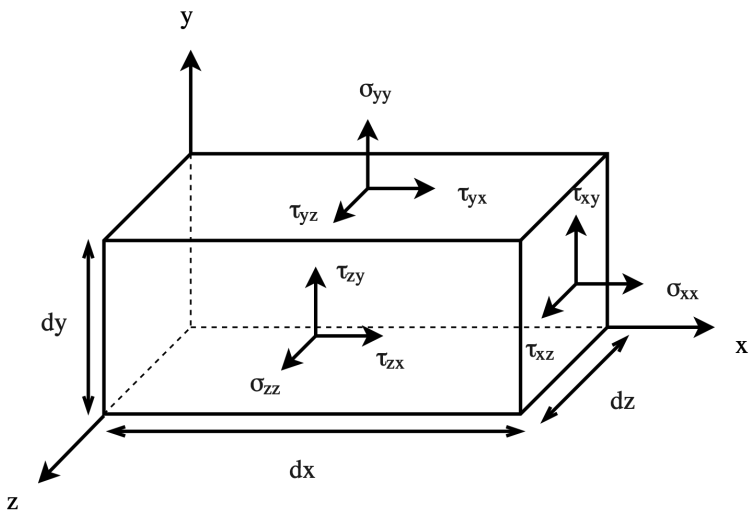

Figure 22: Force components of the stress tensor on an infinitesimal element [39].

Considering the infinitesimal element of a viscous fluid with a stress tensor such as the one in [Figure 22]. Here the tensor may be written as

$$\boldsymbol{\sigma} = \begin{bmatrix} \sigma_{xx} & \tau_{xy} & \tau_{xz} \\ \tau_{yx} & \sigma_{yy} & \tau_{yz} \\ \tau_{zx} & \tau_{zy} & \sigma_{zz} \end{bmatrix}$$

When the fluid is in equilibrium, the tensor is symmetric, $\tau_{ij} = \tau_{ji}$. This is true of Newtonian fluids, in which the shear stresses are proportional to the rate of shearing by the constant μ. The stresses can be described as

$$\tau_{ij} = \tau_{ji} = \mu \left(\frac{\partial u_i}{\partial x_j} + \frac{u_j}{x_i} \right) - \delta_{ij} p \tag{34}$$

In order to include the effect of a viscosity of compression that resists changes in the volume of the fluid, an extra term to the diagonal elements is added. This term is proportional to the divergence of the velocity field by a constant λ.

$$\tau_{ii} = \sigma_i = -p + 2\mu \frac{\partial u_i}{\partial x_i} + \lambda \boldsymbol{\nabla} \cdot \boldsymbol{v} \tag{35}$$

where λ is the second viscosity coefficient also in $[Pa \cdot s]$. Combining equation (35) with the Naver-Stokes equation in conservation form (33) the stresses in each direction may be written

$$\sigma_{xx} = \sigma_x = -p + \lambda \boldsymbol{\nabla} \cdot \boldsymbol{v} + 2\mu \frac{\partial u}{\partial x} \tag{36}$$

$$\sigma_{yy} = \sigma_y = -p + \lambda \boldsymbol{\nabla} \cdot \boldsymbol{v} + 2\mu \frac{\partial v}{\partial y} \tag{37}$$

$$\sigma_{zz} = \sigma_z = -p + \lambda \boldsymbol{\nabla} \cdot \boldsymbol{v} + 2\mu \frac{\partial w}{\partial z} \tag{38}$$

$$\sigma_{xy} = \sigma_{yx} = \mu \left(\frac{\partial v}{\partial x} + \frac{\partial u}{\partial y} \right) \tag{39}$$

$$\sigma_{xz} = \sigma_{zx} = \mu \left(\frac{\partial u}{\partial z} + \frac{\partial w}{\partial x} \right) \tag{40}$$

$$\sigma_{yz} = \sigma_{zy} = \mu \left(\frac{\partial w}{\partial y} + \frac{\partial v}{\partial z} \right) \tag{41}$$

Stokes made the hypothesis that the relationship between the molecular and the second viscosity coefficient is $\lambda = -\frac{2}{3}\mu$ [2]. With the assumption of Newtonian fluid, the stress tensor can after some matrix calculation be written as

$$\begin{aligned}\boldsymbol{\sigma} &= -p\mathbf{I} \\ &+ \begin{pmatrix} -\frac{2}{3}\mu\boldsymbol{\nabla}\cdot\boldsymbol{v} + 2\mu\frac{\partial u}{\partial x} & \mu\left(\frac{\partial v}{\partial x} + \frac{\partial u}{\partial y}\right) & \mu\left(\frac{\partial u}{\partial z} + \frac{\partial w}{\partial x}\right) \\ \mu\left(\frac{\partial v}{\partial x} + \frac{\partial u}{\partial y}\right) & -\frac{2}{3}\mu\boldsymbol{\nabla}\cdot\boldsymbol{v} + 2\mu\frac{\partial v}{\partial y} & \mu\left(\frac{\partial w}{\partial y} + \frac{\partial v}{\partial z}\right) \\ \mu\left(\frac{\partial u}{\partial z} + \frac{\partial w}{\partial x}\right) & \mu\left(\frac{\partial w}{\partial y} + \frac{\partial v}{\partial z}\right) & -\frac{2}{3}\mu\boldsymbol{\nabla}\cdot\boldsymbol{v} + 2\mu\frac{\partial w}{\partial z} \end{pmatrix} \\ &= -p\mathbf{I} + 2\mu\dot{\boldsymbol{\epsilon}} \end{aligned} \tag{42}$$

where $\dot{\boldsymbol{\epsilon}}$ is the strain rate tensor $\dot{\epsilon}_{ij} = \left(\frac{\partial u_i}{\partial x_i} + \frac{\partial u_j}{\partial x_j}\right)$, with dimension $[\frac{1}{s}]$.

5.5 CONSERVATION OF ENERGY

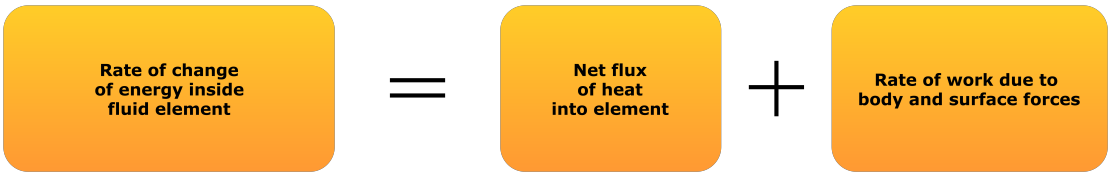

Figure 23: First law of thermodynamics [2].

The physical principle stated in this section is merely the first law of thermodynamics.

5.5.1 *Rate of change of energy inside fluid element*

The fluid element has two contributions to its total energy E given in $\left[\frac{J}{Kg}\right] = \left[\frac{m^2}{s^2}\right]$

- The internal energy due to random molecular motion, e in $\left[\frac{J}{Kg}\right]$
- The kinetic energy due to translational motion, $\frac{v^2}{2}$ in $\left[\frac{J}{Kg}\right]$

The time rate of change is given by the operator $\left[\frac{D}{Dt}\right]$ and the mass of the element is $\rho\ dzdydz$ [2]. Thus the time rate of change of energy inside the element (abbreviated A) is given by

$$A = \rho\frac{D}{Dt}\left(e + \frac{v^2}{2}\right) dxdydz. \tag{43}$$

5.5.2 *Net flux of heat into element*

The topic of heat flux is extensive. Generally heat flux happens due to volumetric heating such as absorption or emission of radiation, thermal conduction and convection [2]. Considering the element at hand, heat flux into the element happens largely due to thermal conduction (abbreviated H) or heat transfer across the surface due to temperature gradients. The volumetric heat effect, $\rho\dot{q}\ dxdydz$ is therefore neglected.

$$\begin{aligned} H &= -\left(\frac{\partial \dot{q}_x}{\partial x} + \frac{\partial \dot{q}_y}{\partial y} + \frac{\partial \dot{q}_z}{\partial z}\right) \\ &= -\nabla \cdot \dot{\mathbf{q}}\ dxdydz \end{aligned} \tag{44}$$

where $\dot{\mathbf{q}} = \begin{pmatrix} \dot{q}_x & \dot{q}_y & \dot{q}_z \end{pmatrix}^T$ is the heat flux.

5.5.3 *Rate of work due to body and surface forces*

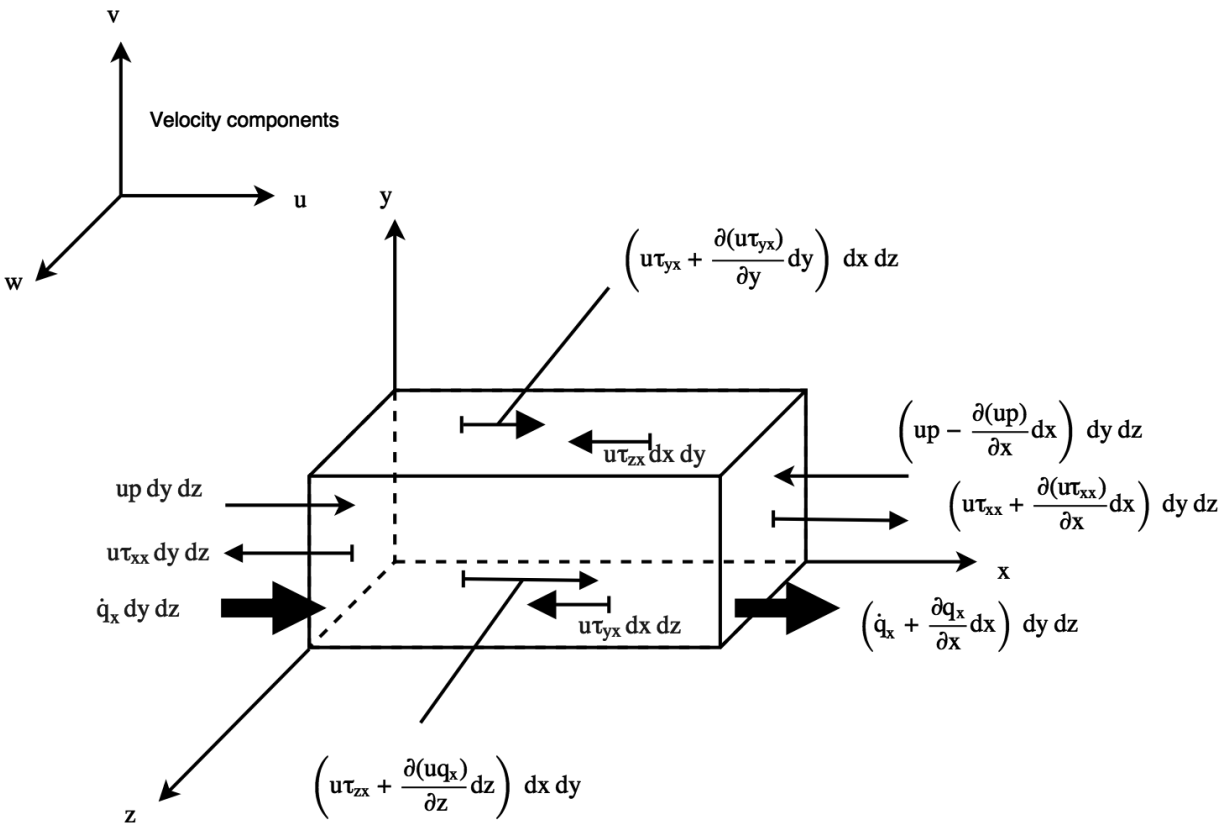

Figure 24: Energy fluxes in x direction [2].

To evaluate the rate of work due to forces, stating the difference between work done by body and surface forces is necessary [2]. For body forces acting on the fluid element moving at a velocity $\boldsymbol{v}$, the rate of work done is

$$W = \rho \mathbf{f} \cdot \boldsymbol{v} dx dy dz \tag{45}$$

With the help of [Figure 24], the deduction of rate of work (abbreviated RWS) done by surface forces can be obtained.

$$\begin{aligned}
\text{RWS} = & \left[\underbrace{-\frac{\partial(up)}{\partial x} + \frac{\partial(u\tau_{xx})}{\partial x} + \frac{\partial(u\tau_{yx})}{\partial y} + \frac{\partial(u\tau_{zx})}{\partial z}}_{\text{x direction}} \right] dx dy dz \\
& + \left[\underbrace{-\frac{\partial(vp)}{\partial y} + \frac{\partial(v\tau_{xy})}{\partial x} + \frac{\partial(v\tau_{yy})}{\partial y} + \frac{\partial(v\tau_{zy})}{\partial z}}_{\text{y direction}} \right] dx dy dz \\
& + \left[\underbrace{-\frac{\partial(wp)}{\partial z} + \frac{\partial(w\tau_{xz})}{\partial x} + \frac{\partial(w\tau_{yz})}{\partial y} + \frac{\partial(w\tau_{zz})}{\partial z}]}_{\text{z direction}} \right] dx dy dz \\
& = \left[-\boldsymbol{\nabla} \cdot p\boldsymbol{v} + \boldsymbol{\nabla} \cdot u \begin{pmatrix} \tau_{xx} \\ \tau_{yx} \\ \tau_{zx} \end{pmatrix} + \boldsymbol{\nabla} \cdot v \begin{pmatrix} \tau_{xy} \\ \tau_{yy} \\ \tau_{zy} \end{pmatrix} + \boldsymbol{\nabla} \cdot v \begin{pmatrix} \tau_{xz} \\ \tau_{yz} \\ \tau_{zz} \end{pmatrix} \right] dx dy dz \\
& = [-\boldsymbol{\nabla} \cdot p\boldsymbol{v} + \boldsymbol{\nabla} \cdot (\boldsymbol{v} \cdot \boldsymbol{\tau})] \, dx dy dz \\
& = \boldsymbol{\nabla} \cdot \boldsymbol{\sigma v} \; dx dy dz
\end{aligned} \tag{46}$$

5.5.4 *The energy equation*

With (45) and (43) the rate of change of energy inside fluid element becomes

$$\begin{aligned}
\rho \frac{D}{Dt} \left(e + \frac{v^2}{2} \right) dx dy dz &= [-\boldsymbol{\nabla} \cdot \dot{\mathbf{q}} + \rho \mathbf{f} \cdot \boldsymbol{v} - \boldsymbol{\nabla} \cdot \boldsymbol{\sigma v}] \, dx dy dz \\
\rho \frac{D}{Dt} \left(e + \frac{v^2}{2} \right) &= \rho \mathbf{f} \cdot \boldsymbol{v} + \boldsymbol{\nabla} \cdot (\boldsymbol{\sigma v} - \dot{\mathbf{q}}).
\end{aligned} \tag{47}$$

This is the non-conservative form. Again, writing out the material derivative gives the conservation form

$$\rho \frac{D}{Dt}\left[\left(e+\frac{v^2}{2}\right)+\boldsymbol{v}\cdot\boldsymbol{\nabla}\left(e+\frac{v^2}{2}\right)\right]=\rho\mathbf{f}\cdot\boldsymbol{v}+\boldsymbol{\nabla}\cdot(\boldsymbol{\sigma}\boldsymbol{v}-\dot{\mathbf{q}}). \tag{48}$$

5.6 DYNAMIC STATE RELATIONS

To fully determine the fluid behaviour there is still two relation needed. Choosing ρ and e as independent variables the state relation gives

$$\begin{aligned} p &= p(e,\rho) \\ T &= T(e,\rho) \end{aligned} \tag{49}$$

For incompressible fluid this gives

$$\begin{aligned} \rho &= \text{constant} \\ c_v &= \frac{R}{\gamma-1} \\ e &= c_p T = c_V T = \frac{RT}{\gamma-1} \end{aligned}$$

And for perfect gas and constant specific heat,

$$\begin{aligned} p &= \rho R T \\ e &= c_V T = \frac{1}{\gamma-1}\frac{p}{\rho} \end{aligned}$$

Here n is the quantity of material in $[\mathrm{mol}]$, R the specific gas constant in $\left[\frac{J}{mol\cdot K}\right]$. c_p and c_V is the specific heat in $\left[\frac{J}{Kg\cdot K}\right]$ for a constant pressure and a constant volume, respectively.

5.7 NAVIER-STOKES EQUATIONS

In non-conservative partial differential form the system determining the fluid behavior is, namely (31), (32) and (47).

$$\begin{aligned} \frac{D\rho}{Dt}+\rho\boldsymbol{\nabla}\cdot\boldsymbol{v}&=0. \\ \rho\frac{D\boldsymbol{v}}{Dt}-\rho\mathbf{f}-\boldsymbol{\nabla}\cdot\boldsymbol{\sigma}&=0 \\ \rho\frac{D}{Dt}\left(e+\frac{v^2}{2}\right)-\rho\mathbf{f}\cdot\boldsymbol{v}-\boldsymbol{\nabla}\cdot(\boldsymbol{\sigma}\boldsymbol{v}-\dot{\mathbf{q}})&=0 \end{aligned} \tag{50}$$

5.8 EULER EQUATIONS

When the inertia forces due to convective contribution is much larger then the viscous forces i.e there is flow with a higher Reynolds number the viscosity can be neglected and the Navier-Stokes equations becomes the Euler equations. In this case the flow is characterized as inviscid, which is often the case in airflow.

$$\begin{aligned} \frac{D\rho}{Dt} + \rho\nabla\cdot\boldsymbol{v} &= 0. \\ \rho\frac{D\boldsymbol{v}}{Dt} - \rho\mathbf{f} + \nabla p &= 0 \\ \rho\frac{D}{Dt}\left(e + \frac{v^2}{2}\right) - \rho\mathbf{f}\cdot\boldsymbol{v} + \nabla\cdot(\dot{\mathbf{q}} + p\boldsymbol{v}) &= 0 \end{aligned} \tag{51}$$

Using the Euler equation, many fluid dynamics problems involving low viscosity and assumed invicid can easily be solved. However, the assumed negligible viscosity is no longer valid in the region of fluid near a solid boundary.

5.9 AIRFLOW

Concerning the case of airflow both in the *Flow Induced Oscillations of a Flexible Beam* benchmark producing Von Kármán vortex street and in simulating the soft palate in light of OSA, some assumptions can be made for the fluid equations. The fluid is considered to be close to that of air. It is thus considered incompressible, isotropic and Newtonian vicious with a constant viscosity μ. Furthermore, the only body force that can be present is gravitation.

5.9.1 *Incompressibility and isotropy*

For the special (but very common) case of an incompressible fluid the density ρ is assumed constant [6]. In the case of an incompressible flow, the pressure constrains the flow in such a way that the volume of fluid elements is constant. In formula incompressibility means

$$\begin{aligned} J &= \det(\mathbf{F}) = 1 \\ \rho &= \text{constant} \\ e &= cT \end{aligned} \tag{52}$$

Since the density is assumed constant equation (31) alters to

$$\nabla\cdot\boldsymbol{v} = 0 \tag{53}$$

This means that the velocity is divergence free.

5.9.2 *Newtonian viscous flow*

When the incompressibility condition is inserted into the shear stress relations described in [Section 5.4.1] the term $(\boldsymbol{\nabla}\cdot\boldsymbol{\sigma}_{dev})^T$ in the momentum equation (32) simplifies to

$$(\boldsymbol{\nabla}\cdot\boldsymbol{\sigma}_{dev})^T = \mu\boldsymbol{\nabla}^2\boldsymbol{v}$$

and the momentum equation (32) simplifies to

$$\rho\frac{D\boldsymbol{v}}{Dt} = \rho\mathbf{f} - \boldsymbol{\nabla}p + \mu\boldsymbol{\nabla}^2\boldsymbol{v}. \tag{54}$$

The momentum equation and the energy equation form a system of equations which is now

$$\begin{aligned} \boldsymbol{\nabla}\cdot\boldsymbol{v} &= 0 \\ \rho\frac{D\boldsymbol{v}}{Dt} &= \rho\mathbf{f} - \boldsymbol{\nabla}p + \mu\boldsymbol{\nabla}^2\boldsymbol{v} \\ \rho\frac{D}{Dt}\left(e + \frac{v^2}{2}\right) &= \rho\mathbf{f}\cdot\boldsymbol{v} + \boldsymbol{\nabla}\cdot(\boldsymbol{\sigma}\boldsymbol{v} - \dot{\mathbf{q}}) \end{aligned} \tag{55}$$

5.9.3 *Initial and boundary conditions*

$$\begin{aligned} \boldsymbol{\nabla}\cdot\boldsymbol{v} &= 0 \\ \rho\frac{D\boldsymbol{v}}{Dt} &= \rho\mathbf{f} - \boldsymbol{\nabla}p + \mu\boldsymbol{\nabla}^2\boldsymbol{v}. \end{aligned} \tag{56}$$

The system (56) needs one BC at the entire boundary for $\boldsymbol{v}$ and one IC, also for $\boldsymbol{v}$. Initially the the solid has zero velocity, thus by the no-slip conditions the same applies to the fluid at this boundary [2].

5.9.4 *Nondimensional equations*

For fluid dynamics, characteristic parameters can be selected to nondimensionalize the equations [6]. Nondimensionalized equation helps to gain a greater insight into the relative size of various terms present in the equation. The Navier-Stokes equations when incompressible case is assumed can be nondimensionalised using the parameters in [Table 1].

Variable	L	U	$\frac{L}{U}$	$\frac{1}{L}$
Parameter	$x' = \frac{x}{L}$	$v' = \frac{v}{U}$	$t' = \frac{t}{\frac{L}{U}}$	$\nabla' = \frac{\nabla}{\frac{1}{L}}$
...	$\frac{U^2}{L}$	ρ_0	$\rho_0 U^2$	
...	$f' = \frac{f}{\frac{U^2}{L}}$	$\rho' = \frac{\rho}{\rho_0}$	$p' = \frac{p}{\rho_0 U^2}$	

Table 1: Characteristic parameters.

Here L, U and ρ_0 is the characteristic length, velocity and density. Incompressibility is assumed such that the fluid density is constant. When the parameters are applied to (55) it yields

$$\nabla' \cdot v' = 0 \tag{57}$$

$$\frac{Dv'}{Dt'} = f' - \nabla' p' + \frac{1}{Re}(\nabla')^2 v. \tag{58}$$

where Re is the Reynolds number. The Reynolds number is the most important dimensionless number in fluid dynamics and is used to provide a criterion for determining dynamic resemblance. It represents the ratio between inertial force and vicious force. The Reynolds number is used to describe the flow as laminar or turbulent. In flows where vicious forces are dominant and the Reynolds number is low laminar flow occurs. Laminar flow is when the flow is occurring smoothly or in regular paths. This is in contrast to turbulent flow, where the flow is dominated by inertial forces and high Reynolds number occur.

$$\begin{aligned} Re &= \frac{\text{dynamic pressure}}{\text{shear stress}} = \frac{\frac{\rho_0 U^2}{L}}{\frac{\mu U}{L^2}} \\ &= \frac{\text{inertia forces}}{\text{vicious forces}} = \frac{\rho_0 U}{\frac{\mu}{L}} \\ &= \frac{\rho_0 U L}{\mu} \end{aligned}$$

For the *Flow Induced Oscillations of a Flexible Beam* benchmark the standard parameters are as follows

- inflow velocity $u_\infty = U = 51.3 \left[\frac{cm}{s}\right]$
- dynamic viscosity $\mu_f = \mu = 1.82 \cdot 10^{-4} \left[\frac{g}{cm \cdot s}\right]$
- density $\rho_f = \rho_0 = 1.18 \cdot 10^{-3} \left[\frac{g}{cm^3}\right]$

This corresponds to Reynolds number

$$Re = \frac{\rho_0 L U}{\mu} = \frac{1.18 \cdot 10^{-3} \left[\frac{g}{cm^3}\right] \cdot 1.0 \cdot 51.3 \left[\frac{cm}{s}\right]}{1.82 \cdot 10^{-4} \left[\frac{g}{cm \cdot s}\right]} = 332.6.$$

Which typical is in the low laminar flow regime. Low Reynolds Numbers can produce vibrations to small structures due to vortex shedding downstream of the structural body encountered.

5.10 VORTEX INDUCED VIBRATIONS

Vortex Induced Vibration (VIV) manifests itself in several applications where flexible structures are subject to external forces. The phenomena is also present in smaller scale systems such as the *Flow Induced Oscillations of a Flexible Beam* benchmark. In short VIV happens due to fluid flow interacting with a structure generating periodic motion to the system [47].

5.10.1 *Vortex shedding*

When subjected to flow at certain conditions, a structure may produce the phenomena called vortex shedding. When structures are emerged by an unsteady oscillating flow vortices are created behind the structure and detach periodically from either sides. This results in a so called *von Kármán vortex street*. Periodic shedding creates low pressure vorticies downstream, resulting in lift and drag forces acting on the structure.

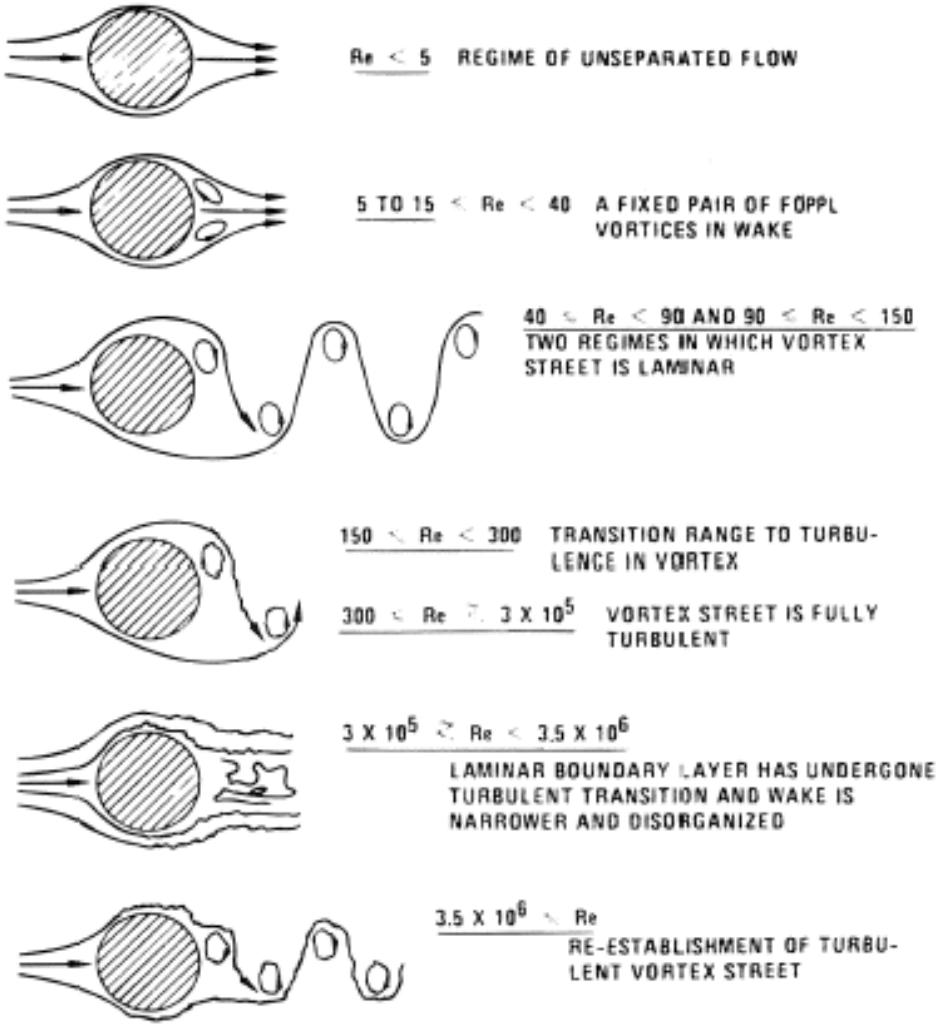

Figure 25: Vortex shedding patterns for different Reynolds number. Cylindrical object [8].

5.11 LIFT AND DRAG

The Forces acting on the structure are the lift and drag forces. The aerodynamic forces on a body comes primarily from differences in pressure and viscous shearing stresses. The drag force is given by

$$F_D = C_D \frac{1}{2} \rho_f u^2 A_{ref} \tag{59}$$

,

where ρ_f is the fluid density, u the velocity and A_{ref} the projected reference area [6]. The drag and lift force are dependent on the drag coefficient C_D and lift coefficient C_L, respectively. The lift force is determined by the equation

$$F_L = C_L \frac{1}{2} \rho_f U^2 A_{ref}$$

However, when the pressure distribution on the surface is known, determining the total lift requires adding up the contributions to the pressure force from local elements of the surface, each with its own local value of pressure. The total lift is thus the integral of the pressure, in the direction perpendicular to the far-field flow, over the entire surface. This can be state as

$$F_L = \oint p \mathbf{n} \cdot \mathbf{k} dS.$$

6

COMPUTATIONAL FLUID-STRUCTURE INTERACTION

"Fluid–structure interaction (FSI) is a class of problems with mutual dependence between the fluid and structural mechanics parts. The flow behavior depends on the shape of the structure and its motion, and the motion and deformation of the structure depend on the fluid mechanics forces acting on the structure." - Bazilevs et al., 2013 [6]

A typical FSI problem is a scenario where a moving and deformable structure is emerged and surrounded in fluid flow. The physical quantities of the structure and flow will then interact with each other. Each domain has its own fields or physical quantities which influence the other [6].

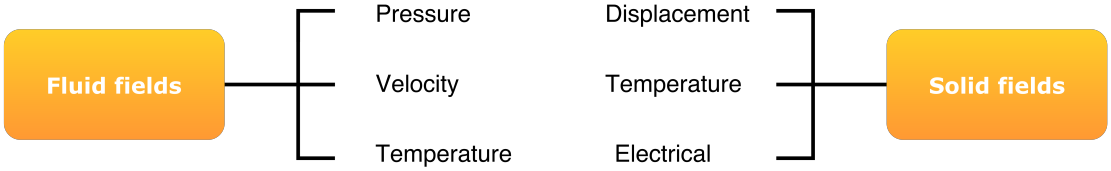

Figure 26: Representative fields of fluid-structure domains [43].

Fluid-structure interaction requires the discretisation of both the structure and fluid. Each of these must then be solved. Depending on the coupling the system may be solved in turns or simultaneously.

6.1 COUPLED SYSTEMS

A system is defined as coupled if two or more physical systems interact with each other, and the solution of either one is dependent on the other. Neither the fluid nor the structural system can be solved independently, due to the unknown forces in the interface region. This is perhaps best described by the wordings of Zienkiewicz, Taylor, and Zhu [48]

"Coupled systems and formulations are those applicable to multiple domains and dependent variables which usually (but not always) describe different physical phenomena and in which;

- *neither domain can be solved while separated from the other*
- *neither set of dependent variables can be explicitly eliminated at the differential equation level."*

The coupled domains do not overlap, which require a set of physical meaningful interface conditions [6]. The coupling conditions are the compatibility of the kinematics and traction at the fluid-structure interface. Since the structure domain is on motion and in most cases the motion follows the material particles, it follows the Lagrangian description of the structural motion. Thus the shape of the fluid sub-domain must change in order to accommodate the motion of the structure.

FSI is generally divided into two, the one-way and two-way FSI. One-way FSI provides an economic alternative since only the structure is subject to the fluid behaviour, and not the other way [21]. One-way FSI has what is called a weak coupling between a fluid and a structure. When the structural motions and deformations are small and will not influence the fluid motion to a large extent, the one-way FSI might be a valid choice. When both systems are subject to the others behaviour, it is a Two-way FSI. Physical properties like deformation, pressure, shear stress are continuously transferred between the two domains. Two-way FSI should be used when the interaction between the fluid and the structure is significant. For applications exposed to VIV, Two-way coupling is the best approach [6].

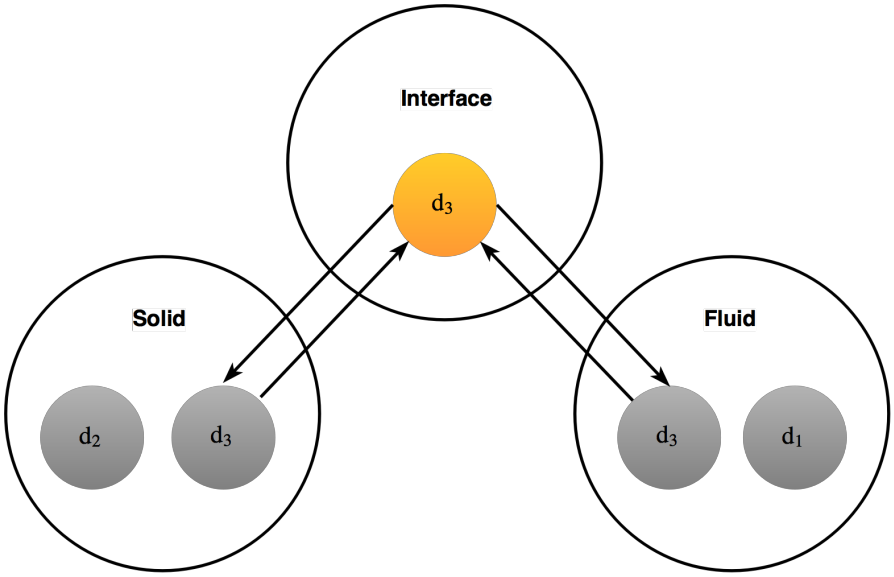

Figure 27: Typical FSI solver setup [46].

By introducing the interface, a third domain in addition to the fluid and structure domains, a system of transfer can be developed. The interface domain makes it possible to handle date of non-matching meshes and allows for independent re-meshing of sub-domains. Such an approach, suggested in [Figure 27], enables the transfer of data such as traction forces and kinematic data.

The choice of discretization for the fluid and structure may be challenging in the process of coupling [48]. In case of using a non-conforming mesh [Sec-

tion 3.5], separate fluid and solid discretizations a non-matching mesh will occur at the intersection. It is then essential to ensure that the fluid and structure have correct coupling of their kinematics and traction.

A standard computational domain denoted by Ω is represented in the figure [Figure 28] [6]. Note that the subscripts "I" refer to the interface, "E" to external and "t" to the time configuration. As shown the domain has an internal boundary Γ_1 and an external boundary Γ_2. The Ω_1 and Ω_2 represent the fluid domain and structural domain, respectively. Thus the whole domain $\Omega = \Omega_1 \cup \Omega_2$ and at the non-overlapping interface $\Gamma_1 = \Omega_1 \cap \Omega_2 = 0$.

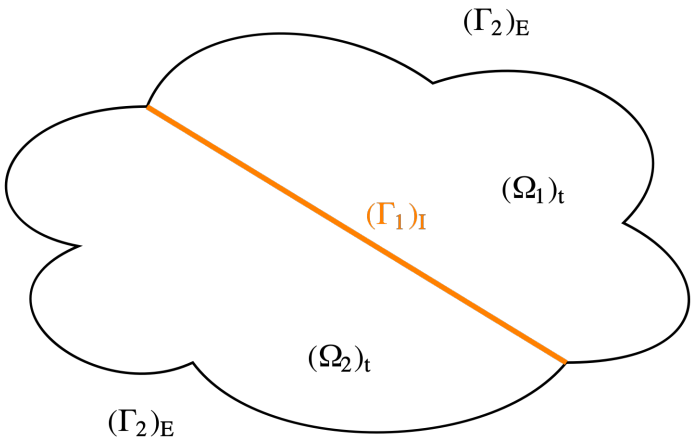

Figure 28: Schematics of fluid and solid spatial domains in a FSI problem [6].

When basing on [Figure 28], FSI formulation at the continuous level can be stated as

$$\begin{aligned}
&\int_{(\Omega_1)_t} w_1 \cdot \left(\rho \left(\frac{\partial \mathbf{v}}{\partial t} + \mathbf{v} \cdot \nabla \mathbf{v} - \mathbf{f} \right) - \nabla \cdot \boldsymbol{\sigma}_1 \right) d\Omega \\
&\qquad + \int_{\Gamma_1} w_1 \cdot (\boldsymbol{\sigma}_1 \mathbf{n}_1 - \mathbf{h}_1) d\Gamma \\
&\qquad + \int_{(\Omega_1)_t} q_1 \nabla \cdot \mathbf{v} d\Omega \\
&+ \int_{(\Omega_2)_t} w_2 \cdot \left(\rho \left(\frac{d^2 \mathbf{y}}{dt^2} - \mathbf{f} \right) - \nabla \cdot \boldsymbol{\sigma}_2 \right) d\Omega \\
&\qquad + \int_{\Gamma_1} w_2 \cdot (\boldsymbol{\sigma}_2 \mathbf{n}_2 - \mathbf{h}_2) d\Gamma \\
&+ \int_{\Gamma_1} (w_1 \cdot \boldsymbol{\sigma}_1 \mathbf{n}_1 + w_2 \cdot \boldsymbol{\sigma}_1 \mathbf{n}_1) d\Gamma = 0
\end{aligned} \tag{60}$$

where $\mathbf{h}_1$ and $\mathbf{h}_2$ are the corresponding prescribed traction vectors. From [Chapter 4] and [Chapter 5] the individual equations for the fluid and structure sub-domains was derived, namely

$$\rho\frac{D\boldsymbol{v}}{Dt} = \rho\mathbf{f} - \boldsymbol{\nabla}p + \boldsymbol{\nabla}\cdot\boldsymbol{\sigma}_1 \quad \text{in } (\Omega_1)_t, \tag{61}$$

$$\boldsymbol{\nabla}\cdot\boldsymbol{v} = 0 \quad \text{in } (\Omega_1)_t \tag{62}$$

and

$$\rho\frac{D\boldsymbol{u}}{Dt} = \boldsymbol{\nabla}\cdot\boldsymbol{\sigma}_2 + \rho\mathbf{f} \quad \text{in } (\Omega_2)_t \tag{63}$$

Here $\boldsymbol{\sigma}_1$ and $\boldsymbol{\sigma}_2$ are the Cauchy stress tensors for the fluid and the solid, respectively. When the traction boundary conditions are satisfied

$$\boldsymbol{\sigma}_1\mathbf{n}_1 - \mathbf{h}_1 = 0 \quad \text{on } (\Gamma_{1h})_t \tag{64}$$

and

$$\boldsymbol{\sigma}_2\mathbf{n}_2 - \mathbf{h}_2 = 0 \quad \text{on } (\Gamma_{2h})_t \tag{65}$$

When introducing $w_1 = w_2$ on Γ_1 to the remaining terms

$$\int_{\Gamma_1} (w_1\cdot\boldsymbol{\sigma}_1\mathbf{n}_1 + w_2\cdot\boldsymbol{\sigma}_1\mathbf{n}_1)\,d\Gamma = 0 \tag{66}$$

The concluding equation is presented as

$$\boldsymbol{\sigma}_1\cdot\mathbf{n}_1 - \boldsymbol{\sigma}_2\cdot\mathbf{n}_2 = 0, \tag{67}$$

on Γ_1 with $\mathbf{n}$ being the outer normal at the boundary [6]. This is the dynamic constraint giving equivalence of the Cauchy stress tensors in the two domains [27].

In order to couple the two domains a kinematic restraint or no slip condition is applied on the boundary of the solid [26]

$$\mathbf{u}_2 - \mathbf{u}_1 = 0 \;\Rightarrow\; \mathbf{u}_1 = \frac{\partial\mathbf{d}_2}{\partial t}, \tag{68}$$

where $\mathbf{u}_1$ is the fluid velocity and $\mathbf{d}_2$ is the displacement vector of the structure.

Different schemes can be used to obtain a coupled solution. Besides the Newton-Raphson and Gauss-Seidel schemes, a staggered scheme is also applicable. These three types are briefly described in following sections. However,

the staggered scheme is of most importance since it is the focus scheme of the thesis's methodology.

Different methods are available for solving FSI problems. The two methods commonly divided into are the monolithic approach and the partitioned approach.

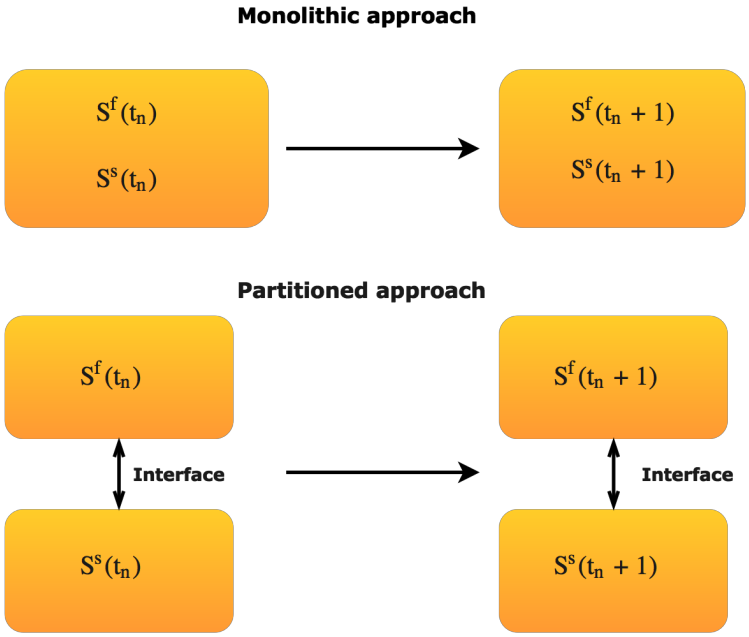

Figure 29: Schematics of monolithic and partitioned approaches [17].

6.2 MONOLITHIC APPROACH

A monolithic or direct approach, as represented in [Figure 29], aims to solve both the structural and the fluid equations simultaneously in one single matrix system [6]. The DOF from all the sub-systems (fluid, solid, interface and mesh) are accumulated into single matrix equation, which is highly non-linear and involves all cross-derivatives.

$$\begin{pmatrix} K_s & K_{fs} \\ K_{sf} & K_f \end{pmatrix} \begin{pmatrix} u_s \\ u_f \end{pmatrix} = \begin{pmatrix} F_s \\ F_f \end{pmatrix}$$

The interface conditions are implicit in the solution procedure. As such it makes the monolithic approach considered more robust than the partitioned. This approach can potentially achieve better accuracy for a multi-disciplinary problem [17]. However, the matrix system tends to be very large for large models and the computational time increases a lot since the methods requires a lot of memory. The monolithic approach requires a code developed for this

particular combination of physical problems. Therefore virtually excluding the possibility of using quite capable existing fluid and structural solvers.

Monolithic solvers are often regarded impractical. The physical models has to be implemented within a single solution environment, which is difficult and sometimes less effective. To be able to keep up with the latest developments of research the solver also has to be continuously modified.

An example of commercial software that implements the monolithic approach is ADINA [22]. ADINA is using finite elements (FEM) to discretize both the structure and the fluid, whereas in computational fluid dynamics (CFD) the traditional discretization approach is to use finite volumes (FVM). Monolithic solvers such as the one utilized by COMSOL appear to be unconditionally stable (possible to use larger time steps) as compared to a partitioned scheme.

6.3 PARTITIONED APPROACH

By the partitioned FSI approach (represented in [Figure 29]), fluid and structure are solved separately within two distinct solvers [6]. Each solver uses its respective mesh discretization and numerical algorithm. Hence, the partitioned approach has the benefit of reserving software modularity, because a existing flow solver and structural solver are coupled. These solvers are usually focused within their own physical domains. Therefore the partitioned approach has the advantage of flexibility by being able to combine different solvers with different numerical methods. This can become convenient when solving advanced FSI problems as the interface geometry become complicated.

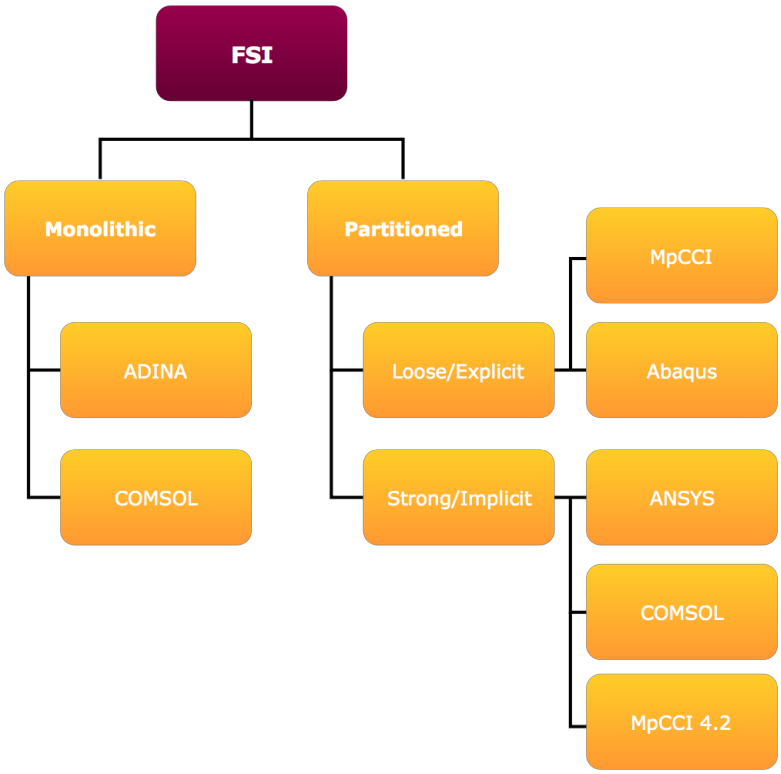

Figure 30: Examples of software.

A coupling algorithm is needed to couple the solvers at the interface in both space and time. The partitioned approach can be categorized into two different kinds of coupling algorithms; loosely coupled and strongly coupled. It is important to notice that the method for solving each subsystem has nothing to with the method of coupling. For instance, an explicit coupling can be used when implicit solvers are used for both fluid and structure.

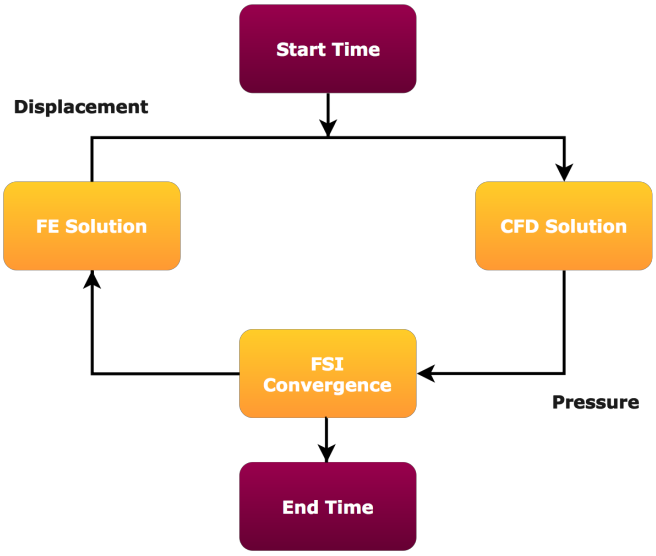

Figure 31: Schematics of convergence process [3].

The partitioned method usually follows a convergence process like the one given in [Figure 31]. More detailed description is given by *Michler et al., 2004* [32]

1. Transfer the motion of the structural boundary to the fluid
2. Update the position of the moving fluid mesh
3. Advance the fluid system in time and compute the new pressure
4. Convert the new fluid pressure into a structural load
5. Advance the structural system in time under the fluid-induced load

The general goal is to obtain a coupled solution within the desired accuracy. As such the coupling algorithm usually contains an iteration scheme and a interpolation method. This is to transfer data between the systems. This depends on how the problem is coupled. The coupling can be either loosely coupled or strongly partition coupled.

6.3.1 *Loose coupling*

Loosely coupling is most often referred to as a staggered scheme. The method is perhaps best introduced by *Bazilevs et al., 2013* [6]

"For a given time step, a typical loosely-coupled algorithm involves the solution of the fluid mechanics equations with the velocity boundary conditions coming from the extrapolated structure displacement rate at the interface, followed by the solution of the structural mechanics equations with the updated fluid mechanics interface traction, and followed by the solution of the mesh moving equations with the updated structural displacement at the interface."

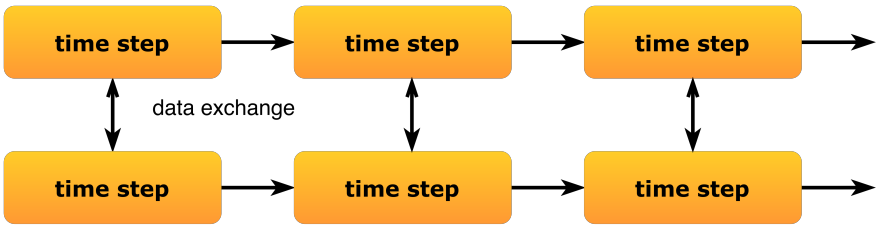

Figure 32: Loose/implicit coupling [38].

In loosely coupled approaches, the equations of fluid mechanics, structural mechanics, and movement of meshes are solved sequentially. A loosely coupled algorithm is explicit and the codes will have only one bidirectional exchange of solved variables per time step, in a sequentially staggered manner

[6]. The loosely coupled scheme is thus considered favorably in terms of efficiency. The most usual algorithm for loosely coupled system is to solve the system in a sequentially staggered manner, but the Gauss-Seidel method, the Newton-Raphson method and the Jacobi method are applicable.

The iterative staggered partitioned scheme is energy conservative at the interface. This makes it more stable than the explicit/strong coupling. This however, often makes it more time consuming. On the other hand the loosely coupled schemes also has some drawbacks. When applied the added mass effect discussed later in [Section 7.5.2] can make the scheme unstable.

As seen in [Figure 30], Abaqus' FSI solver is partitioned and uses a loose partition coupling algorithm. Thus the fluid and structure equations are solved subsequently.

6.3.2 *Strong coupling*

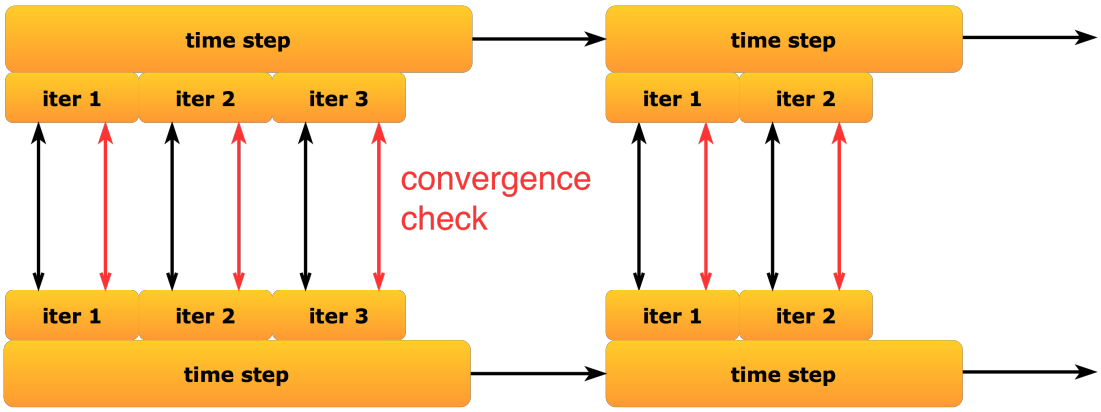

Figure 33: Strong/explicit coupling [38].

Strongly coupled solvers completely satisfy the equilibrium of traction forces. In addition to Gauss-Seidel they consist of monolithic and partitioned Newton-Raphson schemes. Strongly coupled systems utilize an iteration method to obtain convergence before further time-stepping. Within each time-step, data is transferred between the fluid and structural solver until the solution converges. This is shown in [Figure 33]. For the sake of accuracy, the structure influences the fluid and the other way around in such a strong way, that more than one iterations per time step are needed before advancing to the next time step. Three categories of coupling techniques can be used in the monolithic and strongly coupled approach: the block-iterative, quasi-direct, and the direct coupling [6].

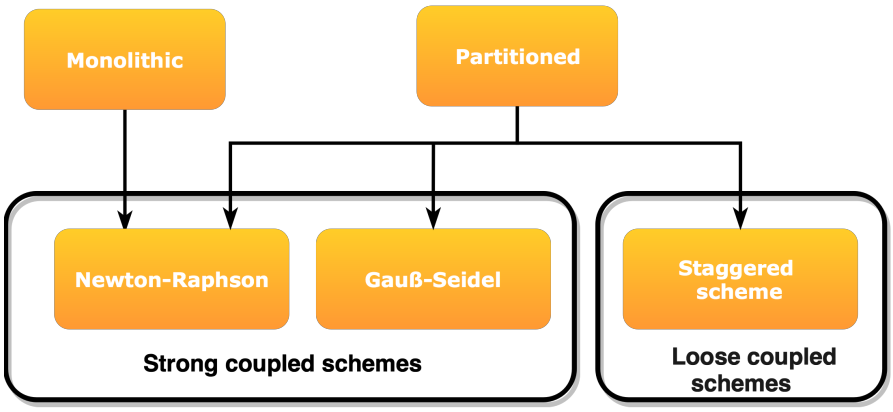

Figure 34: Possible interface tracking strategy [46].

The Newton-Raphson schemes can be solved as a whole or sequential, monolithic and partitioned respectively. A system of equations that corresponds to this scheme is

$$\begin{aligned}\mathbf{N}_1(\mathbf{d}_1, \mathbf{d}_2, \mathbf{d}_3) &= 0\\ \mathbf{N}_2(\mathbf{d}_1, \mathbf{d}_2, \mathbf{d}_3) &= 0\\ \mathbf{N}_3(\mathbf{d}_1, \mathbf{d}_2, \mathbf{d}_3) &= 0\end{aligned}$$

where $\mathbf{d}_1$, $\mathbf{d}_2$ and $\mathbf{d}_3$ are vectors of nodal unknowns. These corresponds to the unknown functions $\mathbf{u}_1$, $\mathbf{u}_2$ and $\mathbf{u}_3$.

To solve these equations with Newton-Raphson it is necessary to get a solution of the linear equation system [6]

$$\begin{aligned}\mathbf{A}_{11}\mathbf{x}_1 + \mathbf{A}_{12}\mathbf{x}_2 + \mathbf{A}_{13}\mathbf{x}_3 &= \mathbf{b}_1\\ \mathbf{A}_{21}\mathbf{x}_1 + \mathbf{A}_{22}\mathbf{x}_2 + \mathbf{A}_{23}\mathbf{x}_3 &= \mathbf{b}_2\\ \mathbf{A}_{31}\mathbf{x}_1 + \mathbf{A}_{32}\mathbf{x}_2 + \mathbf{A}_{33}\mathbf{x}_3 &= \mathbf{b}_3\end{aligned}$$

Here $\mathbf{x}_1$, $\mathbf{x}_2$ and $\mathbf{x}_3$ the correction increments for $\mathbf{d}_1$, $\mathbf{d}_2$ and $\mathbf{d}_3$. $\mathbf{b}_1 = -\mathbf{N}_1$, $\mathbf{b}_2 = -\mathbf{N}_2$ and $\mathbf{b}_3 = -\mathbf{N}_3$ are the residuals of the nonlinear equations and $\mathbf{A}_{\beta\gamma} = \frac{\partial \mathbf{N}_\beta}{\partial \mathbf{d}_\gamma}$.

Consistent partitioned Newton-Raphson methods tend to offer good robustness, but the implementation can be computational expensive and cumbersome. In both Gauss-Seidel and staggered schemes the sub-domains are solved sequentially. They are also solved in separate systems of equations.

6.4 INTERFACE CAPTURING AND TRACKING

In general there are two possible ways of defining the interface between the fluid and structure [Figure 35] [6].

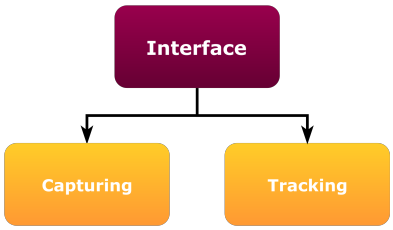

Figure 35: Interface definition.

When interface capturing is used, the solid and fluid mesh are moving independently. This is primarily used with an Eulerian fluid mesh. Although this method does not constrain the scale of deformations, in case of holding up to the conservation equations it is less accurate.

In the case of using interface tracking, the fluid and structure are moving together. No overlapping or gaps between the sub-domains occurs. This method is considered more accurate than interface capturing. However it is not sufficient when there is large deformations. Thus, re-meshing is needed. In the *Flow Induced Oscillations of a Flexible Beam* and OSA palate model case only interface tracking is used.

7

NUMERICAL APPROACH AND SOFTWARE UTILITY

7.1 INTRODUTCION

A general presentation of the different numerical approaches and methods will be given. In addition to FSI being a three-field problem, where the motion of the structure and the fluid domains may initially be unknown [6]. All the issues related to numerical discretizations of single field problems, such as stability, robustness, accuracy, speed and ability to handle complex geometries are also present in FSI problems.

The fluid and structure domains can be discretisized by different methods just like normal fluid and solid solvers can. A flexible approach is to have separate fluid and structure discretizations for the individual sub-problems. The choice of discretization schemes is important, since this is how the different terms in the equations are approximated. Such as the advective and the diffusive terms typically used in CFD. A rule of thumb is that higher order schemes gives a more accurate approximation, but are far more unstable [33]. Lower order schemes such as upwind can create numerical diffusion, but often stabilizes the simulation.

Three ways of describing the physical domains is presented here. Each method is similar in that it represents a systematic numerical method for solving partial differential equations (PDE). The major difference is the implementation.

7.2 FINITE DIFFERENCE

The finite difference method is based on the differential form of the PDE [44]. Each derivative is replaced with an approximate difference formula, usually derived from a Taylor series expansion. The domain or grid may be divided into hexahedral cells, in which the solution will be obtained at each nodal point.

$$\nabla^2 \mathbf{u} = S -> \frac{\partial^2 \mathbf{u}}{\partial x^2} = S.$$

The Taylor series expansion around a given point is given as

$$\frac{\partial^2 \mathbf{u}}{\partial x^2} \approx \frac{\mathbf{u}_{j-1} - 2\mathbf{u}_j + \mathbf{u}_{j+1}}{\Delta x^2}.$$

Often the choice is between upwind, central and downwind schemes [4]. The upwind scheme is called conditionally stable. Whereas the downwind and the central scheme are unconditionally unstable. The main disadvantage of the upwind scheme is that it introduces a large amount of numerical diffusion due to the first order truncation error. Thus smearing out the solution if not run in fine enough mesh. If the truncation error is made to approach zero, the solution to the differential equation would approach the true solution to the PDE. If however providing a solution is more important than the accuracy, the upwind scheme will easier provide convergence than a unstable scheme.

7.3 FINITE ELEMENT

One reason for the finite elements method's (FEM) success in multiphysics analysis is that it is a very general method. This is described in the book by Shröder and Wriggers [42]. In the finite element method the dependant values are stored at the element nodes. The discretization is based upon a piecewise representation of the solution in terms of specified basis functions. The computational domain is divided into smaller finite elements, where the solution is constructed from the basis functions.

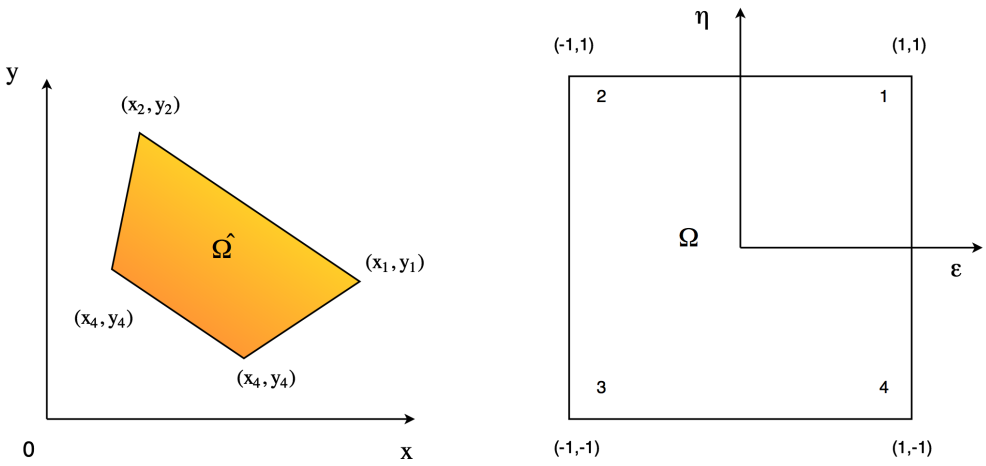

Figure 36: Finite Element Method [20].

The actual equations that are solved are typically obtained by restating the conservation equation in weak form. The field variables are written in terms of the basis functions, the equation is multiplied by appropriate test functions and then integrated over an element. Since the FEM solution is in terms of specific basis functions, a great deal more is known about the solution than for either FDM or FVM. This can be a double-edged sword, as the choice of basis functions is very important and boundary conditions may be more difficult to

formulate. Again, a system of equations is obtained (usually for nodal values) that must be solved to obtain a solution.

7.4 FINITE VOLUME

In finite volume the dependant values are stored in the center of the finite volume [33]. As opposed to FEM each cell the energy from conservation of mass and momentum is ensured in FVM. The discretization is based upon an integral form of the PDE [19]. These are the conservation of mass, momentum and energy equations which was shown in [Chapter 5]. The boundary-value problem is given as

$$\nabla^2 u = s \quad => \quad \frac{\partial^2 u}{\partial x^2} = S.$$

With FVM this statement is converted to an integral conservative form before discretization. The last term includes the surface flux effects.

$$\int_\Omega \frac{\partial^2 u}{\partial x^2} = \int_\Omega S.$$

Manipulations of the equations rely on the Gaussian divergence theorem; generally

$$\iiint_V \nabla \cdot F dV = \oint_{S(V)} F \cdot \hat{N} dS. \tag{69}$$

The PDE is written in a form which can be solved for a given cell. The domain is discretized onto cells or finite volumes, which for every volume the governing equations are solved. The resulting system of equations usually involves fluxes of the conserved variables.

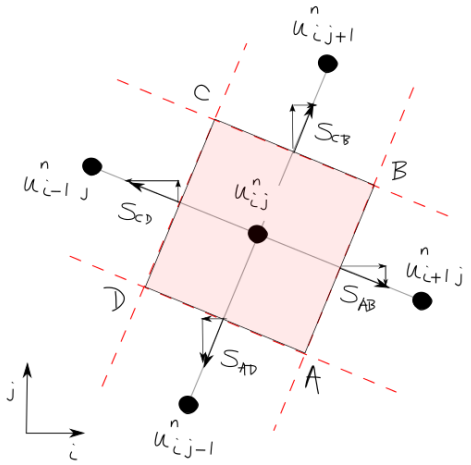

Figure 37: Fluid Volume Method [36].

The advantage this method holds over FDM is that it does not require the use of structural grids. Also the effort to convert the given mesh in to a structured numerical grid internally is avoided [19]. The approximate solution is discrete, but the variables are typically placed at cell centers rather than nodal points as in FDM and FEM. However, there also exists face-centered finite volume methods. In any case, the values of field variables at non-storage locations (e.g. vertices) are obtained using interpolation.

7.5 PARAMETERS

In this section some parameters which is of importance to the FSI simulations will be presented. First off the CFL number which is a condition named after Courant-Friederichs-Lewy is of importance when it comes to transient problems [33]. Other parameters such as the added mass matrix plays a significant role on slender structures exposed to incompressible flow where the mass ratio between the two is low.

7.5.1 *CFL number*

Usually in CFD the CFL-number gives the relationship between how time is resolved compared to the spatial resolution. A CFL number larger than one implies that a quantity are convected through one cell faster than one time step can capture as shown in the figure [Figure 38]. The CFL number show the ratio between how far the signal travels and the length of one cell. For first order schemes the equations only consider neighboring cells. If the signal travels further than the neighbour this might lead to instability. Therefore the CFL condition is usually set to be less than one in order to properly capture the transient behaviour. Violating the condition may lead to instability and the simulation might blow up.

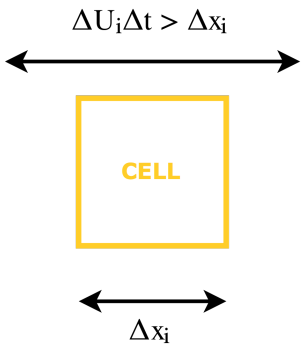

Figure 38: CFL-number

The same applies to FSI, where there also has been defined a time-interval where the computations are conditionally stable [15]. This interval results from

an upper boundary from the Courant-Friederichs-Lewy condition and a lower boundary, β, resulting from the highest eigenvalue of the added mass matrix.

$$\beta < \Delta t < CFL < 1.0.$$

A CFL number less than 1.0 is often set by default as a criteria by the solver. For instance in Abaqus CFD. This can also be adjusted and removed as a priority check before simulations.

7.5.2 *Artificial added mass*

The artificial added mass effect is an effect occurring in the loosely coupled scheme [15]. The added mass effect causes inaccuracy of traction forces such that the deformation of the structure is not done accurately. The effect happens when similar densities between fluid and solid is fully coupled. The name originates from that the fluid closest to the coupling interface will act as extra mass on the structure, increasing its inertia. The structural solver does not consider the inertia from the fluid mass which interfere with the structure. This again leads to instabilities. Using a second order staggered scheme this problem is avoided due to the scheme proving unconditionally stable even at low mass ratios.

$$\mu = \frac{\rho_s}{\rho_f} \tag{70}$$

Strong coupled algorithms are also affected by the density ratio. An increased number of iterations in each time step are needed to achieve convergence of forces along the interface. The effect occurs for instance in blood vessel FSI simulations where the density of blood and the vessel walls are similar. In the case of *Flow Induced Oscillations of a Flexible Beam* this might become a problem. However, for the case of OSA depending on the material definitions, this will not be a considerable problem [6].

7.6 POSSIBLE SOFTWARE

There exists a wide range of software for modelling fluid flow and structural analysis. Most commercial software such as Abaqus and ANSYS, are not likely to give out specific information about how the finer details. However, some solver like COMSOL often states their intentions to build an all out FEM based solver [23]. On the other hand, open source CFD software such as openFOAM is free to use and can even be modified by changing solver information. Access is given to key-files and the user may also modify source code in the built-in solvers themselves.

Abaqus, ANSYS and also COMSOL have embedded FSI solvers. ANSYS for example, may use its structural solver ANSYS Mechanical coupled with its

CFD solver ANSYS Fluent to solve a FSI problem. It is also quite possible to couple two different commercial or open source solvers, like Abaqus and openFOAM. Thus gaining some of the best aspects within two worlds of structural analysis and fluid flow.

The particular solvers use different solving techniques for FSI. In this matter the term *black box* applies. Both Abaqus and ANSYS claims to be able to solve for non-linear structural analysis and fluid flow. Figuring out the specifics of this is as mentioned not an easy task.

7.6.1 *COMSOL*

The software COMSOL uses as stated the FEM approach on both solid and fluid domains [23]. Thus it is suited for strong coupling. This however, imply that COMSOL is not a preferred choice for turbulent or transient flow. Which may be the case for OSA. In addition questions arise about the solid solvers ability to solve for nonlinear FEM.

7.6.2 *Abaqus CAE & CFD*

Most likely Abaqus uses a partitioned approach when solving FSI problems. The solvers Abaqus/CFD and Abaqus/CAE can be coupled to iterate part-solutions to convergence. The developers claim that these can provide a broad range of non-linear and coupled fluid-structural problems [45]. The solvers are said to be capable of solving laminar and turbulent flow with a deforming mesh using the ALE method discussed in [Section 3.4]. It is further claimed that FSI problems where the boundary motion is relatively independent of the fluid flow may be solved. An approach using these tools seems like a efficient and perhaps easier method for the case of OSA than combining other software for an partitioned approach.

7.6.3 *ANSYS Fluent*

The solver Fluent developed by ANSYS Inc. has a decent reputation in the computational fluid dynamics community. As stated on their web page:

ANSYS Fluent is the most powerful CFD software tool available and have well-validated physical modeling capabilities to deliver fast, accurate results across the widest range of CFD and multiphysics applications. - ANSYS Inc., 2017 [21].

ANSYS Fluent utilizes the finite volume. Therefore it often proves more stable, since unstructured meshes are easier implemented. One advantage due to its popularity is that it often supports coupling through third party coupling codes for FSI applications.

7.6.4 *Alternative software openFOAM & Abaqus CEL*

The open source CFD solver OpenFOAM is less likely qualified to solve the range of problems that other commercial solvers can solve. However, the fact that it is free to use and can be modified has its advantages. OpenFOAM has lately become popular. It is widely used by students and is continuously increasing its capability of solving a broader range of problems. For instance it has been noted that multiphase flow and transient flow can be solved using customized solvers from the software [28].

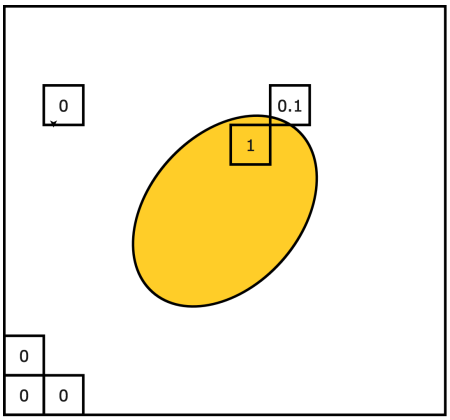

Figure 39: Volume of Fluid.

For multiphase problems OpenFOAM is capable of utilizing the volume of fluid (VOF) method introduced by Hirt and Nichols [16]. The method belongs to the class of Eulerian advective schemes, a numerical recipe to track the shape and position of the surface. For the problem of OSA multiphase do not apply. However, this method is also used by Abaqus's Coupled Eulerian-Lagrangian method (CEL), which can be used to simulate both 2D and 3D FSI problems in Abaqus CAE [45]. The exact process of which is unfortunately not a part of this report. In short, the Eulerian region is initialized by a volume fraction which represents the fluid distribution. The Volume of Fluid method is based on the idea of a fraction function α on the form:

$$\frac{\partial \alpha}{\partial t} + \mathbf{u} \cdot \nabla \alpha = 0 \tag{71}$$

The discontinuous phase boundary is replaced with a soft boundary governed by the phase fraction, α. Thus the interface is tracked indirectly through the phase fraction and not explicitly. A sufficient resolution in the boundary zones is a requirement for accurate boundary tracking. This can be done by increasing the mesh resolution which gives sharper boundary. Finer meshing often implies costly computational effort. If solution accuracy is to be achieved the Abaqus CEL method often requires a longer time to reach a solution.

7.6.5 *MpCCI*

Developed at the Fraunhofer Institute SCAI the application MpCCI is a third party coupling code designed to couple numerous supported simulation codes [37].

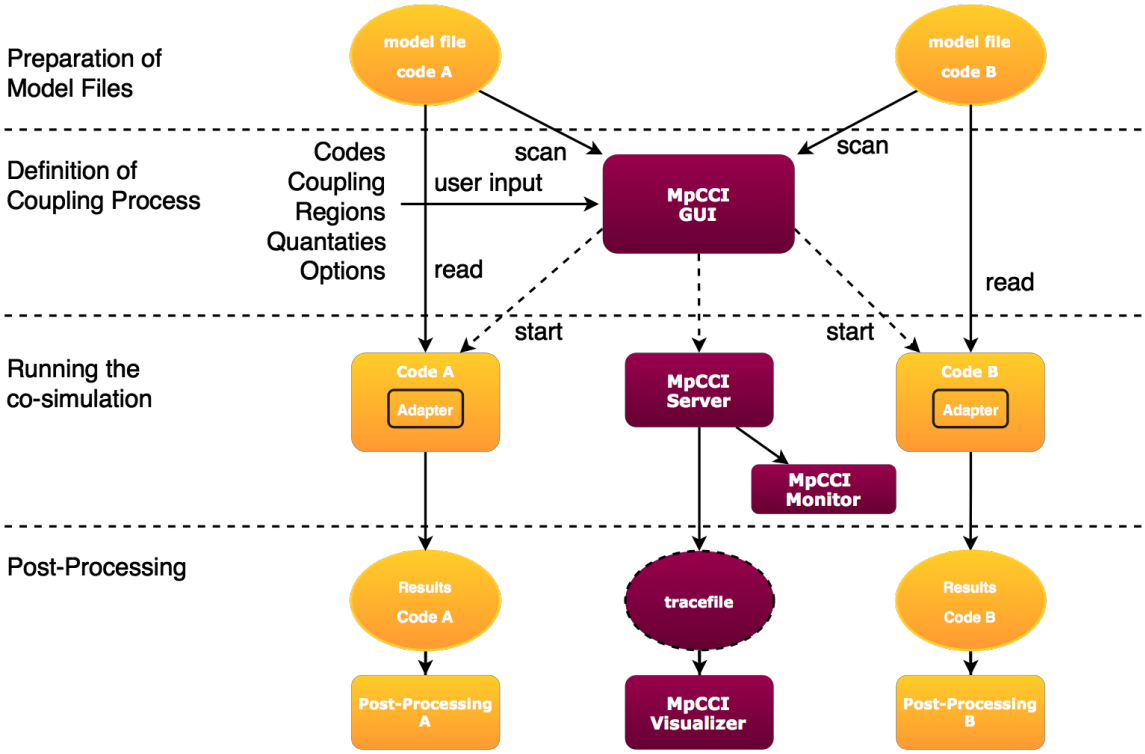

Figure 40: Using MpCCI. Overview of the simulation process [37].

The solvers to couple with MpCCI uses their own respective methods and interfaces. Thus experience with the specific solvers is an advantage. This is stated in the manual as [37]:

The application of MpCCI requires a good knowledge of the employed simulation codes. Therefore, it is recommended to use those codes for a co-simulation the user has already some experience with.

The general simulation process is show in [Figure 40]. The model files A and B used for simulation are input files from the specific solvers to couple. This can for instance be Abaqus CAE and ANSYS Fluent. The files can be created and modified through the Abaqus and Fluent interface or modified directly by changing the content of the files. Licence to the specific solvers to couple are required.

Part III

SIMULATIONS

In part III design and simulation of the benchmark *Flow Induced Oscillations of a Flexible Beam* introduced by Wall (1999) will be attempted. Comparison of the different codes used and discussion of the findings are presented to further gain advantage towards modelling the case of OSA. A perspective from a critical point of view given the different results is upheld and concluding remarks are drawn.

8

FLOW INDUCED OSCILLATIONS OF A FLEXIBLE BEAM

8.1 INTRODUCTION

In order to understand the how to and procedures of different coupling approaches the codes has to be used for simulations. The 2D FSI benchmark producing von Kármán vortex streets was chosen as the comparative study used and simulated in the different solvers. The specific solvers selected to run this benchmark is the embedded COMSOL solver, both monolithic and segregated approach, Abaqus embedded co-simulation and Abaqus CAE coupled with Ansys Fluent via the third party coupling code MpCCI.

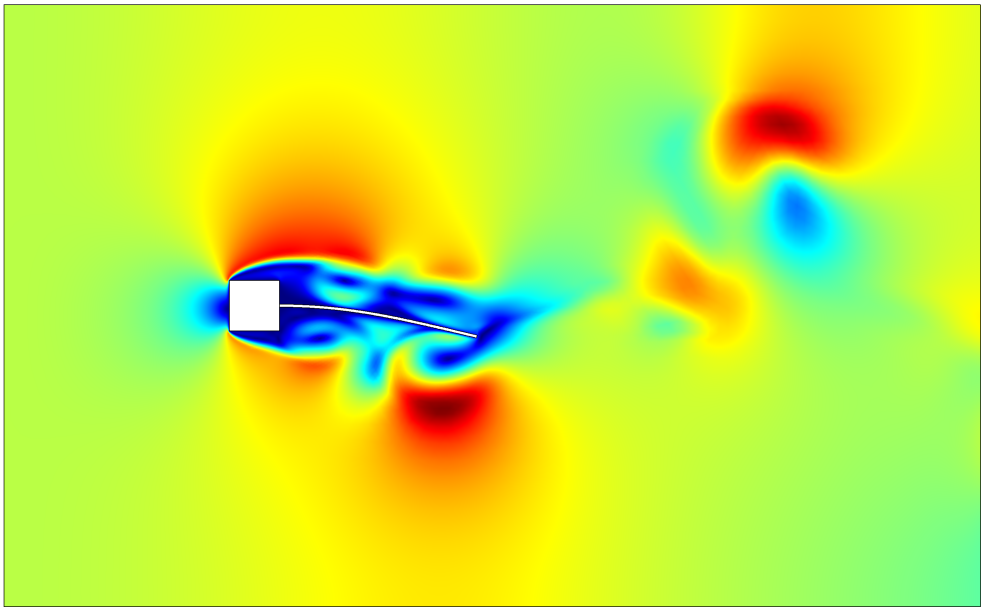

Figure 41: Velocity field after 2.6 seconds. Comsol's fully coupled approach.

8.1.1 *Rig specifications*

Two computer setups where used for the numerical simulations. The first, a fairly outdated stationary rig, uses an Intel(R) Core(TM) i5-4440 CPU with clock rate 3.10 GHz and running a 64-bit operative system. The installed memory is 8.0 GB RAM. This rig was used for running the embedded FSI solvers of COMSOL and Abaqus.

The other rig, a laptop, was mainly used because of issues with server licensing when running MpCCI on the first rig. Therefore the only viable option was

to opt for a second rig to run MpCCI with Abaqus Fluent coupling. The second rig has a Intel(R) Core(TM) i7-3520M CPU with a clock rate of 2.90 GHz. It has 2 Cores and 4 logical processors. This computer also has installed 8.0 GB RAM and is running a 64-bit operative system.

8.2 BENCHMARK MODELLING

The Von Karman benchmark is called by several names. Some refer to it as *flow induced oscillations of a flexible beam* or *flow past a thin elastic beam attached to a fixed rigid block*, which are more specific descriptions. The test problem was proposed in Wall (1999) to study the accuracy and robustness of FSI methods [6].

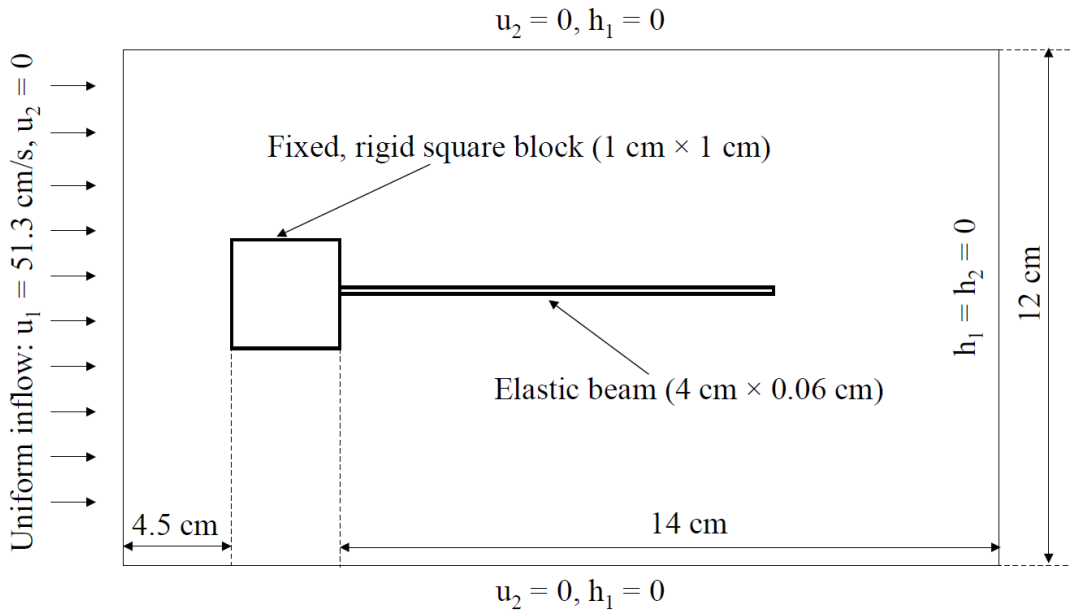

Figure 42: Problem setup [6].

The problem setup is pictured in [Figure 42]. The specifics of this case are listed below.

- Flow is driven by a uniform inflow of 0.513 $\left[\frac{m}{s}\right]$.
- Fluid density is 1.18 $\left[\frac{g}{cm^3}\right]$.
- Dynamic viscosity is 1.82×10^{-5} $\left[\frac{Pa}{s}\right]$.
- The density of the beam is 100 $\left[\frac{kg}{m^3}\right]$.
- The Young's modulus of the beam is 2.5×10^5 [Pa].

- The poisson's ratio is 0.35.
- The Reynolds number is 333.

The mesh is set to be allowed to move freely in the fluid domain except at the inflow and on the rigid block. Here the mesh is fixed. It is also constrained at the lateral boundaries and outflow boundary to not move in the normal direction. In this benchmark the numerical method of ALE is employed. The boundary conditions used are listed below.

- For the fluid: imposed velocity at inlet, slip conditions for the upper and lower wall and a zero pressure at the outlet.
- For the solid: imposed null displacement at the left end.
- For the interface: kinematic continuity ($\boldsymbol{v}_s = \boldsymbol{v}_f$) and dynamic equilibrium ($p_f = \boldsymbol{\sigma}_s \boldsymbol{n}$) are imposed for both strong and weak coupling.

8.2.1 *Structure properties*

The solid beam is to be assumed elastic and compressible. From [Chapter 4] the governing equations describing the structure in 2D is given by

$$\rho \left(\frac{\partial \boldsymbol{v}_s}{\partial t} + (\boldsymbol{v}_s \cdot \boldsymbol{\nabla}) \boldsymbol{v}_s \right) = \boldsymbol{\nabla} \cdot \boldsymbol{\sigma}_s, \tag{72}$$

or in the Lagrangian perspective

$$\rho_s \frac{\partial^2 \mathbf{d}}{\partial t^2} = \boldsymbol{\nabla} \cdot (J \boldsymbol{\sigma}_s \mathbf{F}^{-T}). \tag{73}$$

Here the deformation gradient tensor $\mathbf{F}$ is $\mathbf{F} = \mathbf{I} + \boldsymbol{\nabla} \mathbf{d}$. The Cauchy stress tensor describes the material.

8.2.2 *Fluid properties*

The flow is considered incompressible $\rho = \textit{constant}$, and there is no body forces present $\mathbf{b} = 0$ [6]. The 2D version of the Navier Stokes equations is

$$\begin{aligned} \frac{\partial \rho}{\partial t} + \boldsymbol{\nabla} \cdot \rho \boldsymbol{v}_f &= 0 \\ \rho \left(\frac{\partial \boldsymbol{v}_f}{\partial t} + (\boldsymbol{v}_f \cdot \boldsymbol{\nabla}) \boldsymbol{v}_f \right) &= \rho \mathbf{b} - \boldsymbol{\nabla} p + \boldsymbol{\nabla} \sigma_{dev}. \end{aligned} \tag{74}$$

Thus considering the flow assumptions this becomes

$$\nabla \cdot \boldsymbol{v}_f = 0$$
$$\rho\left(\frac{\partial \boldsymbol{v}_f}{\partial t} + (\boldsymbol{v}_f \cdot \nabla)\boldsymbol{v}_f\right) = -\nabla p + \mu\nabla^2\boldsymbol{v}_f. \tag{75}$$

The variables of interest are the velocity $\boldsymbol{v}_f$ and pressure p.

8.3 COMSOL

The benchmark was first set up in COMSOL. Both the fully coupled and the segregated solver are used. The total simulation time is set to 5 seconds to get perspective both at initial movement and when possibly reaching more or less stable oscillations. Triangular mesh elements are used in both models.

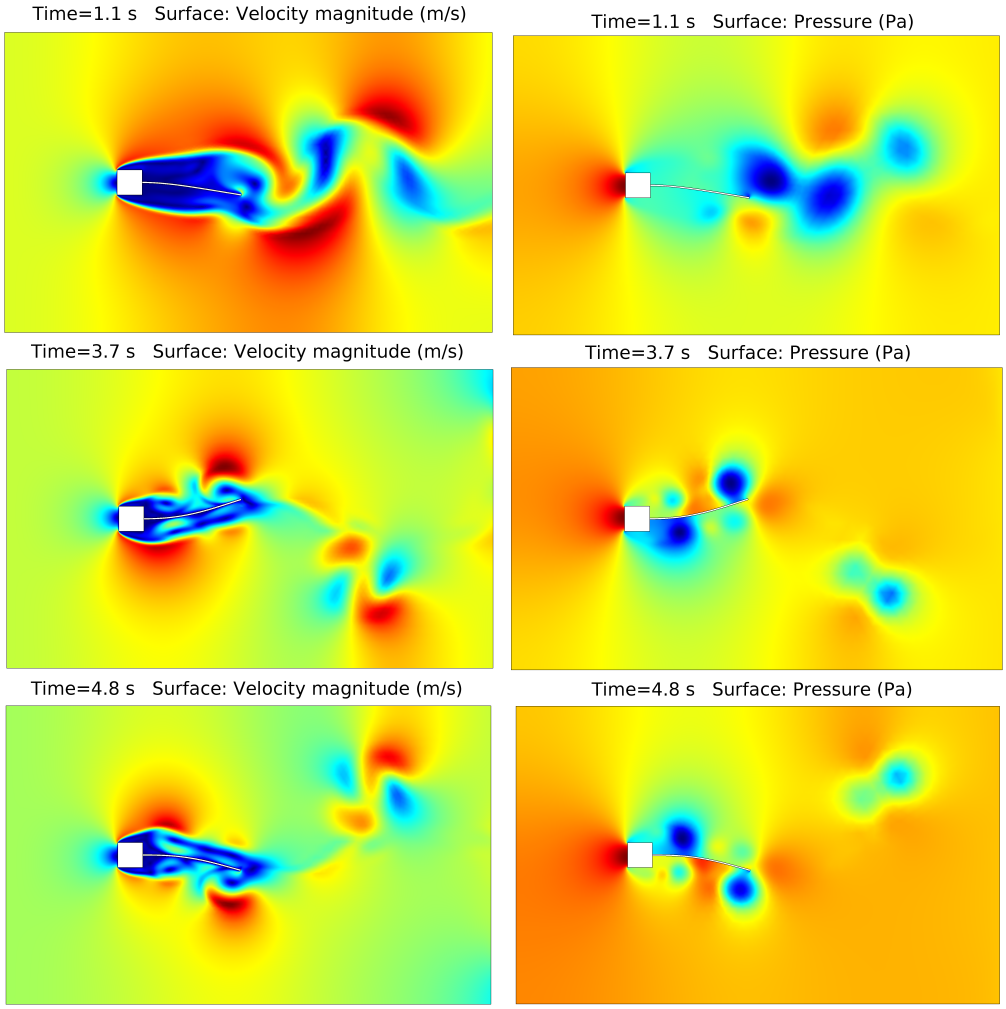

Figure 43: Velocity and pressure plots over time. Fully coupled solver.

Different plots i.e tip displacement, velocity, pressure and converging plots are shown to get a clear view of the simulations. In addition a single fluid

element is monitored in both simulations. The element is chosen at the upper side and downstream of the tip's initial placement at exact coordinates $(110, 80)$ [Figure 44].

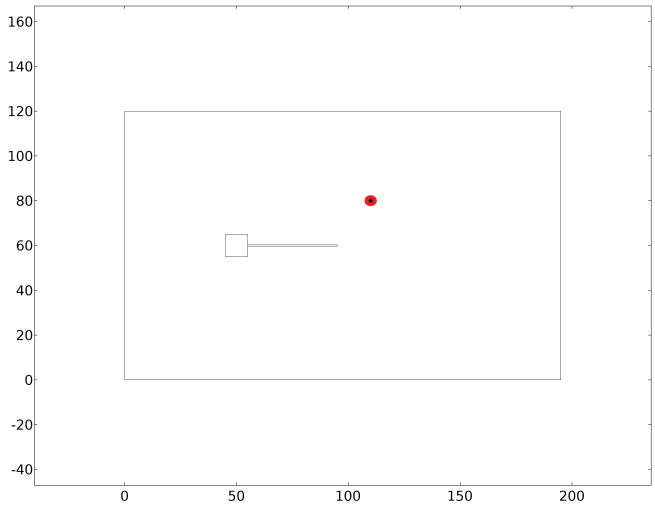

Figure 44: Selected fluid element.

8.3.1 *Fully coupled solver*

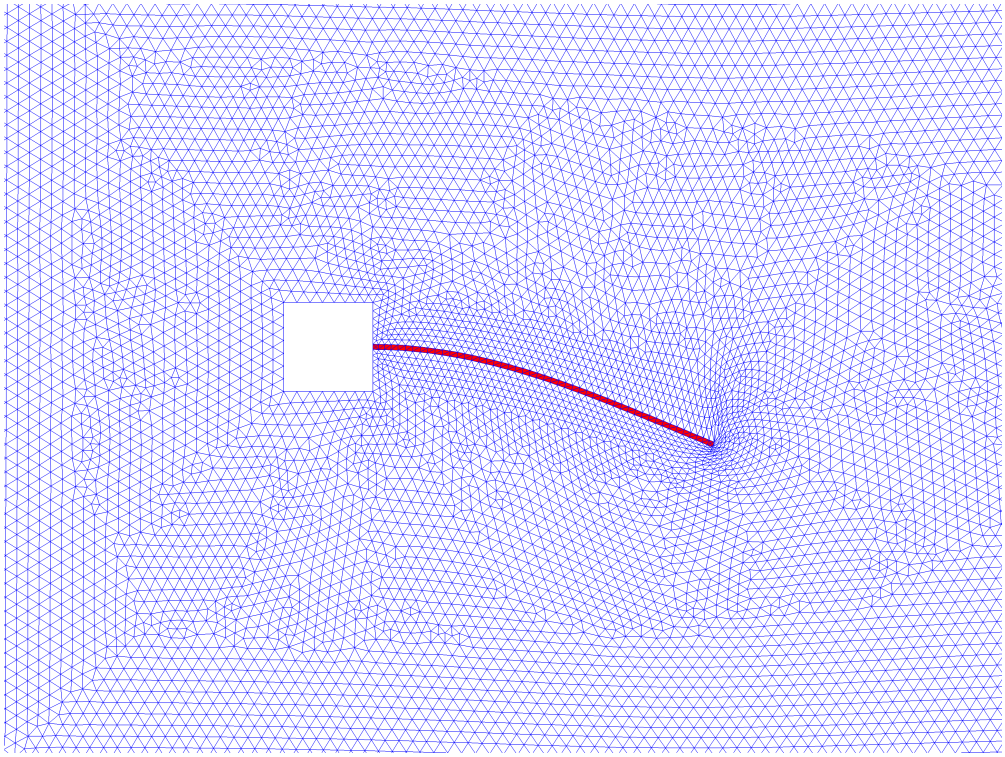

Figure 45: Mesh displacement after 2.0 seconds.

The first attempt at the problem using COMSOL was with the fully coupled solver. The Jacobian is updated once per time step. Geometric nonlinearity is included and Comsol's constant newton scheme for nonlinear methods is used. A dampening factor of 1.0 is used.

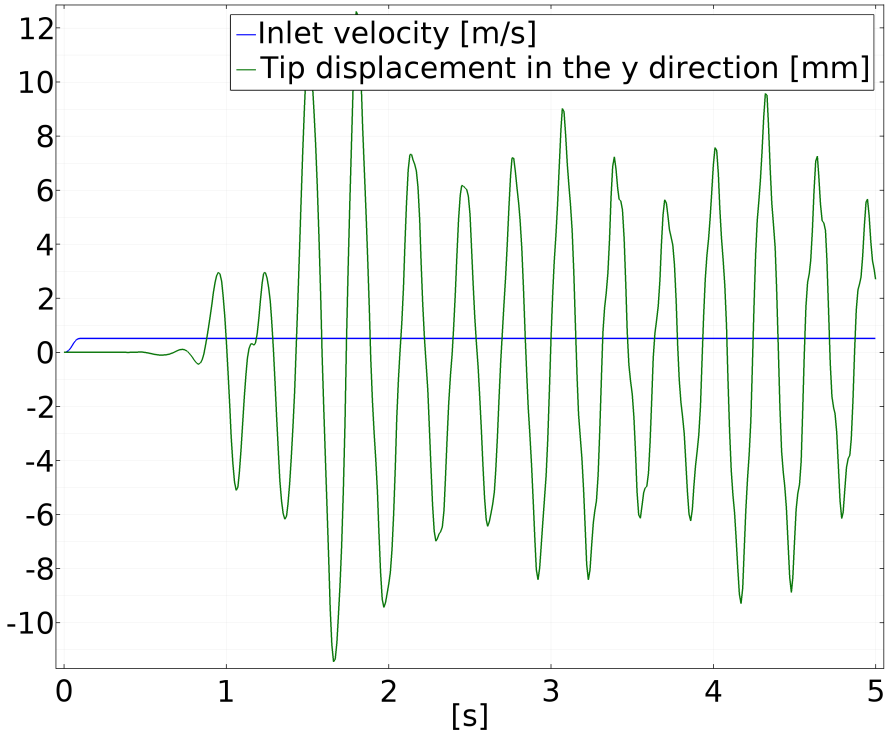

(a) Tip displacement.

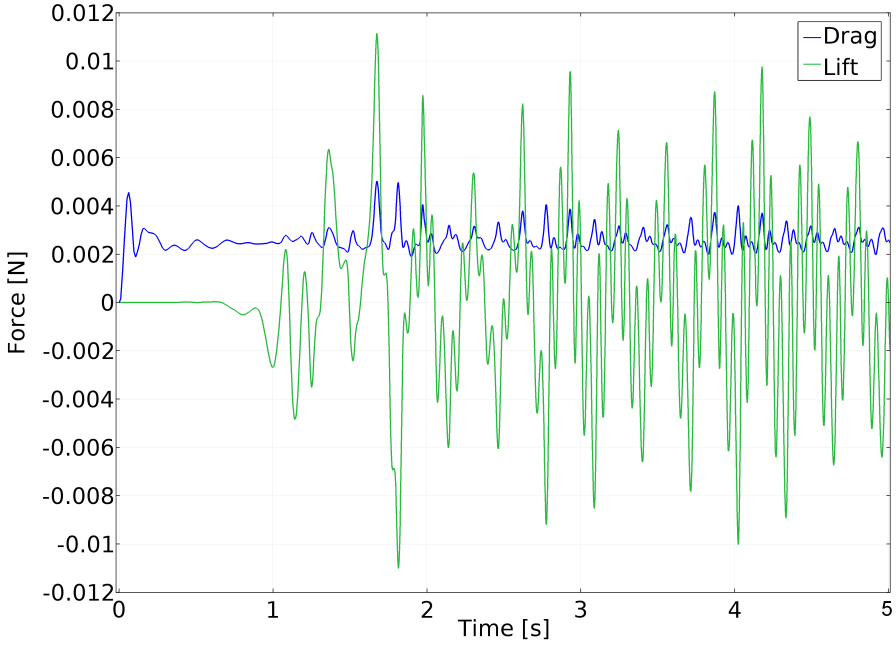

(b) Lift and drag.

Figure 46: Fully coupled approach.

The exact detail of COMSOL's nonlinear method is unknown. The scheme causes the solver to make larger updates in an aggressive manner to speed up the solution progress [23]. It should be noted that solving for non-linearity results in significantly longer solution time. The solution time in this case with a finer mesh consisting of 9458 mesh elements and 338 boundary elements was 1 hour 35 minutes and 41 seconds.

As seen in upper graph in the [Figure 46], there is no movement to the tip before 0.5 seconds. The inlet velocity follows a ramp function shown by the red line going from zero to full velocity at the start up. This was implemented as a safety precaution to get the simulation to run past the fluctuations at the beginning. Which would become greater at higher velocities. Thus a small delayed response in the simulation is seen.

8.3.2 *Segregated solver*

After the fully coupled solver, the problem was set up in COMSOL's segregated solver. The segregated solver uses two main steps, one for each material involved. The first segregated step is in this case for the solid displacement field which has spatial coordinates as variable. The second step is for the fluid velocity field, which uses the pressure as variable. The maximum number of iterations allowed within each step is set to 20, which is the default. As in the fully coupled solver the Jacobian is updated once per time step, and the solvers non-linear method is set to constant newton with a dampening factor of 0.6. In this case solution time with mesh consisting of 18800 mesh elements and 338 boundary elements was 3 hours 20 minutes and 48 seconds.

As can be seen in the figure for tip displacement [Figure 47], the oscillations for the segregated approach reach close to about 6.5mm amplitude before 5 seconds pass. Just like the fully coupled approach the inlet velocity in the segregated approach follows a small ramp function at the start of the simulation, seen by the red line.

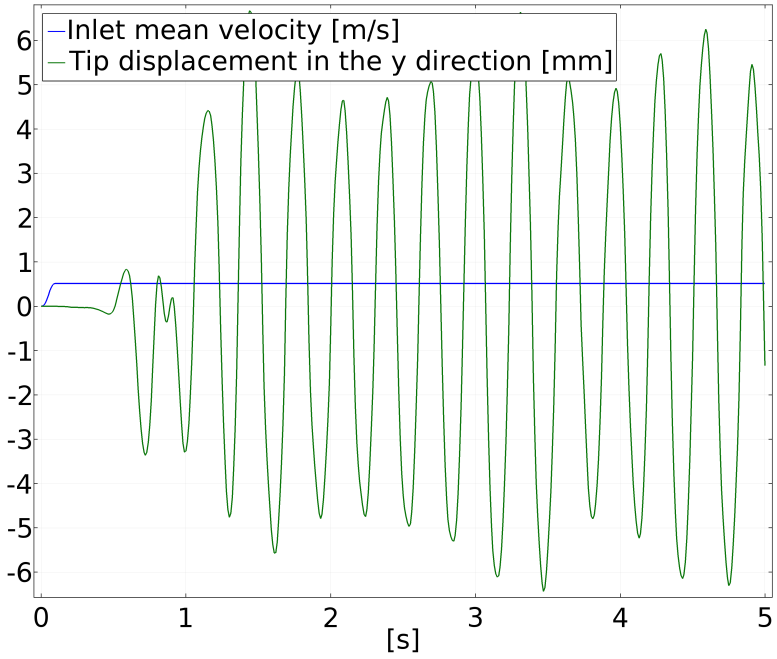

(a) Tip displacement.

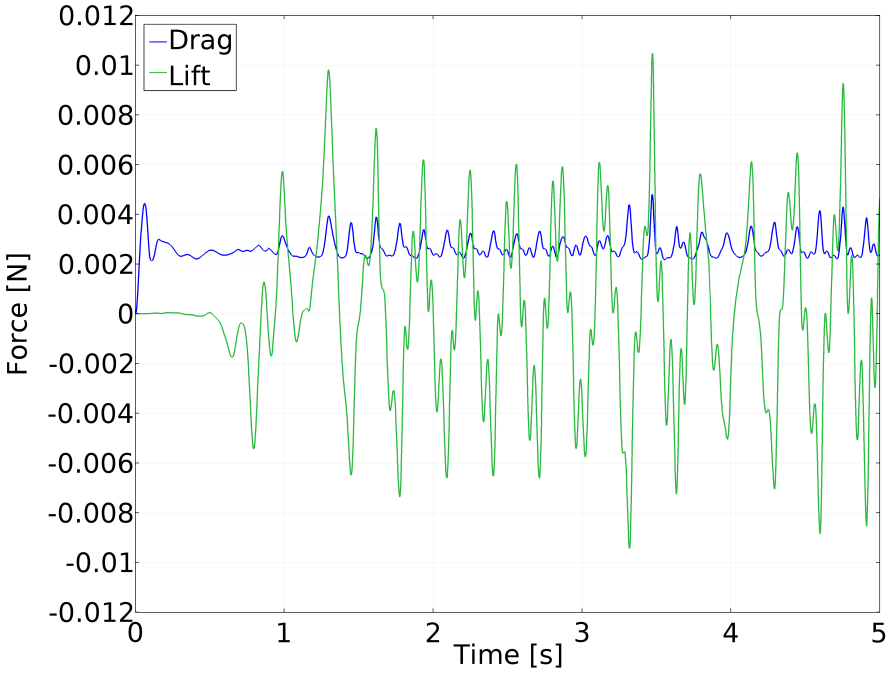

(b) Lift and drag.

Figure 47: Segregated approach.

The results for the selected fluid element downstream of the tip for both the fully coupled and the segregated approach is given side by side in [Figure 48]. Also in these plots differences can be seen between the two simulations. The different mesh used in the two simulation is surely responsible to some degree,

but this alone is unlikely to explain the difference seen. Another reason might be a less strict convergence criteria in one of the two.

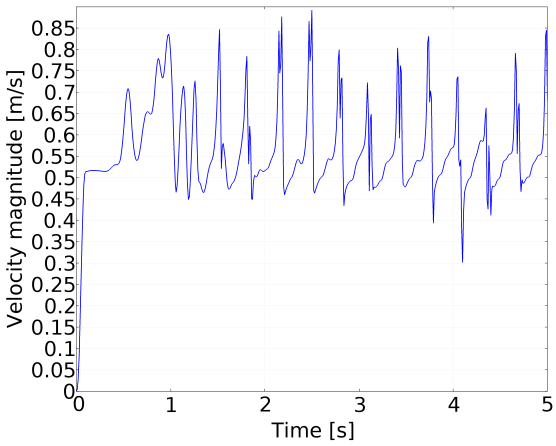

(a) Element velocity.

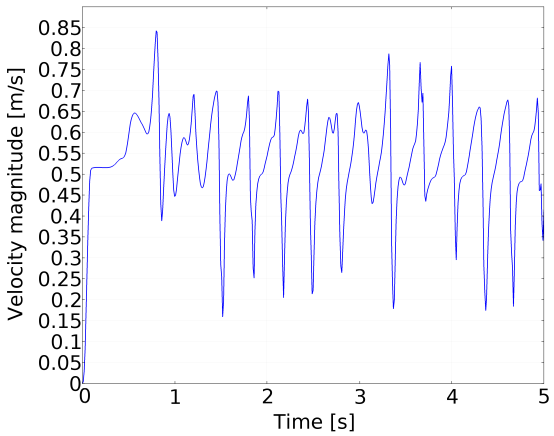

(b) Element velocity.

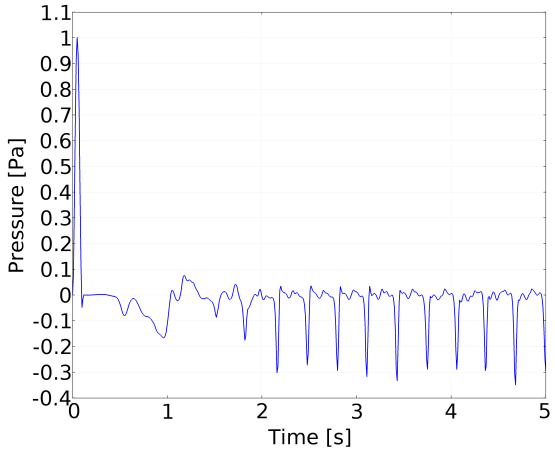

(c) Element pressure.

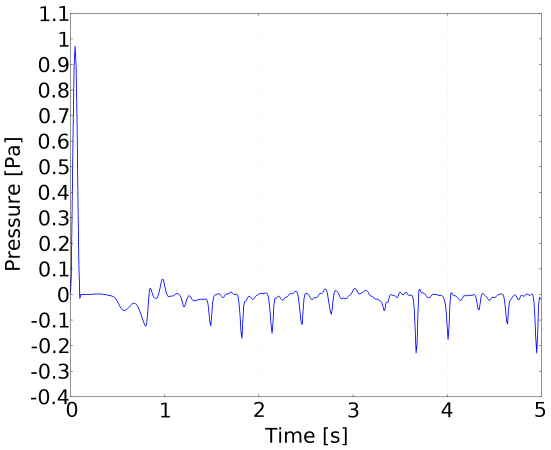

(d) Element pressure.

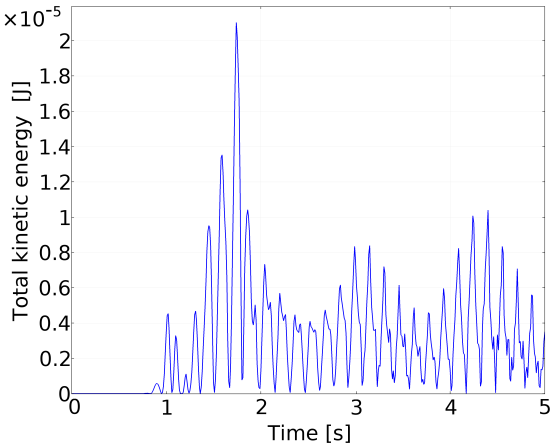

(e) Total kinetic energy.

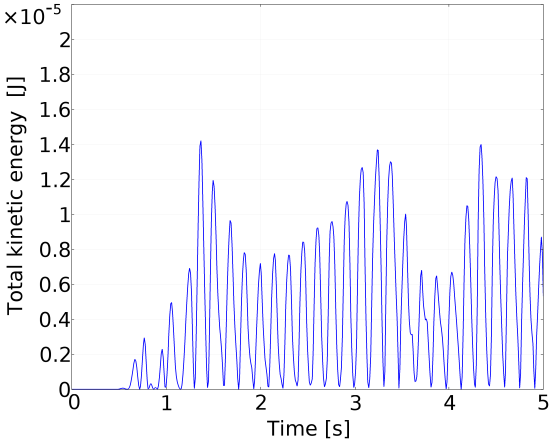

(f) Total kinetic energy.

Figure 48: Comparison of the selected fluid element. Fully coupled to the left. Segregated solver to the right.

Both the fully coupled and segregated solver should reach the same results as long as there is no difference in the model description, i.e mesh or other criteria. However, the default convergence criteria are sometimes too loose. The convergence tolerances with both solvers should be tightened to make sure that they reach the same solution. The same solution should be reached expect when the simulation has no unique solution. This seems to be an issue between the two simulations as they vary in the results produced. The convergence plots are given in [Figure 49].

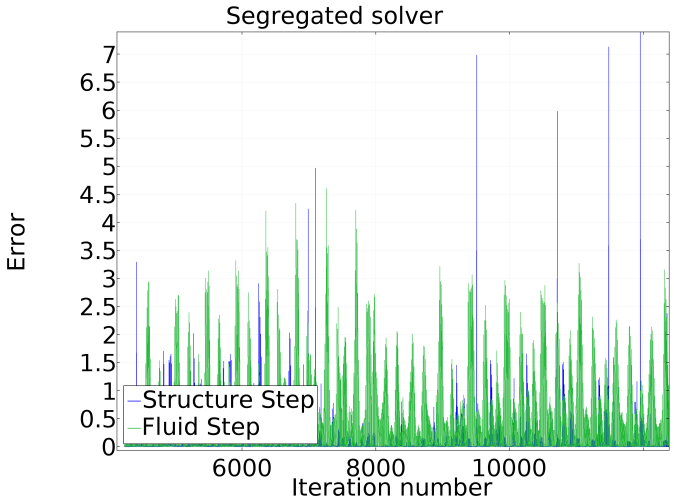

(a) Residual error in the segregated approach.

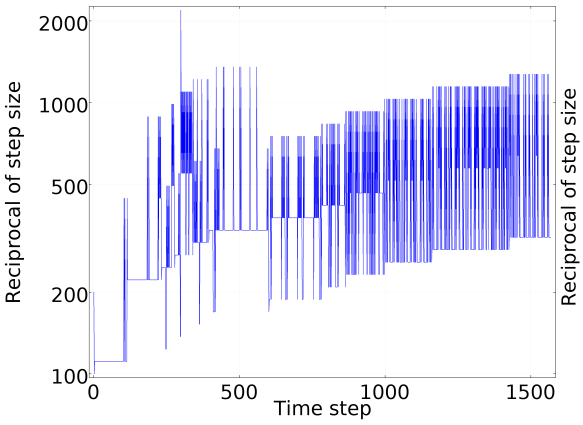

(b) Fully coupled approach.

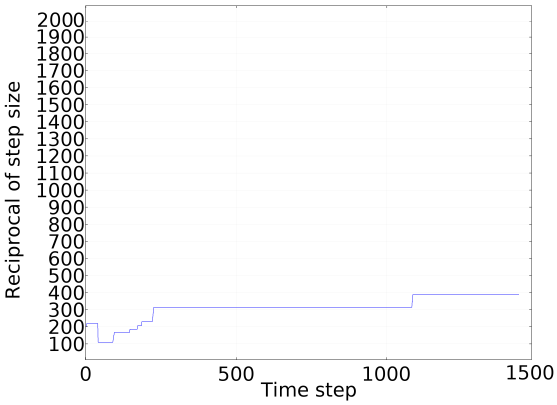

(c) Segregated approach.

Figure 49: Residual errors and reciprocal of step size.

As can be seen the residual error for both the fluid and structure segregated steps is quite high. Thus the criteria should be tightened further. The reciprocal of step size is one divided with the actual step size, $[\frac{1}{\Delta t}]$. COMSOL has the ability to change the step size under simulation [23]. This is done by default if not checked, like in this case. If the convergence criteria are being held with good margin the step size is increased by the solver. If however the margin is low, COMSOL reduces the step time such that the margin to the criteria is

held. Thus a large reciprocal of step size is deemed to result in poor solution accuracy.

8.4 ABAQUS

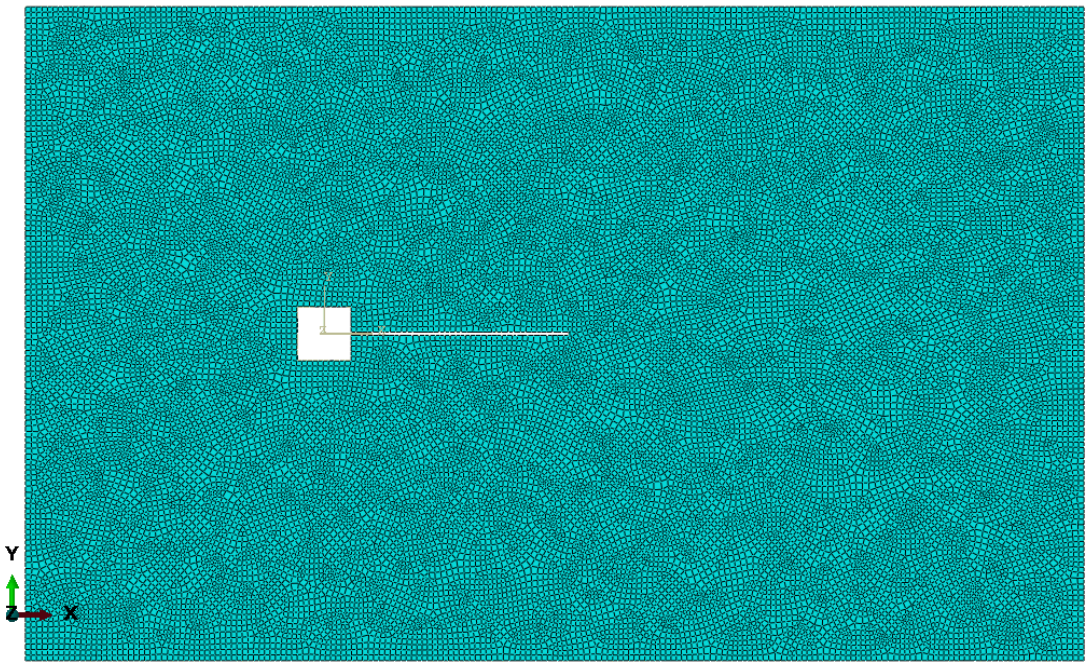

(a) Whole fluid mesh.

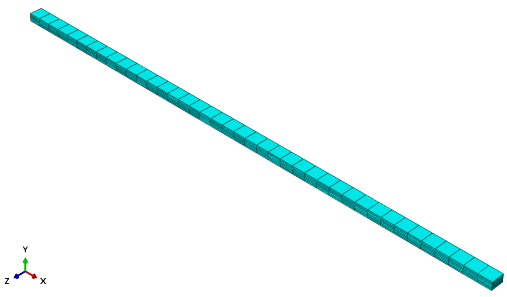

(b) Whole structure mesh.

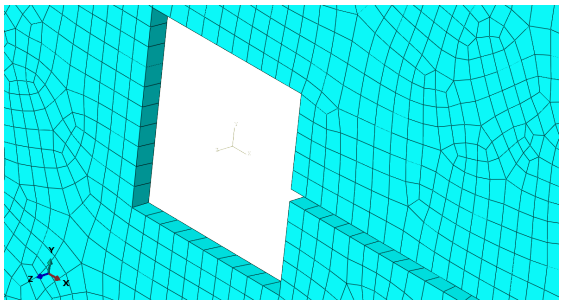

(c) Obstacle in fluid mesh.

Figure 50: Abaqus 3D mesh one element thick.

An attempt to simulate the benchmark was also made with the embedded Abaqus FSI solver. The FSI partition in Abaqus is done by first creating two models. One for the fluid domain and another for the solid, Abaqus CFD and CAE models respectively. Solving by the embedded FSI solver of Abaqus is called co-simulation. Unfortunately it is not possible to do a standard 2D co-simulation in Abaqus. This is because at this time the Abaqus CFD solver only supports 3D modelling. However, by choosing 3D and setting the depth of the mesh cell equal to one element thick (typical in the z-direction) it could

perhaps be able to perform like the 2D case. This however is not confirmed by the Abaqus developers.

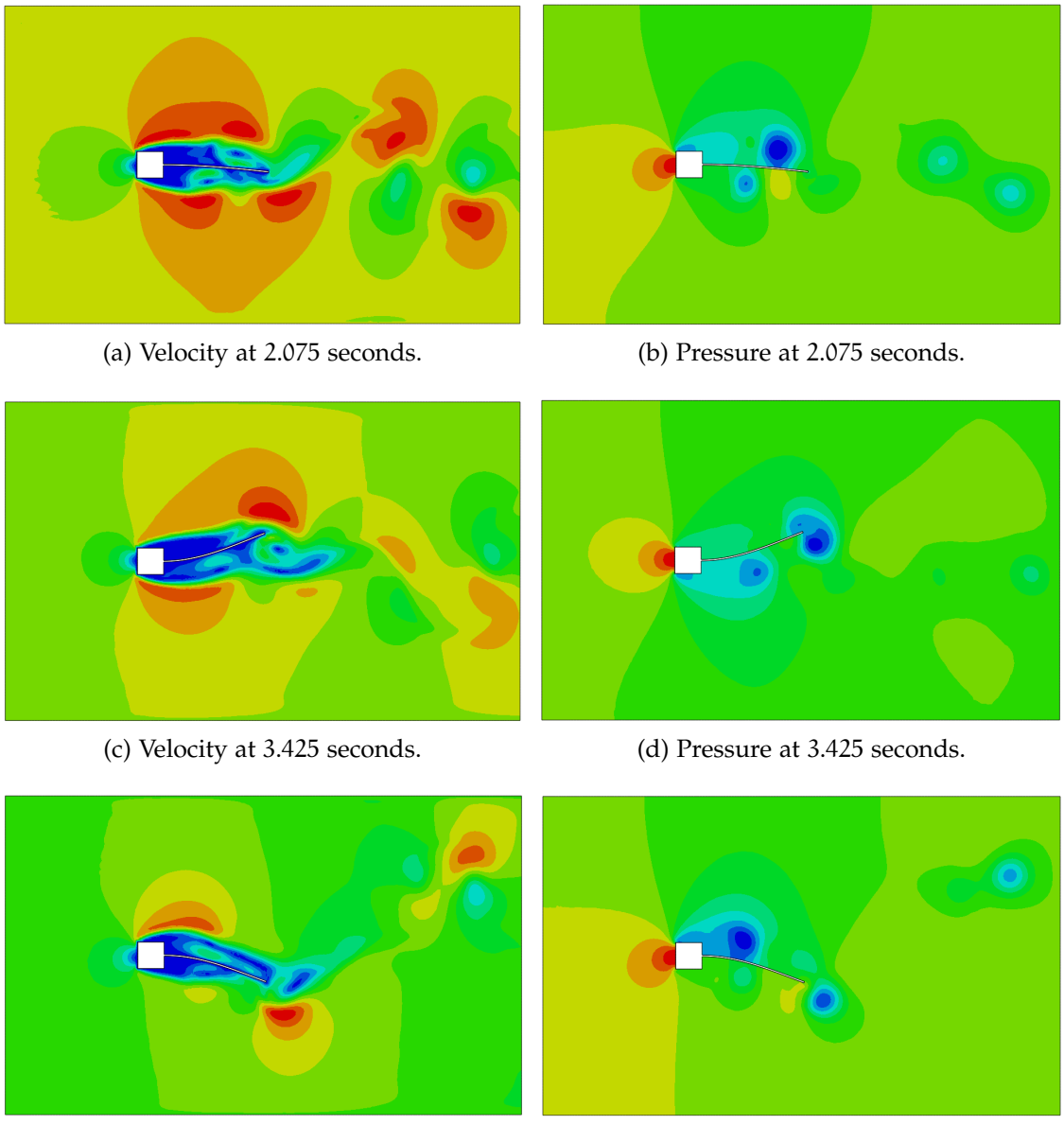

(a) Velocity at 2.075 seconds.

(b) Pressure at 2.075 seconds.

(c) Velocity at 3.425 seconds.

(d) Pressure at 3.425 seconds.

(e) Velocity at 4.5 seconds.

(f) Pressures at 4.5 seconds.

Figure 51: Velocity and pressure plots over time. Abaqus embedded 3D solver.

The velocity and pressure plots for the benchmark simulated in Abaqus are shown in [Figure 51]. The Abaqus version used is v. 6.12 and licence are provided to students by NTNU.

A fairly straight forward mesh is used. The fluid mesh consists of 28578 HEX8 elements and the solid mesh consists of 240 C3DR8 elements. The C3DR8 is a general purpose eight node linear brick element with reduced integration to one point [45]. The open square seen in the fluid mesh in [Figure 50] is

imposed a no-slip condition and has no flow moving through it, such that it is considered a fixed solid block from the fluid perspective. The solid flag is modeled as a simple beam which is constrained at the left end where it is in contact with the open square. Thus meshing the fixed solid square is avoided and less elements needed. The intersection between the two domains are set to where the solid flag mesh is in contact with the surrounding fluid mesh.

It should be noted that simulating in 3D, even if only one element thick, will cost more than the 2D case due to using elements with higher node count. It may also be beneficial to consider the computational cost which arise when simulating a finer mesh in large areas of the CFD model. To make it easier for the two models to interact, it is advised to use about equal grid size of the models. However, solvers today often has the ability to handle non-conformities in meshes [37]. Thus this should not be a considerable problem.

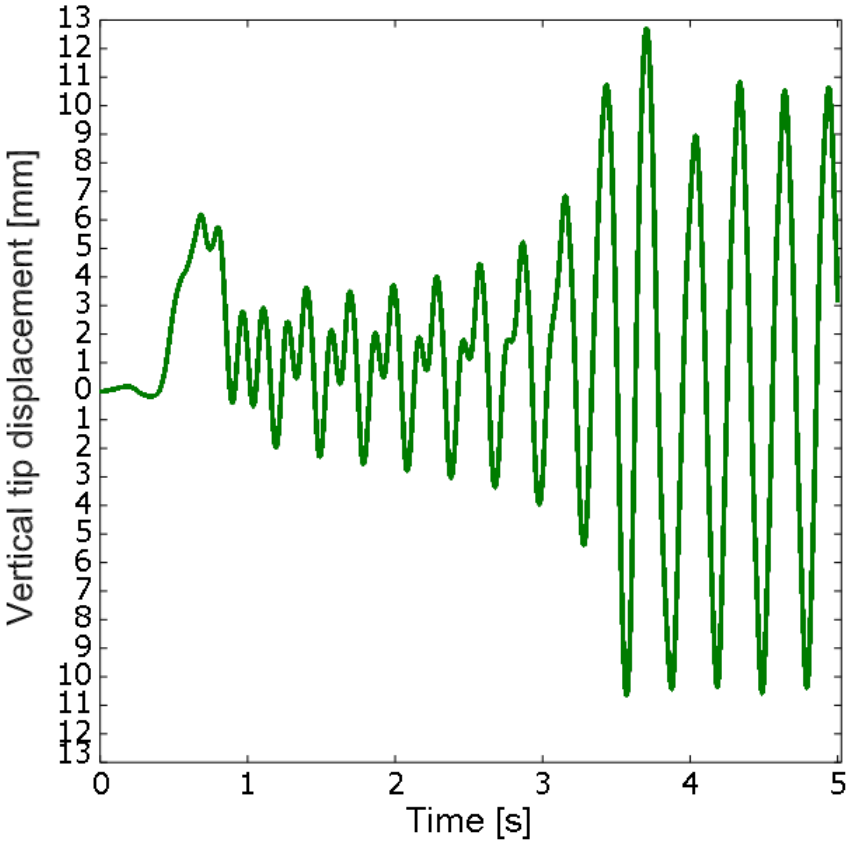

Figure 52: Vertical tip movement.

A dynamic explicit solver was chosen for the structural part. The FSI is done by co-simulation, which is a step-wise solving of the models. Based on the selected time step, the CFD solver will solve for the fluid in lesser steps until the coupling step is reached. When the coupling step is reached the Abaqus CAE solver solves for the structure. In this simulation the CFD time step was fixed to a low step size, 0.0005 seconds. The structural explicit solver would

solve at 100 times that, every 0.05 seconds. The simulation continues in this segregated manner until a solution is reached. This is unlike when using the dynamic implicit solver for the structure, where the time step of one model becomes strictly dependent on the other. If the CFD model is dependent on a time step far lesser then the solid model solved by FEM would appreciate, the simulation might crash.

With a total run time of approximately 6 hours and 30 minutes. The simulation reach what seems to be more or less stable vertical tip displacement oscillations in about 4 seconds [Figure 52].

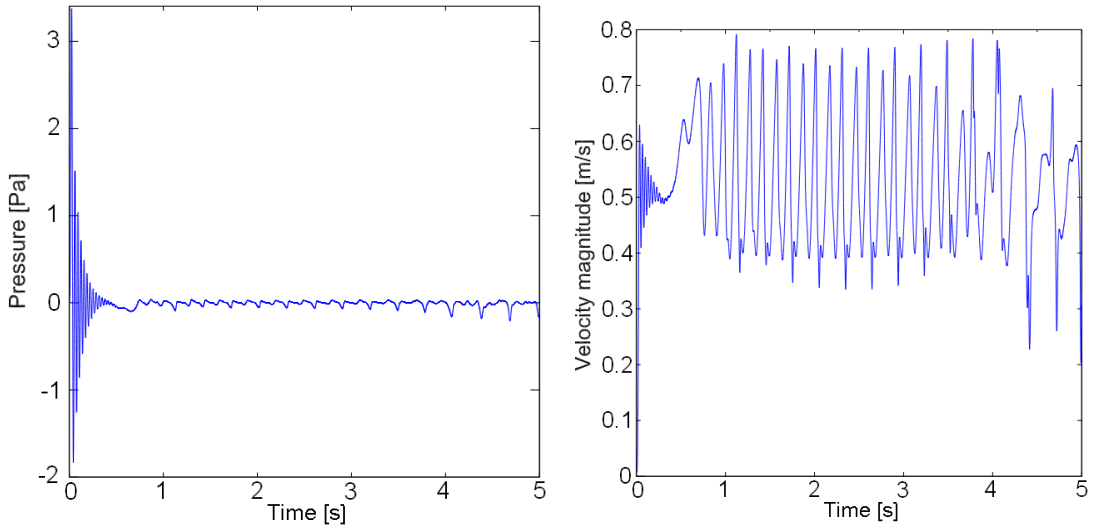

(a) Pressure plot.

(b) Velocity plot.

Figure 53: Node point pressure and velocity.

As seen in [Figure 52], the later displacements seems to be in agreement with expected results. However, it is obvious that the mesh in this simulation could be better tuned around the structure and coarser towards the inlet, outlet and lateral boundaries. Less elements on the whole could make it possible to increase the step size, gain performance during simulation, reaching a solution faster and with better accuracy. The structure mesh could be divided into more elements, enabling better accuracy of the motion.

The plots given in [Figure 53] shows the pressure and velocity at the unique nodal point chosen downstream just like in the case of the COMSOL simulations. These plots also seems to be congruent with earlier simulations. The pressure oscillates more initially, but settles as expected oscillating around zero as time passes.

8.5 ABAQUS COUPLED WITH FLUENT

To expand the horizon and find possible approaches to solving FSI problems a coupling of Abaqus with Fluent was attempted. This was done with the use of the coupling code MpCCI by Fraunhofer SCAI. The main goal by this approach was to find out if the usage of MpCCI was in all doable and creditable.

Fortunately the MpCCI software has a manual for details and instructions on usage [37]. The manual also contains some tutorials in 2D and 3D which can be run if licences to the specific solvers to couple are held. A similar problem tutorial of flow induced oscillations of a flexible beam was actually found in this manual. Therefore the only challenge was to redefine the simulation and indeed run it through Abaqus coupled with Fluent. This however proved to be a cumbersome task. Mainly because of server license issues with Abaqus at NTNU, but also because the input files from the tutorial seemed outdated. Thus modifications had to be made to the coupling and input files.

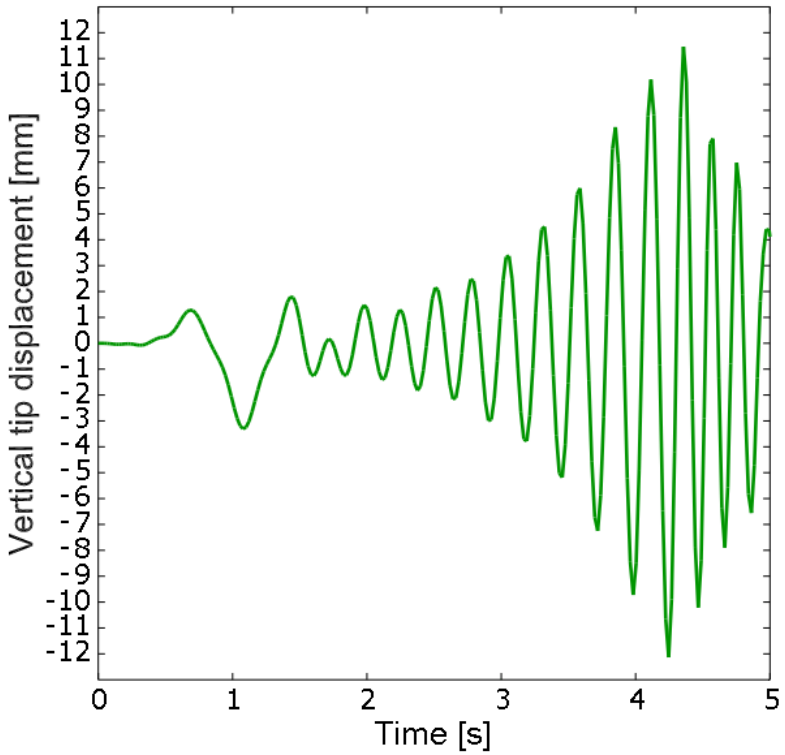

Figure 54: Vertical tip movement.

After adjustments the oscillations happens frequently. This is coherent to the other simulations done by the embedded solvers of COMSOL and Abaqus. The run time for this simulation was fairly quick, about 20 minutes. The vertical tip movement can be seen in [Figure 54].

The fluctuations created by the low solid density, Young's modulus and high fluid inlet velocity can be troublesome to handle for the solvers. It can there-

fore be important that the fluid mesh is predisposed to foresee large movement and that the overall quality is sufficient. In addition the time step should be minimal. If not the possibility for negative volumes or inverted mesh cells are greater. The simulation would only run at one specific time step of 0.02. The exact reason for this is not known. The coupling had trouble following the fluctuations at the beginning. By raising the time step it is possible these fluctuations were not accounted for properly, thus giving the coupled solvers the ability to continue. If using an inappropriate time step the solution will often either produce ill-shaped results or diverge to the extent that the convergence criteria ends the simulation.

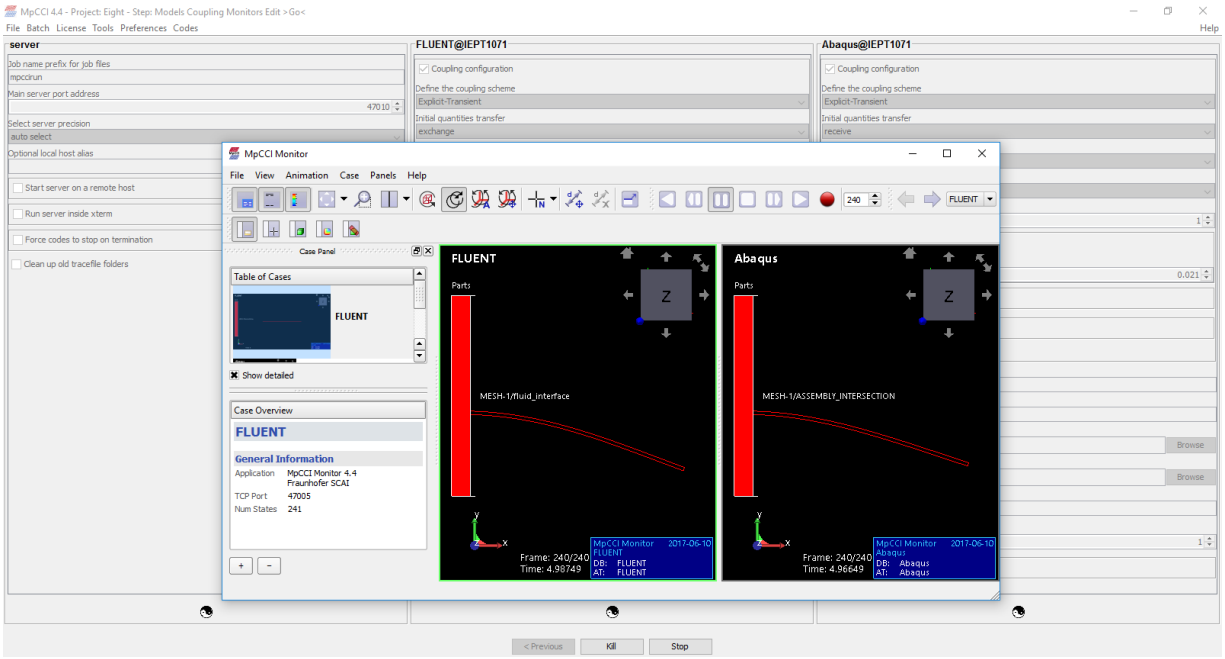

Figure 55: MpCCI interface.

The MpCCI GUI (background) and the MpCCI Monitor (foreground) interface is shown in [Figure 55]. Even though the simulations were not managed to run to an desirable extent, the main goal of this specific simulation was reached. The coupling code MpCCI proves to be usable in coupling different solvers. However, to which extent is not known for sure. Due to less experience with the usage of MpCCI and external coupling codes in general at NTNU, this might be a step towards gaining experience with just that. In retrospect the task seemed much more cumbersome than it actually was, which tend to be common when applying unknown methods of simulation.

8.6 COMPARING RESULTS

A comparison of the vertical tip displacement from the simulations are given in [Figure 56]. The plot scales and color are matched to enable a clearer view.

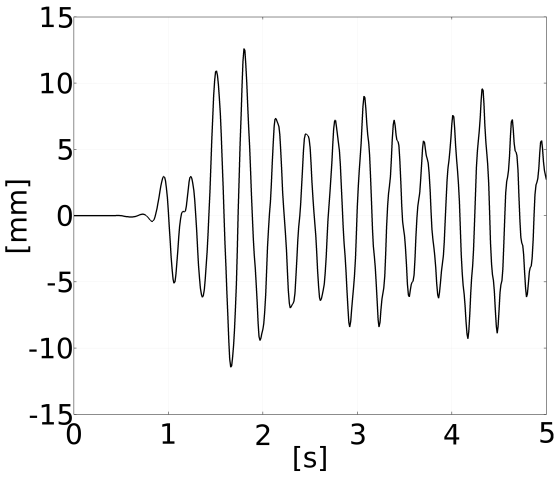

(a) COMSOL fully coupled approach.

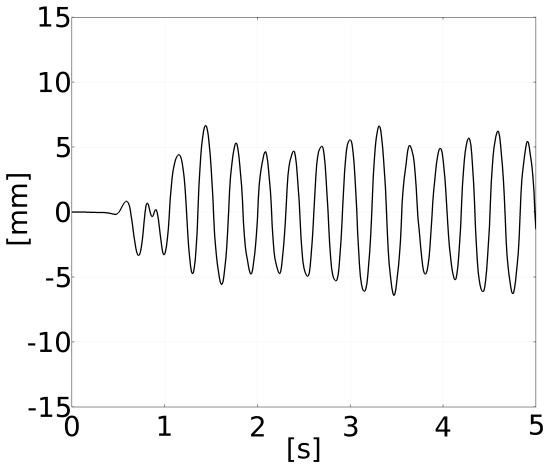

(b) COMSOL segregated approach.

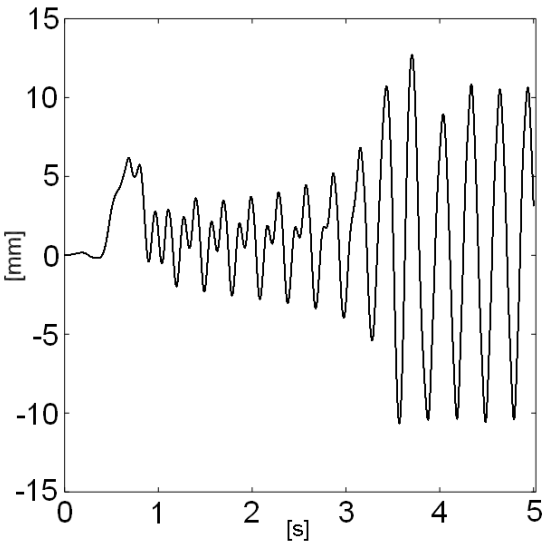

(c) Abaqus 3D embedded solver.

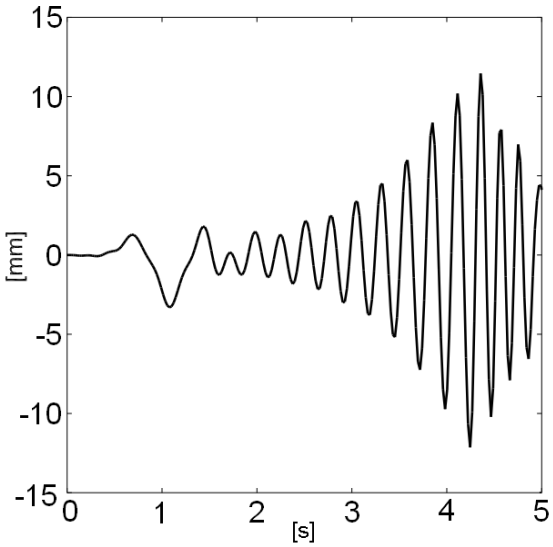

(d) Abaqus and Fluent via MpCCI.

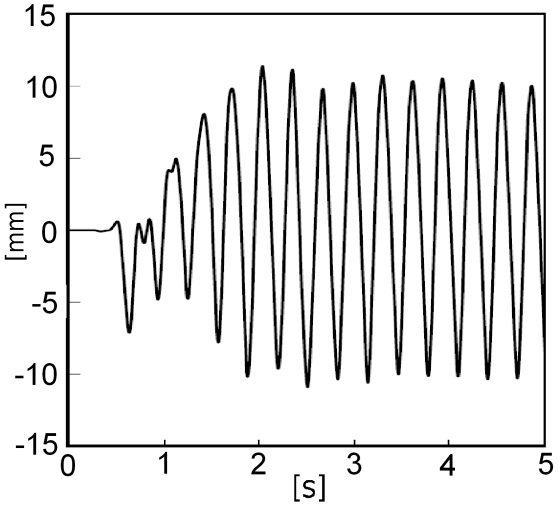

(e) Data from *Froehle et al., 2015* [14].

Figure 56: Comparison of tip movement.

SOLVER	NUMBER OF ELEMENTS	SOLUTION TIME
COMSOL fully coupled	9796	1 h 35 min 41 s
COMSOL segregated	19307	3 hours 20 min 48 s
Abaqus embedded	28578	6 h 30 min
MpCCI coupling	9388	20 min

Table 2: Number of elements and solution time by the respective solvers.

The number of elements used and the respective solution time for each solver are shown in [Table 2]. The number of elements used are fairly high, especially in the 3D embedded Abaqus simulation. This simulation required a finer mesh around the tip to be able to run. To produce a more defined von Kármán vortex street it is also convenient that the overall fluid mesh is in finer detail.

Distinct differences can be seen in the vertical tip movement plots. In all simulations except the two done in COMSOL the displacement oscillations seems to increase as time goes, up to a certain point. The 3D embedded solver seems to reach and fit the more stable oscillations as expected in comparison to the data from *Froehle et al., 2015* [14]. The displacement plots from COMSOL indicates either not properly defined simulations (i.e mesh, convergence or material properties) or the solver is unable to solve for non-linear behavior in the extent that Abaqus can. The simulation done with MpCCI is most likely not on point due to the inappropriate step size used.

The non-matching results can occur due to numerous reasons. Although perhaps the most likely is modest experience with almost all of the solvers used. The mesh of the fluid and structural domains are set up differently in the solvers. Thus the mesh and the number of elements used is not identical from one simulation to the next. In addition different solving parameters used might not have been considered thoroughly. The probability of not using a correct material description, boundary condition or having managed to not properly define geometry is present. When setting up simulations by uncharted methods such sources of error may occur. Small differences in the results are still to be expected, due to the solvers using different coupling approaches and describing domains based on different numerical methods, specifically the FEM and FVM. In addition some of the solvers are likely more capable at handling nonlinear material behaviour than others.

Plots of the velocity and pressure at the selected point downstream of the tip for some of the different solvers are given in [Figure 59]. Although differences can be seen across the simulations in the plots, there are also similarities in the velocity and pressure response.

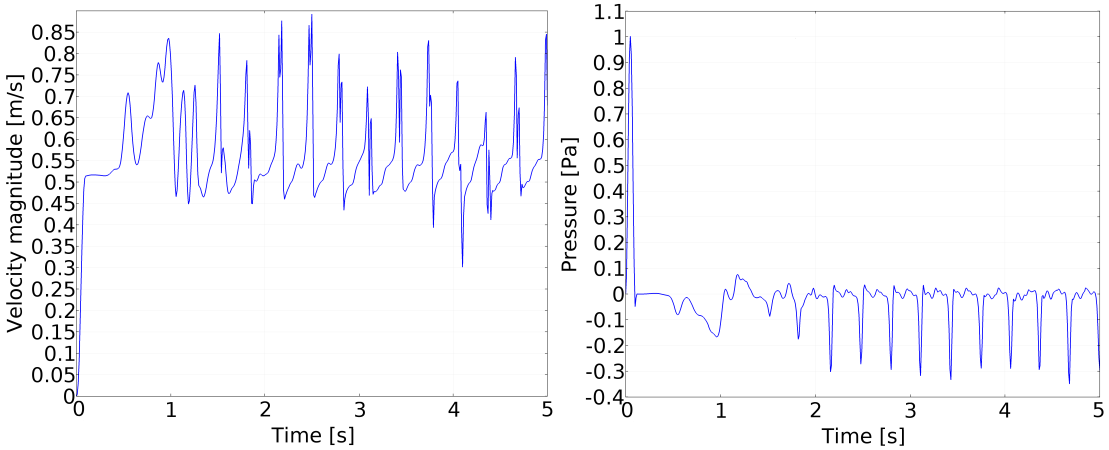

(a) Node velocity. (b) Node pressure.

Figure 57: Comparison of the selected node. COMSOL fully coupled approach.

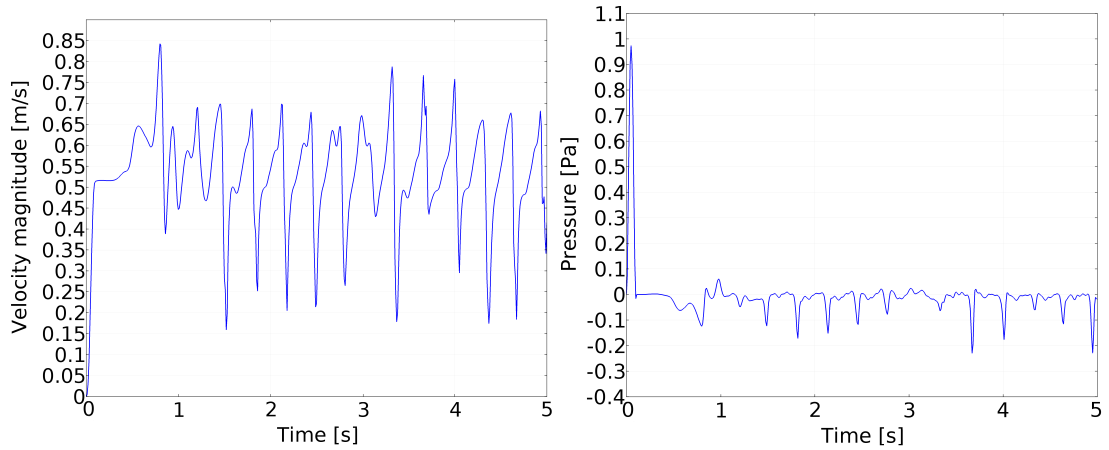

(a) Node velocity. (b) Node pressure.

Figure 58: Comparison of the selected node. COMSOL segregated approach.

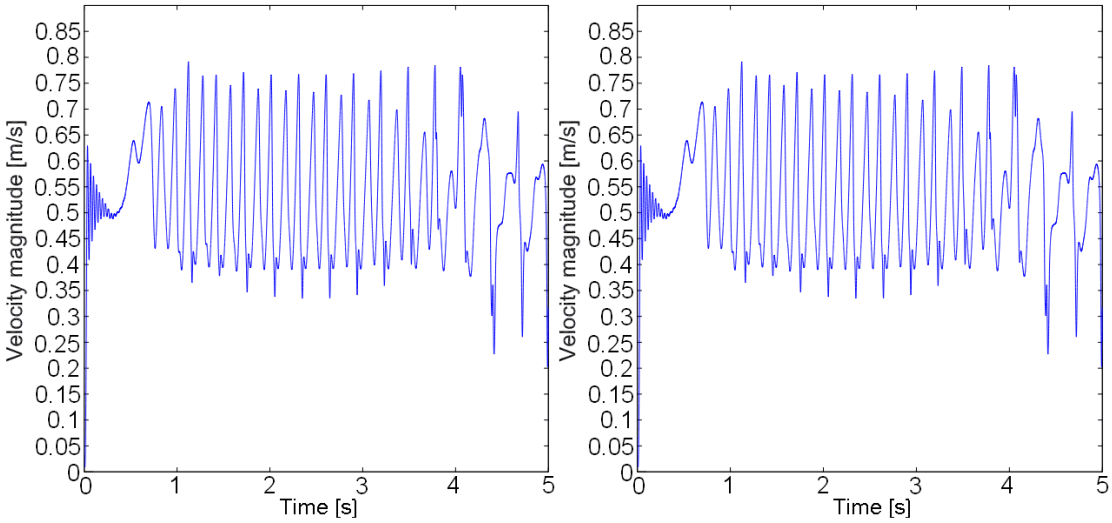

(a) Node velocity. (b) Node pressure.

Figure 59: Comparison of the selected node. Abaqus embedded solver.

A useful way of displaying quality of mesh discretization is by running the simulations with different mesh and time step sizes. Storing these results the tip motion can be plotted in the same figure for the different used number of elements and step sizes. Unfortunately due to the number of simulations this was not done. Only the time step which first proved appropriate to run each simulation was used and it's results kept. Thus the information acquired by this approach on the meshing feasibility is modest. In retrospect, not considering this was surely a mistake.

To get some perspective on the difficulty and issues often encountered when simulating FSI problems some of the results are seen in context of the findings of *Bavo AM et al., 2016* [5].

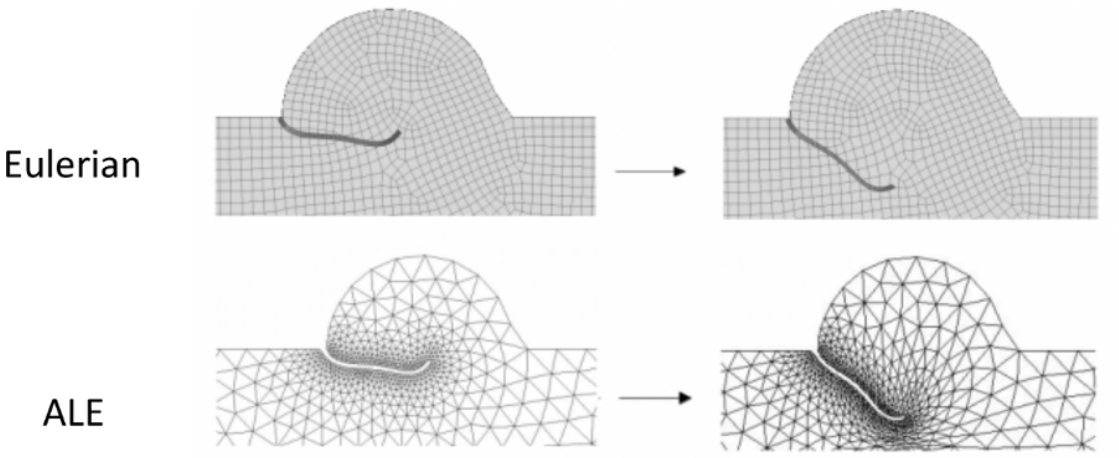

Figure 60: Simulating flexible leaflet by ALE and Eulerian technique [5].

The process of FSI benchmarking can be a cumbersome process, not unlikely to run into convergence failure due to inappropriate discretization and step size, misrepresentative initial and boundary conditions, equilibrium equations not solved properly and all of the issues mentioned above. Most of which was touched by the simulations done in this report.

The performance of the benchmark simulations done in this report seems particular limited by mesh motion and deformation of the fluid domain. Using the ALE method might not be adequate in describing large deformations. It is also important to note that the choice of solver will influence the results. As partly mentioned in [Chapter 3] there are some typical issues considering the ALE method. When both structural and fluid grid deforms, it generally has higher computational cost compared to for instance the immersed boundary method (IB) [5]. Thus for problems where conforming mesh are used and the structural domain undergoes large displacements, issues often appear. In addition, a very refined fluid mesh is required in the area of movement. This can be seen in [Figure 60]. As stated by *Bavo AM et al., 2016* [5]:

"Theoretically the ALE technique would be preferable when the interface is sharply defined, and the variables are calculated directly on the surface and not obtained from the interpolation, as in the IB methods."

	2D		3D	
	ALE-FSI	IB-FSI	ALE-FSI	IB-FSI
SOLID	500	300	5200	1250
FLUID	2400	3500	150000	1150000

doi:10.1371/journal.pone.0154517.t001

(a) Number of elements used.

2D		3D	
ALE-FSI	IB-FSI	ALE-FSI	IB-FSI
48 h	1h	> 3 weeks (early opening)	30 h (entire simulation)

doi:10.1371/journal.pone.0154517.t002

(b) Time.

Figure 61: Comparison of computational time by ALE and IB methods [5].

Admitting the accuracy potentially gained from the ALE method, it might not be suitable for simulating larger 3D problems where high structural displacements take place. If the fluid grid is under severe deformation in a limited amount of time the remeshing and smoothing algorithms to preserve quality for the domain might not be sufficient to ensure convergence. In such cases the simulations are commonly performed with IB based methods, which allows for faster solutions [Figure 61], no remeshing and good handling of the fluid grid deformation [5]. In spite of these suggestions the ALE method is further used in this report to perform the 2D and 3D case of OSA [Chapter 9].

9

PALATE MODELING

9.1 INTRODUCTION

To set up simulations for the case of OSA a simple model was made based on the geometry described by *M.R. Rasani et al., 2011* [35]. The geometry represents a channel domain shown in [Figure 62]. The channel consists of a rigid plate connected to a flexible plate representing the hard palate and soft palate respectively. In addition a obstruction to hinder flow through is introduced. An ALE formulation is used to account for the solid mesh motion that follows the fluid deformation. The flow in this case can be characterized by the unsteady Navier Stokes and continuity equation given in [Chapter 5].

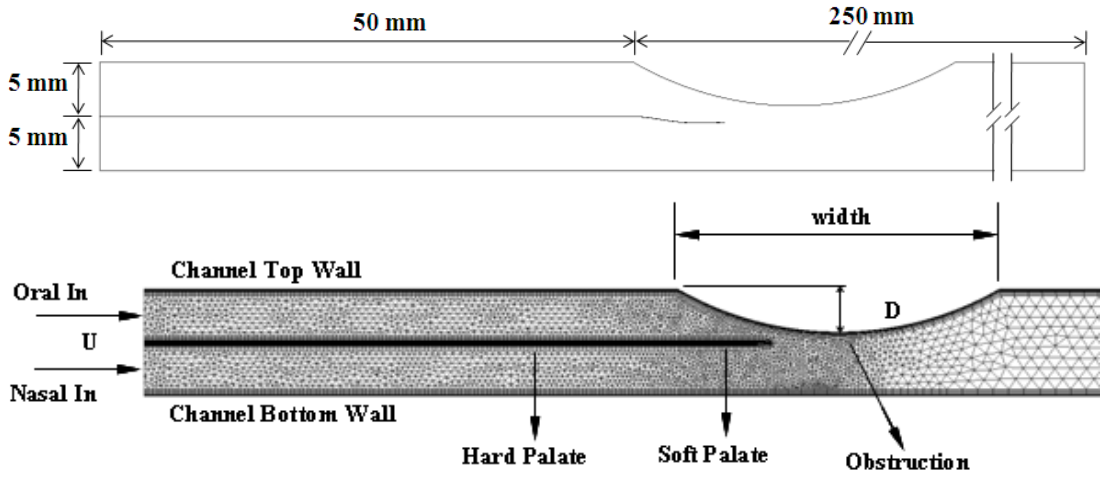

Figure 62: Idealized model of oral and nasal passage through upper airway [35].

The obstruction is representing the tongue moving back into the throat enabling the collapse of the pharynx, as explained in [Section 1.1]. This is modeled as a circular elastic plate which is merged into the channel. In the 2D case both the obstruction and the flexible plate will be subject to deformation. Thus the interface between the fluid and the structures are found at two separate places. The obstruction and soft palate plate are simultaneously interacting with the flow in between. A 2D case is first simulated in COMSOL. Then a 3D case is simulated by the embedded FSI solver Abaqus.

9.2 THE MODEL

The changes in pressure in the channel and the deformation of the elastic plates is monitored when fluid flow is sent through. For simplicity both the obstruction plate and the soft palate plate is considered homogeneous, elastic and isotropic. Thus the properties of both the plates have a constant Young's modulus, E and Poisson ratio, ν. No turbulence model (k-ε) is used to simulate the flow. This is to keep the simulation as simple as possible. Displacements of the midpoint of the upper plate representing the tongue will be monitored as well as the tip of the soft palate plate. Changes in velocity and lift and drag will also be monitored trough the simulation.

The material properties used for the fluid and the solid was set to represent air and the obstruction and soft palate to that of muscle tissue, respectively. For simplicity, the obstruction representing the tongue was initially considered to have density equal to that of water [25]. However, this was changed in the 2D case to be able to better understand special behaviours of the simulation. The material properties used are given in [Table 3].

SOLID	$\rho_s[\frac{Kg}{m^3}]$	$E[Pa]$	ν
Tongue & soft palate	125	1.415×10^5	0.33
FLUID	$\rho_f[\frac{Kg}{m^3}]$		$\mu[Pa \cdot s]$
Air	1.185	-	1.982×10^{-5}

Table 3: Material properties in 2D palate model.

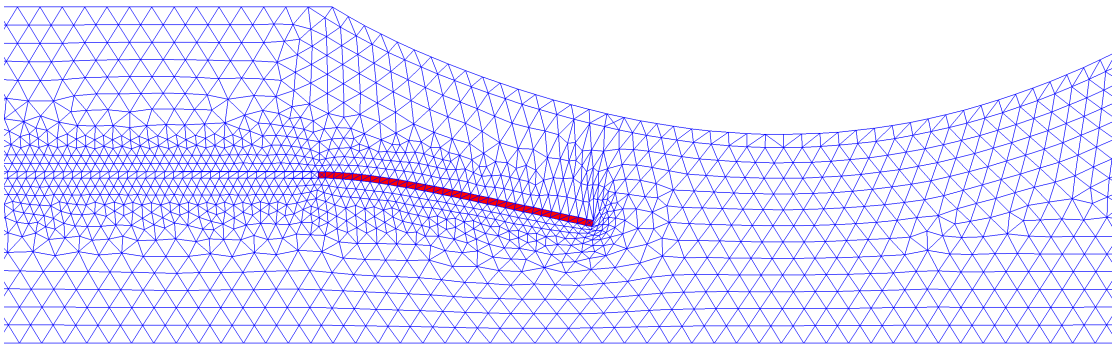

Figure 63: 2D mesh displacement in COMSOL after 0.15 seconds.

9.3 INITIAL AND BOUNDARY CONDITIONS

The inlet condition for the flow was set to velocity of 1.2 $\left[\frac{m}{s}\right]$. At the outlet the pressure is set to zero. In the solid model walls is constrained to be rigid and with a no-slip condition. Only movement in the fluid and in the elastic plates is to be possible. However, initially to keep the simulations simple no force or pressure is applied to the elastic plate from above (which if necessary could act as the weight of the tongue). The mid flexible plate is fixed at the left end where it is in contact with the fixed plate and the elastic obstruction is fixed at the left and right end where it is in contact with the channel walls, and free to move otherwise. The fluid-structure interface is imposed to where the air is in contact with the obstruction and the soft palate.

The 3d case follows the much of the same initial and boundary conditions as the 2D case. However, in this simulation the obstruction is rigid, not able to move. Thus only the soft palate is able to move when interacting with the fluid.

9.4 2D SIMULATION

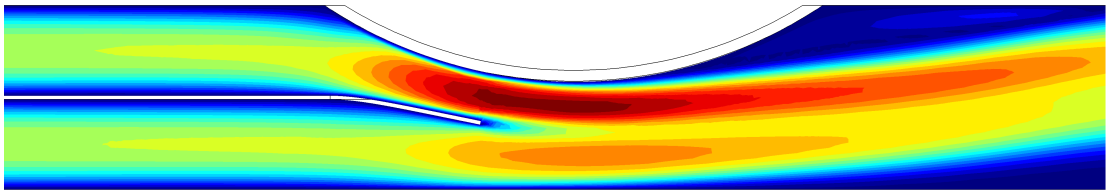

Figure 64: Developed velocity in simple 2D model in COMSOL.

A comparison between two simulations are done. In the second model the obstacle is set at a lower height than in the first, measured from the lowest point on the obstruction to the channel bottom wall. Thus representing the tongue at two initial placements.

The first and second model are given the names; *open model* and *narrow model*, respectively [Table 4]. The thickness of the flexible obstruction and the flexible tip is 0.6 mm and 0.2 mm, in both models respectively. Like in the simulation of the *Flow Induced Oscillations of a Flexible Beam* a fluid element is selected for pressure comparison in the channel, positioned under the obstruction in both models at coordinate $(64, 4)$. This is shown in [Figure 67]. The simulation of the narrow model requires a finer mesh due to the narrowing of the channel resulting in larger movement of the flexible structures. Both simulations is set to run up to a end time of 0.2 second, at constant time step size Δt of 0.001. Both simulations reach a solution in less than 15 minutes.

OPEN MODEL	Number of elements	Height [mm]
	18989	8
NARROW MODEL	Number of elements	Height [mm]
	36122	6

Table 4: Specifics of 2D models.

The flexible plate representing the soft palate is moving down to enable the initially constricted flow on it's upper side [Figure 65]. The obstruction is slightly pushed upwards by the flow, then drawn downwards due to the pressure drop.

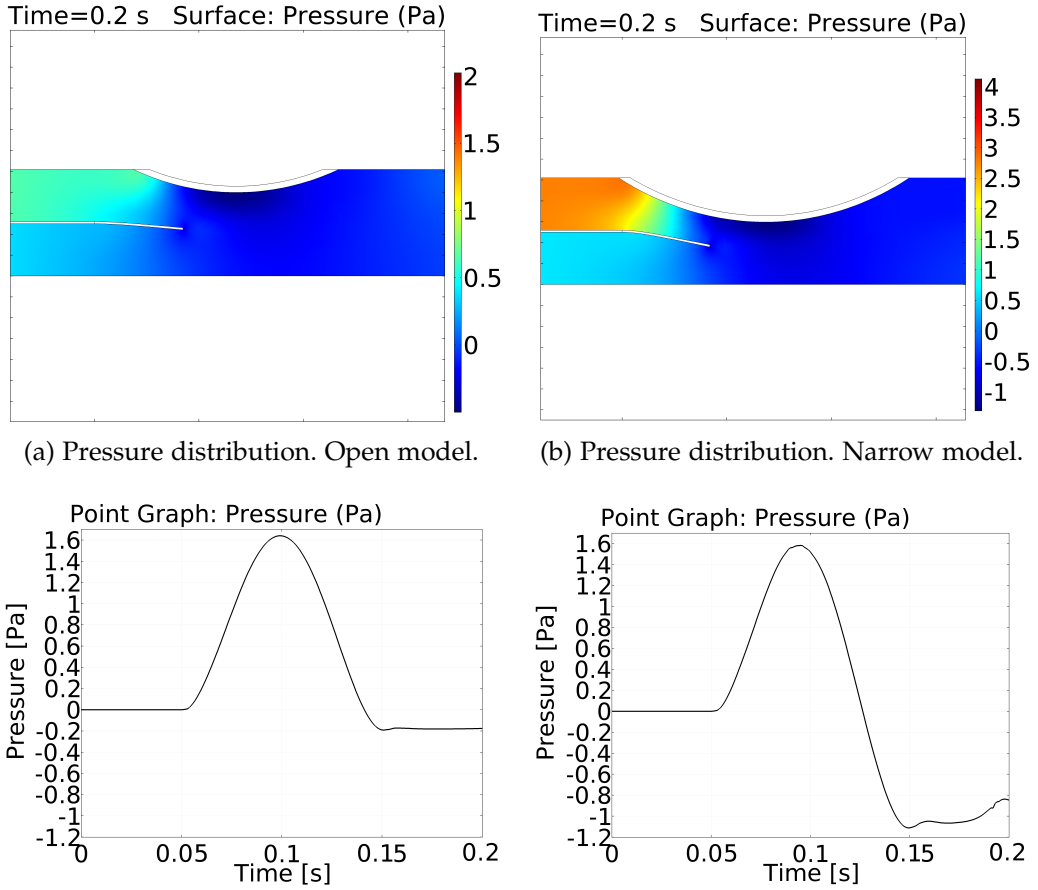

(a) Pressure distribution. Open model.

(b) Pressure distribution. Narrow model.

(c) Pressure at single point in flow. Open model

(d) Pressure at single point in flow. Narrow model.

Figure 65: 2D simulation pressure.

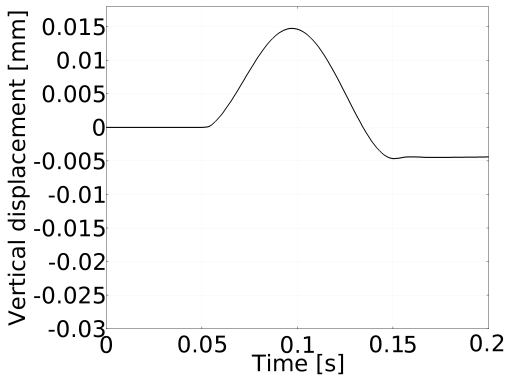

(a) Vertical displacement of obstruction midpoint. Open model.

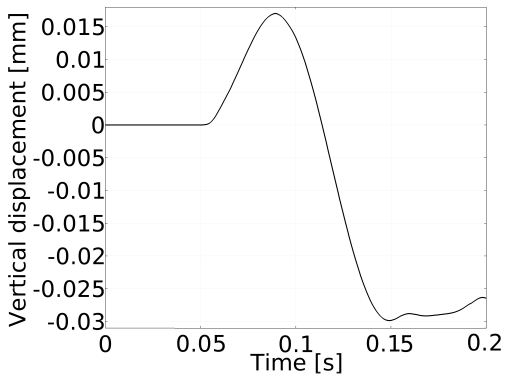

(b) Vertical displacement of obstruction midpoint. Narrow model.

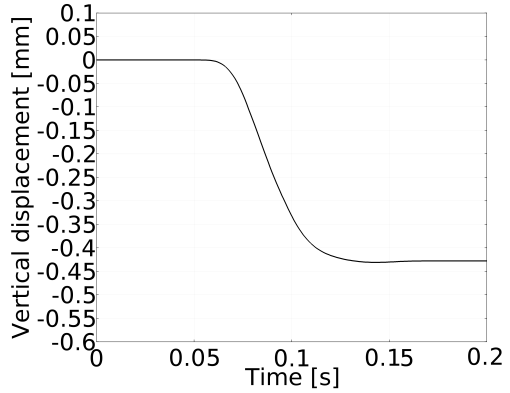

(c) Vertical displacement of flexible tip. Open model.

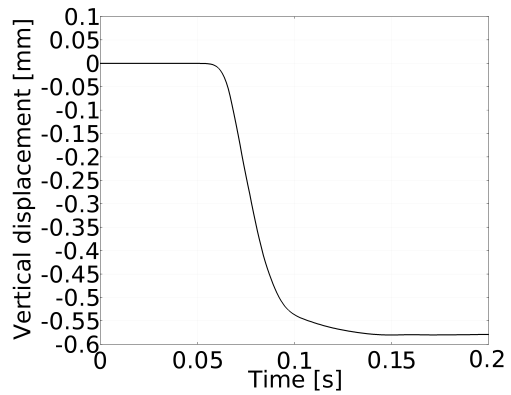

(d) Vertical displacement of flexible tip. Narrow model.

Figure 66: 2D simulation displacements.

The pressure in the channel distributes as first expected. Considering the material definitions used in the simulations the vertical displacement of the obstruction is noteworthy [Figure 66]. The low pressure is attracting downwards both the obstruction and the flexible tip in a manner of suction when air flows into the channel. Thus narrowing the channel further and hindering flow through. The partial collapse of the channel is reassembling the phenomena of flow rate limitations [25]. Hence the transmural pressure is increased.

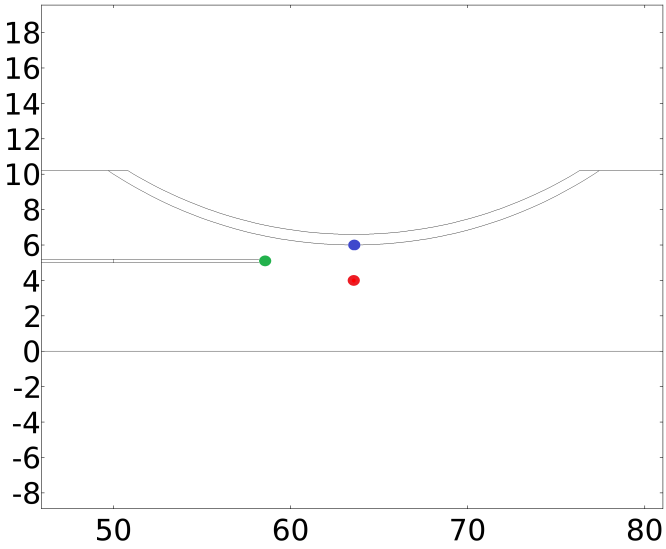

Figure 67: Selected fluid element (red), obstruction midpoint (blue) and flexible tip (green). Axes in [mm].

9.5 3D SIMULATION

After simulating the 2D case a 3D simulation was done by the embedded FSI solver in Abaqus. To further experiment with the model some of the parameters where changed. The end time for this simulation is set to 1.0 seconds.

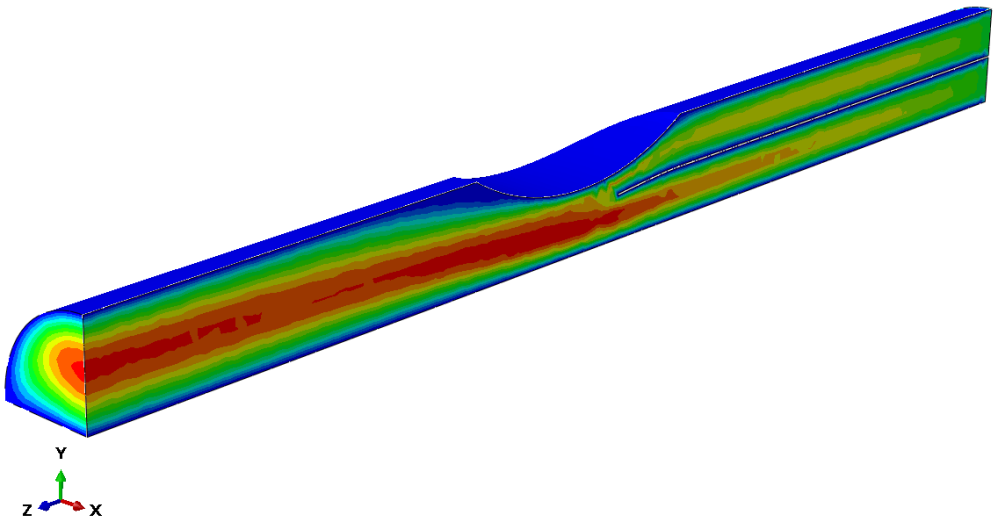

Figure 68: 3D Palate model in Abaqus. Cut view (symmetry about the z-axis).

In this case the density of the soft palate is set close to that of water [Table 5]. The 3D simulation show much of the same velocity response as the 2D simulations. In contrast to the 2D case the obstructive plate is set to rigid and is not subject to deformation. As seen in [Figure 68] the flow reaches higher velocity

closer to the center of the channel. This is due to the no-slip conditions at the interior walls and the palate.

SOLID	$\rho_s[\frac{Kg}{m^3}]$	$E[Pa]$	ν
Soft palate	1040	1.415×10^5	0.33
FLUID	$\rho_f[\frac{Kg}{m^3}]$		$\mu[Pa \cdot s]$
Air	1.185	-	1.982×10^{-5}

Table 5: Material properties in 3D palate model.

At one point the 3D simulation in Abaqus encountered a specific error in the CFD solver. Due to relative high dynamic viscosity resulting in low Reynolds numbers the solver had trouble converging the momentum equation, specified in [Section 5.4]. This particularly seems to be an issue when simulating for high flow velocities. Therefore additional iterations on the affected equilibrium equations are needed to be able to handle this issue. To avoid changing the properties and maintain material integrity the inlet flow velocity was reduced to 0.6 $[\frac{m}{s}]$.

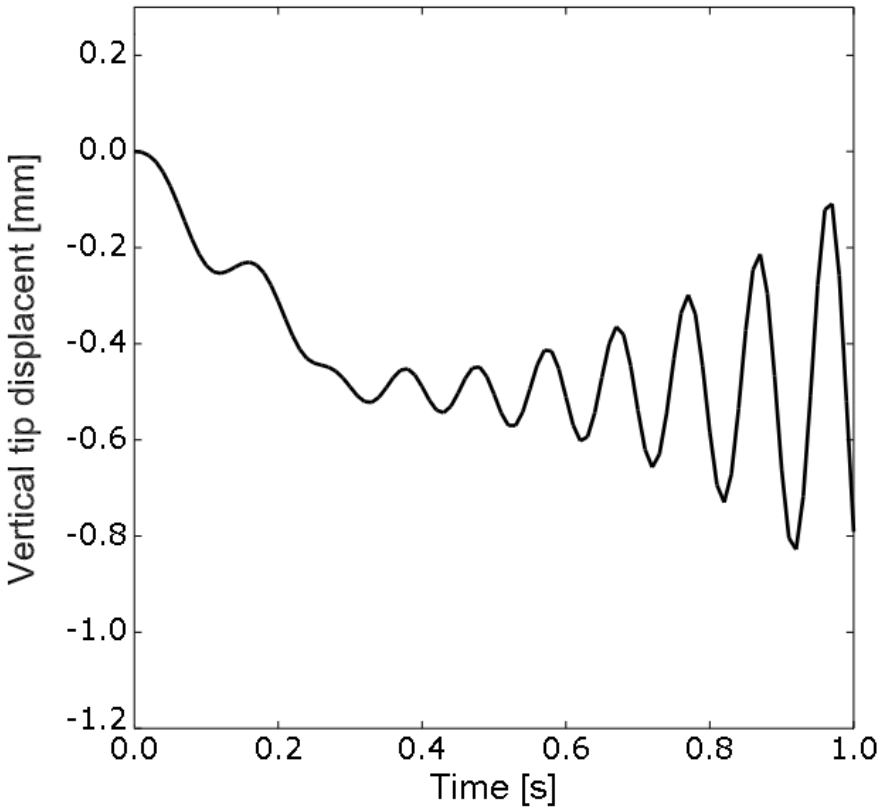

Figure 69: Vertical tip displacement. 3D Palate model in Abaqus.

Some interesting results where produced by the 3D simulation [Figure 69]. Like in the 2D case the flexible tip continues to move downward, but develops a oscillating pattern closer to 0.4 second gaining in amplitude. Further simulations and closer investigation of this was not done. However, the produced result indicates that due to the obstruction being rigid and not moving, small vortexes and local pressure changes are produced. Thus resulting in tip oscillations.

9.6 DISCUSSION

The 2D case gives a simple and coarse understanding of the phenomena of OSA. Yet it provides insight to the main issue with the disease. The low pressure created when breathing in due to the blockage causes the pharynx to collapse. Thus methods to hinder this are attractive. Some appliances has already been proposed in [Section 1.1.3]. However, finding new and better ways of dealing with this problem is of interest. Helping to find these ways describing the disease by FSI seems to be of great value.

Being the more experimental simulation, the 3D case can provide perspective and touches on the subject dealing with instability of the soft palate. To which degree this resembles reasonable behaviour is not studied further. The specific case is not the focus of this thesis. In addition comparative data is lacking for this particular setup.

Simulation by FSI has the capability to give insights and understanding of the physics defining the problem by parts and on the whole. Ultimately a more detailed description is desirable in the extent in solving close to the realistic case. To do this a model made from a CT scan of the upper airway can be analyzed by applications of FSI. This however is a whole new scenario which can prove to be a challenge. To tackle a problem description of this scale the different methods discussed in [Section 8.6] might be of helpful.

9.6.1 *Initial and boundary conditions*

The inlet and boundary conditions presumed in the simulations done in this report can be considered to provide a less descriptive solution of the problem. Thus the results has to be investigated thoroughly and made sense of in light of only reassembling the practical problem to a certain degree. By simplifying the problem description and isolating the whole into lesser problems insight to finer details can be gained. It is also often considered beneficial to go about the simulation of the problem by increasing difficulty. This enables consideration of important aspects of the problem and gives room for experimenting. Which is not easy in greater, complex and time consuming simulations.

As mentioned in [Section 1.3] defining proper initial and boundary conditions for this problem can be essential in producing reliable results. Describing

complex problems with simple models can be troublesome in the sense that imposed conditions has difficulty representing the real system. In the case of OSA a simple model like the one simulated in this report is for instance not expected to account for the behaviour of the flow prior to the oropharynx and further downstream into the laryngopharynx. Thus the more realistic flow characteristics are not likely accounted for. Therefore from a CFD point of view, the placement and specifics of considered initial and boundary conditions is of importance. Modeling a larger and more defined case accounting for longer sections of the upper airway, and setting the boundary conditions at a distance can be an option to describe better flow characteristics. For instance turbulent flow, which in addition to being important in describing airway resistance, results in more accurate description of pressure distributions and it's impact on the structural behaviour by FSI.

10

CONCLUSION AND PERSPECTIVES

10.1 INTRODUCTION

The objective of this master thesis was to compare and study the feasibility of selected solvers capable of solving FSI. This was done in light of simulating the problem of OSA, which yet proves challenging in the fields of medicine and FSI [25].

From the findings and evaluations made throughout this report some conclusions and perspectives can be stated concerning the feasibility of the different software and their applications. Primarily it is of importance that the solver is accurate, robust and can solve the problem by the material models it is assigned to an adequately degree in a limited amount of time. It is also beneficial that the solver is practical. The user interface capability and procedure of these tools vary greatly.

10.2 CONCLUSION

Computational FSI analysis proves to be a challenging branch of multiphysics. The common goal in simulating different scenarios is to get a physical meaningful and accurate solution in a a reasonable amount of time. However, the process of simulation often has drawbacks such as mesh discretization, coupling and convergence issues, in addition to trouble with the solvers. The former also seems to increase with the scale of the simulation. Hence it can be a time consuming process.

The choice of dicretization and coupling of the domains are important. The ALE method is able to produce accurate results, but the method might not be suited for problems containing large structural displacements. Using this method for larger and more complex problems are perhaps not adequate to account for the grid deformation. This is also stated by *Bavo AM et al., 2016* [5].

The ways to simulate the problem of OSA are numerous. However, for different problems descriptions there clearly are combinations of tools which are better than others. To achieve a meaningful solution the solver must be able to proper model and mesh the scenario. Reaching a solution with reasonable accuracy is preferable without a time consuming simulation. Also, it should be able to solve for nonlinear materials, transient and incompressible flow. Turbulent models may also become beneficial in describing the problem. The importance of having a adequate problem description should not be underestimated.

A simple model is a good stepping stone for simulating more challenging problems, but often produces less desirable and adequately results. However, a step-wise modeling approach in terms of difficulty may be beneficial. Starting with an easy model and evaluating the results found from parameters set. This also enables to get a better understanding of imposed boundary conditions and effects of turbulent flow. A decent knowledge of FSI and experience with the simulation tool is recommended before embarking on more complex scenarios.

Using COMSOL can results in stable and quick results for non-complex and simple simulations. It has a user-friendly interface and is fairly easy to learn. However, the solver tends to be heavy on the CPU and uses a lot of memory. This applies especially for the fully coupled approach where all equations are solved in one matrix, K. It is possible to solve for nonlinear material behaviour in COMSOL. However, it's ability to solve for nonlinear structural behaviour is not specifically tested in this project. Therefore little can be said about it's application for nonlinear materials.

By combining different models by a partitioned approach existing solvers superior in their own domains may be combined. Thus reserving software modularity and presenting flexibility to solve more advanced FSI problems. Coupling two solver which is developed by the same company may also be beneficial due to compatibility across the FSI interface and ease for the analyst. Bringing a third party coupling solver into the picture can have drawbacks to the user interface. The possible gains from coupling solver specialized in their respective fields through third party software must be weighed against its practical use.

The Abaqus CFD solver feasibility and applicability is unfortunately not tested to a satisfactory degree. Thus it may or may not be at the same level as for instance the Ansys Fluent solver, which commands great respect in the CFD community. However, the Abaqus CAE solver is considered to be in the top class at material description and behaviour. In addition to being able to solve FSI embedded by coupling Abaqus CAE and Abaqus CFD, it can also solve FSI with the coupled eulerian method (CEL) using IB. It should be noted however that the accuracy of this approach has been disputed [5]. The CEL method may prove beneficial in simulating the more detailed case of OSA. Thus when considering by both theoretical and practical sense the appliances of the commercial solver Abaqus still makes it a preferable choice.

10.3 PERSPECTIVE

The widely usage of FEM and CFD software indicates that the different solvers will develop more in the future. Although FSI has gained popularity and is used more frequently in science and engineering, the field is far from complete and is continuously under development. Though it can be cumbersome to han-

dle, the ALE method has many appliances where it produces accurate results. However, much points to development taking place around the IB method, proving capable of handling simulations with large deformations in shorter time spans. Forthcoming the solvers will hopefully be better suited to solve the problem of OSA. One thing is certain, the field of computational fluid-structure interaction has great potential, and therefore likely has a promising future.

BIBLIOGRAPHY

[1] M.D Abidin Michael. *"Hyoid Suspension to the Mandible for the Treatment of Obstructive Sleep Apnea"*. URL https://clinicaltrials.gov/ct2/show/record/NCT02738112. Feb.15.2017.

[2] J.D Anderson JR. *"Computational fluid dynamics, the basics with applications"*. McGraw-Hill Inc., Singapore, 1995.

[3] CAE Assiciates. URL https://caeai.com/blog/fluid-structure-interaction. May.20.2017.

[4] O. Axelsson. *Finite Difference Methods. Encyclopedia of Computational Mechanics.* Volume 1: Fundamentals. John Wiley & sons, 2004.

[5] AM. Bavo, G. Rocatello, F. Innaccone, J. Degroote, J. Vierendeels, and P. Segers. "Fluid-Structure Interaction Simulation of Prosthetic Aortic Valves: Comparison between Immersed Boundary and Arbitrary Lagrangian-Eulerian Techniques for the Mesh Representation." In: (2016).

[6] Yuri Bazilevs, Kenji Takizawa, and Tayfun E. Tezduyar. *Computational Fluid-Structure Interaction: Methods and Applications*. 1st. Wiley, 2013.

[7] Alexander M. Belostosky, Pavel A. Akimov, Taymuraz B. Kaytukov, Irina N. Afanasyeva, Anton R Usmanov, Sergey V. Scherbina, and Vladislav V. Vershinin. "About Finite Element Analysis of Fluid-Structure Interactiom Problems." In: *Procedia Engineering* 91 (2014), pp. 37–42.

[8] Robert D. Blevins. *Flow-Induced Vibrations*. 2nd. Krieger publishing company, 2001.

[9] M. Blumen, F. Chabolle, E. Rabischong, P. Rabischong, and B. Frachet. "Dilator muscles of the pharynx and their implication in the sleep apnea syndrome of obstructive type. Review of the literature." In: 115.2 (1998), pp. 73–84.

[10] Lexington Clinic. URL https://www.lexingtonclinic.com/osasurgery/hyoid.html. Jan.11.2017.

[11] Ryan M. Clodagh and Bradley T. Douglas. "Pathogenesis of obstructive sleep apnea." In: *Applied Physiology* 99.6 (2005), 2440–2450.

[12] OpenStax College. *Anatomy and Physiology*. URL http://cnx.org/contents/14fb4ad7-39a1-4eee-ab6e-3ef2482e3e22@8.26. June.06.2017.

[13] Jerome A. Depssey, Sigrid C. Veasey, Barbara J. Morgan, and Christopher P. O'Donnel. "Pathophysiology of Sleep Apnea." In: *Physiological Reviews* 90.1 (2010), pp. 47–112.

[14] Bradley Froehle and Per-Olof. Persson. "A High-Order Discontinuous Galerkin Method for Fluid-Structure Interaction With Efficient Implicit-Explicit Time Stepping." In: *Journal of Computational physics* (2015).

[15] C Förster, W.A Wall, and E. Ramm. "Artificial added mass instabilities in sequential staggered coupling of nonlinear structures and incompressible viscous flows." In: *Computer Methods in Applied Mechanics and Engineering*, Volume 196.7 (2007), pp. 1278–1293.

[16] C. W. Hirt and B.D. Nichols. "Volume of Fluid (VOF) Method for the Dynamics of Free Boundaries." In: *Journal of Computational Physics* Volume 39 (1981).

[17] Gene Hou, Jin Wang, and Anita Layton. "Numerical Methods for Fluid-Structure Interaction — A Review." In: *Communications in Computational Physics* 12.2 (2012), pp. 337–377.

[18] Health Hype. URL http://www.healthhype.com/. Jan.02.2017.

[19] University of Illinois. *Computational Fluid Dynamics*. URL https://uiuc-cse.github.io/me498cm-fa15/lessons/fluent/fvm.html. May.25.2017.

[20] University of Illinois. URL http://verl.npre.illinois.edu/NumericalMethodsandC html. May.28.2017.

[21] ANSYS Inc. URL http://www.ansys.com/. Feb.01.2017.

[22] Adina R&D Inc. URL http://www.adina.com/fluid-structure-interaction.shtml. June.02.2017.

[23] COMSOL Inc. URL https://www.comsol.com/blogs/fem-vs-fvm/. March.13.2017.

[24] Dear Doctor Inc. URL http://www.deardoctor.com/articles/sleep-apnea-faqs/. Jan.08.2017.

[25] Tu Jiyuan, Kiao Inthavong, and Goodarz Ahmadi. *Computational Fluid and Particle Dynamics in the Human Respiratory System*. 1st. Springer Netherlands, 2013.

[26] R. van Loon, P.D Anderson, and F.N van de Vosse. "A fluid–structure interaction method with solid-rigid contact for heart valve dynamics." In: *Journal of Computational Physics* 217 (2006), pp. 806–823.

[27] R. van Loon, P.D Anderson, F.N van de Vosse, and S.J. Sherwin. "Comparison of various fluid–structure interaction methods for deformable bodies." In: *Computers and Structures* 85 (2007), 833–843.

[28] OpenCFD Ltd. URL http://www.openfoam.com/. June.03.2017.

[29] WEb MD. URL http://www.webmd.com/sleep-disorders/sleep-apnea/continuous-positive-airway-pressure-cpap-for-sleep-apnea. Jan.16.2017.

[30] G. C. Mbata and J. C. Chuckwuka. "Obstructive sleep apnea hypopnea syndrome." In: *Ann Med Health Sci Res* 2.1 (2012), pp. 74–77.

[31] Mayo Foundation for Medical Education and Research. URL http://www.mayoclinic.org/. Feb.01.2017.

[32] C. Michler, E.H van Brummelen, R. de Borst, and S.J. Hulshoff. "A, monolithic approach to fluid structure interaction." In: *Computers & Fluids* 33.Issue 5-6 (2004), 839–848.

[33] F. Moukalled, L. Mangani, and M. Darwish. *The Finite Volume Method in Computational Fluid Dynamics*. 1st. Volume 113. Springer International Publishing, 2015.

[34] Madara M. Ogut and Kremer Gul. *"Engineering Design: A, the Practical Guide"*. Trafford, 2004.

[35] M. R. Rasani, K. Inthavong, and J.Y. Tu. "Simulation of pharyngeal airway interaction with airflow using low-Re turbulence model." In: *Modeling and Simulation in Engineering* (2011).

[36] The Visual Room. URL http://thevisualroom.com/finite_volume_method_4.html. Feb.03.2017.

[37] Fraunhofer SCAI. *MpCCI 4.4.2-1 Documentation*. URL http://www.mpcci.de/content/dam/scai/mpcci/documents/MpCCIdoc.pdf. March 20, 2017.

[38] Fraunhofer SCAI. *MpCCI – The Independent Code Coupling Interface*. URL http://www.probabilistik.de/vortrag/v2011_brodbeck.pdf. March 22, 2017.

[39] U. Saravanan. *"Advanced Solid Mechanics"*. McGraw-Hill Inc., Indian Institute of Technology Madras, 2013.

[40] Sciphile.org. URL http://sciphile.org/lessons/bernoullis-principle-and-venturi-tube. March.03.2017.

[41] Sharcnet. URL https://www.sharcnet.ca/Software/Ansys/17.0/en-us/help/exd_ag/exp_dyn_theory_ref_frame.html. March.20.2017.

[42] Jörg Shröder and Peter Wriggers. *Advanced Finite Element Technologies*. 1st. Volume 566. Springer International Publishing, 2016.

[43] Adriaan Sillem. *"Feasibility study of a tire hydroplaning simulation in a infnite element code using a coupled Eulerian-Lagrangian method"*. Delft university of technology, October 2008.

[44] Bjorn Sjodin. *"What's The Difference Between FEM, FDM, and FVM?"* URL http://machinedesign.com/fea-and-simulation/what-s-difference-between-fem-fdm-and-fvm. April.19.2017.

[45] Dassault Systèmes. URL http://www.3ds.com/products-services/simulia/products/abaqus/. Jan.19.2017.

[46] Sander Vaher. *"A Weakly Coupled Strategy for Computational Fluid-Structure Interaction: Theory, Implementation and Application"*. Swansea University, June 2013.

[47] C.H.K. Williamson and R. Godvardhan. "Vortex-induced vibrations." In: *Fluid Mechanics,* Volume 36 (2004), pp. 413–455.

[48] O.C. Zienkiewicz, R.L Taylor, and J.Z Zhu. *The finite element method - its basis fundamentals*. 7th. Elsevier, 2013.